Department of Radio Science and Engineering

Studies on microelectro-mechanically tuneable high-impedance surface for millimetre wave beam steering

---

Dmitri Chicherin

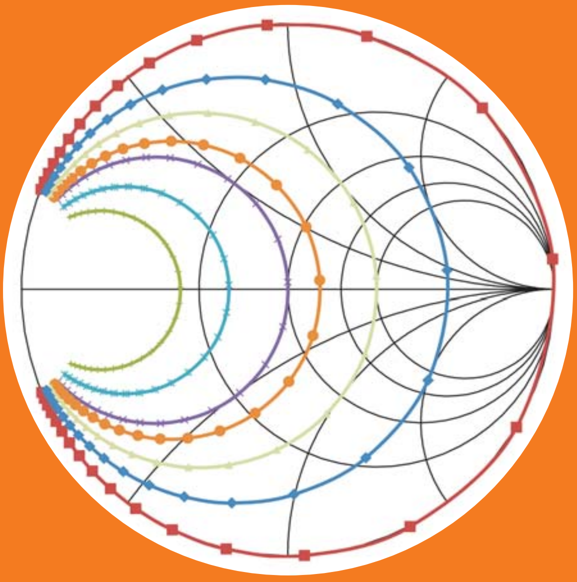

DOCTORAL DISSERTATIONS

Aalto University publication series
DOCTORAL DISSERTATIONS 127/2011

Studies on microelectromechanically tuneable high-impedance surface for millimetre wave beam steering

Dmitri Chicherin

Doctoral dissertation for the degree of Doctor of Science in Technology to be presented with due permission of the School of Electrical Engineering for public examination and debate in Auditorium S1 at the Aalto University School of Electrical Engineering (Espoo, Finland) on the 2nd of December 2011 at 12 o'clock noon.

Aalto University
School of Electrical Engineering
Department of Radio Science and Engineering

Supervisor
Professor Antti V. Räisänen

Instructor
Professor Antti V. Räisänen

Preliminary examiners
Professor Wolfgang Menzel, University of Ulm, Germany
Dr. Tauno Vähä-Heikkilä, VTT Technical Research Centre of Finland

Opponent
Professor Didier Lippens, Université des Sciences et Technologie de Lille, France

Aalto University publication series
DOCTORAL DISSERTATIONS 127/2011

ISBN 978-952-60-4389-0 (printed)
ISBN 978-952-60-4390-6 (pdf)
ISSN-L 1799-4934
ISSN 1799-4934 (printed)
ISSN 1799-4942 (pdf)

Unigrafia Oy
Helsinki 2011

Finland

The dissertation can be read at http://lib.tkk.fi/Diss/

NORDIC ECOLABEL
441 697
Printed matter

Aalto University

Aalto University, P.O. Box 11000, FI-00076 Aalto www.aalto.fi

Abstract

Author
Dmitri Chicherin

Name of the doctoral dissertation
Studies on microelectromechanically tuneable high-impedance surface for millimetre wave beam steering

Publisher School of Electrical Engineering

Unit Department of Radio Science and Engineering

Series Aalto University publication series DOCTORAL DISSERTATIONS 127/2011

Field of research Radio Engineering

Manuscript submitted 10 June 2011 **Manuscript revised** 6 November 2011

Date of the defence 2 December 2011 **Language** English

☐ **Monograph** ☒ **Article dissertation (summary + original articles)**

Abstract

This thesis focuses on the development of novel microelectromechanically tuneable high-impedance surfaces (HIS) for millimetre wave beam steering applications. Microelectromechanical systems (MEMS) provide good functional parameters, e.g., low loss even at millimetre wave frequencies and excellent reliability, and can effectively compete with conventional technologies, e.g., ferroelectrics and ferrites. At the same time MEMS enable tuneability of the HIS, which can be used for developing reconfigurable devices with decreased system complexity, high level of integration and even as a system-on-a-chip, which dramatically reduces cost of the high frequency devices.

The proposed MEMS tuneable HIS consists of a two-dimensional periodical arrangement of MEMS varactors, with a period much smaller than the wavelength of the interacting electromagnetic field, placed on an electrically thin grounded dielectric substrate. Being embedded in a waveguide, the structure can be used as an analogue type phase shifting element controlled by a bias voltage connected to the MEMS varactors. Alternatively, the MEMS tuneable HIS can be used as a smart electronic beam steering reflective surface, if a reconfigurable gradient of the effective surface impedance is induced throughout the structure by applying different programmed bias voltages to the different rows of the MEMS varactors.

The methodology used in this study is a combination of analytical analysis, numerical simulations and electromagnetic measurements. A precise analytical model of the MEMS tuneable HIS is derived and used for designing of the structures operating in the W-band. Numerical simulations of different types of HIS and phase shifters based on the tuneable impedance surface embedded in rectangular metal waveguides and dielectric rod waveguides are carried out. Results of the numerical simulations correspond very well with the analytical calculations. Several prototypes of the multi-layered and MEMS-based HIS are fabricated and characterised. Measurements of the reflection coefficient show clear resonant high-impedance behaviour in the designed frequency range with reflection phase changing from almost 180° at lower frequencies to 0° at the resonance and to almost 180° at higher frequencies. The measured phase shifter based on a MEMS tuneable HIS placed adjacent to a dielectric rod waveguide exhibits an analogue type phase shift of up to 70° when the bias voltage is applied to the MEMS varactors.

Keywords High-impedance surface, artificial electromagnetic materials, microelectromechanical systems, MEMS, beam steering, phase shifters, millimetre wave

ISBN (printed) 978-952-60-4389-0 **ISBN (pdf)** 978-952-60-4390-6

ISSN-L 1799-4934 **ISSN (printed)** 1799-4934 **ISSN (pdf)** 1799-4942

Location of publisher Espoo **Location of printing** Helsinki **Year** 2011

Pages 164 **The dissertation can be read at** http://lib.tkk.fi/Diss/

Preface

This dissertation is a summary of the research work performed at the Department of Radio Science and Engineering of Aalto University (formerly Radio Laboratory of TKK Helsinki University of Technology). I am most grateful to Professor Antti Räisänen for the opportunity to carry out research in the Radio Laboratory on the very exciting subject, for supervising this work, supporting and guiding me in radio engineering. I also thank Professor Antti Räisänen for entrusting me – a PhD student – to prepare a European FP7 project proposal TUMESA back in 2007, and to function as a project manager of TUMESA, which gave me an invaluable professional and personal experience.

It is my pleasure to thank Professor Sergei Tretyakov for sharing his experience and introducing me at the earlier stage of this work to the concept of artificial electromagnetic materials, which was crucial for my research. I greatly appreciate joint work with Dr. Dmitri Lioubtchenko and Dr. Sergey Dudorov and fruitful discussions with Prof. Constantin Simovski.

I express my sincere gratitude to Dr. Victor Ovchinnikov for microfabrication of the very first prototypes described in this work. Other devices were fabricated at KTH – Royal Institute of Technology by Mr. Mikael Sterner under supervision of Associate Professor Joachim Oberhammer, leader of RF MEMS group of KTH Microsystem Technology Lab. They both deserve my special thanks for fabricating the devices that I have been designing, and for our long term, fluent and productive collaboration. It was also a great pleasure to collaborate with other TUMESA partners: Mr. Jan Åberg, the Vice President of MicroComp Nordic, Professor Ronan Sauleau, Dr. Erwan Fourn and Dr. Alexander Vorobyov of Université de Rennes 1, and Dr. Frantz Bodereau of Autocruise S.A.

I am very grateful to all the personnel of the Department of Radio Science and Engineering for their help and for keeping up the good atmosphere. Especially I would like to mention Professor Igor Nefedov and Dr. Sylvain Ranvier, who were my roommates, Dr. Clemens Icheln, Dr. Juha Mallat, Dr. Juha Ala-Laurinaho, Dr. Vladimir Podlozny, Dr. Timo Veijola, Mr. Tomás Zvolenský, Mr. Zhou Du, Mr. Lorenz Schmuckli, Mrs. Stina Lindberg and Mrs. Tuula Mylläri.

I am thankful to the pre-examiners of this dissertation Professor Wolfgang Menzel and Dr. Tauno Vähä-Heikkilä for their observations and Professor Didier Lippens for accepting to be the opponent.

Academy of Finland, Tekes and the European Commission is acknowledged for financial support of my research work.

Professor Igor Mashek, the supervisor of my Master degree, Professor Sergey Manida, the then Dean of the Physics Faculty of the St. Petersburg

State University, and Professor Marc Chenevier of Université Joseph Fourier, Grenoble, are greatly appreciated for their support of my international research carrier, which started in 1997.

Finally, I wish to thank my great family: Lilia, Maria, Sergey, Grigory, Sari and late Lyudmila for their care and encouragements throughout my studies and research. I send my warmest thanks to my dear wife Maria for her love and support, and to our wonderful daughters Tatiana and Katarina for bringing joy in our lives.

November 5th, 2011

Дмитрий Чичерин

Dmitri Chicherin

Contents

List of publications

The thesis is based on the work presented in the following papers:

[P1] D. Chicherin, S. Dudorov, D. Lioubtchenko, V. Ovchinnikov, S. Tretyakov, and A.V. Räisänen, "MEMS-based high-impedance surfaces for millimetre and submillimetre wave applications," *Microwave and Optical Technology Letters*, vol. 48, no. 12, pp. 2570-2573, 2006.

[P2] D. Chicherin, S. Dudorov, D. Lioubtchenko, V. Ovchinnikov, and A.V. Räisänen, "Millimetre wave phase shifters based on a metal waveguide with a MEMS-based high-impedance surface," *Proc. of the 36th European Microwave Conf.*, Manchester, UK, September 10-15, 2006, pp. 372-375.

[P3] D. Chicherin, S. Dudorov, D. Lioubtchenko, V. Ovchinnikov, and A.V. Räisänen, "Characterisation and measurements of a multilayer high-impedance surface at W-band," *Proc. of the 1st International Congress on Advanced Electromagnetic Materials in Microwave and Optics*, Rome, Italy, October 22-26, 2007, pp. 891-894.

[P4] D. Chicherin, S. Dudorov, M. Sterner, J. Oberhammer, and A.V. Räisänen, "Micro-fabricated high-impedance surface for millimeter wave beam steering applications," *Proc. of the 33rd International Conf. on Infrared, Millimeter, and Terahertz Waves*, Pasadena, California, USA, September 15-19, 2008, PID659522.pdf, Keynote presentation.

[P5] M. Sterner, D. Chicherin, A.V. Räisänen, G. Stemme, and J. Oberhammer, "RF MEMS high-impedance tuneable metamaterials for millimeter-wave beam steering," *Proc. of the IEEE MEMS Conf.*, Sorrento, Italy, January 25-29, 2009, pp. 896-899.

[P6] D. Chicherin, M. Sterner, J. Oberhammer, S. Dudorov, J. Åberg, and A.V. Räisänen, "Analog type millimeter wave phase shifters based on MEMS tunable high-impedance surface in rectangular metal waveguide," *IEEE International Microwave Symp. Digest*, Anaheim, CA, USA, May 25-28, 2010, pp. 61-64.

[P7] M. Sterner, D. Chicherin, J. Åberg, R. Sauleau, A.V. Räisänen, G. Stemme, and J. Oberhammer, "Integration of MEMS reconfigurable reflective surfaces in rectangular waveguide stubs for W-band phase-shifters," *Proc. of Asia Pacific Microwave Conf.*, Yokohama, Japan, December 7-10, 2010, pp. 1825-1828.

[P8] D. Chicherin, M. Sterner, J. Oberhammer, S. Dudorov, D. Lioubtchenko, A.J. Niskanen, V. Ovchinnikov, and A.V. Räisänen, "MEMS based high-impedance surface for millimetre wave dielectric rod waveguide phase shifter," *Proc. of the 40th European Microwave Conf.*, Paris, France, September 28-30, 2010, pp. 950-953.

[P9] D. Chicherin, M. Sterner, D. Lioubtchenko, J. Oberhammer, A.V. Räisänen, "Analog-type millimetre wave phase shifters based on MEMS tunable high-impedance surface and dielectric rod waveguide," *International Journal of Microwave and Wireless Technologies,* vol. 3, no. 5, pp. 533-538, 2011.

[P10] Z. Du, D. Chicherin, and A.V. Räisänen, "Millimeter wave beam steering with a MEMS-based high impedance surface," *Proc. of European Microwave Conf.*, Manchester, UK, October 9-14, 2011, pp. 1043-1046.

In addition to the publications listed above, the author of this thesis has contributed to other journal, conference and workshop publications related to the field of the research [1]-[20].

Contribution of the author

In paper [P1] the author proposed the layout of MEMS varactors to be used in HIS, designed the multilayer HIS, drew masks for microfabrication, carried out measurement campaign and analysed the results. The author prepared the manuscript.

In paper [P2] the author performed numerical analysis of the multilayer HIS, designed the MEMS-based HIS, drew masks for microfabrication, carried out measurement campaign and analysed the results. The author prepared the manuscript.

In paper [P3] the author proposed the equivalent circuit model and derived equations for the effective surface impedance and effective resonant circuit parameters of the multilayer HIS, performed numerical simulations and analysed the results. The author prepared the manuscript.

In paper [P4] the author performed numerical analysis of the improved HIS, designed it, carried out measurement campaign and analysed the results. The author prepared the whole manuscript except Section “Fabrication”.

In paper [P5] the author performed numerical analysis of the MEMS-based HIS, designed the MEMS-based HIS, and carried out S11-parameter measurements. The author participated in the manuscript preparation.

In paper [P6] the author performed analytical and numerical analysis of the MEMS-based HIS, designed the MEMS-based HIS, and carried out S11-parameter measurements. The author prepared a major part of the manuscript.

In paper [P7] the author carried out S11-parameter measurements of the different interfaces. The author participated in the manuscript preparation.

In paper [P8] the author performed analytical and numerical analysis of the MEMS-based HIS and the phase shifter, designed a large MEMS-based HIS, and carried out S-parameters measurements. The author prepared the manuscript.

In paper [P9] the author performed analytical and numerical analysis of the MEMS-based HIS and the phase shifter, designed the large MEMS-based HIS, and carried out S-parameters measurements. The author prepared the manuscript.

In paper [P10] the author formulated the research question, proposed the simplified model, discussed the numerical results and carried out S-parameter measurements. The author prepared a large part of the manuscript.

Abbreviations

DRW	Dielectric rod waveguide
HIS	High-impedance surface
ICT	Information and communication technologies
lhs	Left-hand side (of a figure)
MEMS	Microelectromechanical systems
PEC	Perfect electric conductor
PMC	Perfect magnetic conductor
rhs	Right-hand side (of a figure)
SEM	Scanning electron microscopy
S-parameter	Scattering parameter
SRR	Short range radar
TE	Transverse electric
TM	Transverse magnetic
VCO	Voltage-controlled oscillator

Symbols

a	Width of the waveguide cross-section (perpendicular to the E-field)
A_{holes}	Total area of all etching holes
A_{MEMS}	Area of the MEMS varactors
A_{solid}	Area of the solid metal parallel plate capacitance
c	Speed of light
C_{eff}	Effective capacitance of the square mesh
d	Overlapping between the parallel plates
$d_{\mathrm{DRW\text{-}HIS}}$	Distance between the DRW and HIS
D	Period of the mesh of patches or of a HIS
f	Frequency of the wave
g	Gap of the parallel plate (MEMS) capacitor
g_0	Initial gap between the actuation electrode and the MEMS membrane
h	Thickness of the dielectric substrate
k_0	Free space wave impedance
k_{eff}	Effective wave number
$\vec{k}_{HIS}$	Wave vector in the HIS section of the waveguide
$\vec{k}_{wg}$	Wave vector in the metal waveguide
l	Length of the corrugation stub
l_{spr}	Length of the spring
L_{eff}	Effective inductance of the HIS
L_{x}	Patch length
O	Big-O notation
R	Reflection coefficient for a normally incident field
R_{d}	Effective series resistance of the dielectric substrate
R_{pp}	Resistance of the parallel plate capacitor
s, s_1, s_2	Separation between the patches
s_{spr}	Spacing between the turns of the spring
t_{e}	Thin actuation electrode thickness
t_{p}	Lower patches thickness
V	Bias voltage applied to the MEMS varactors
w	Width of the metal plates and membranes
$w_{\mathrm{DRW\text{-}HIS}}$	Width of the HIS adjacent to the DRW
w_{spr}	Width of the spring
W	Width of the actuation electrode
Z	Impedance of the corrugated surface
Z_0	Characteristic impedance
Z_{d}	Input impedance of the grounded dielectric
Z_{eff}	Effective impedance of a structure
Z_{mesh}	Effective surface impedance of the square patches mesh for normal incidence
Z_{pp}	Impedance of the parallel plate capacitor

Z^{TE}_{mesh}	Effective surface impedance of the square patches mesh for TE-polarisation
Z^{TM}_{mesh}	Effective surface impedance of the square patches mesh for TM-polarisation
Z_{tot}	Total effective input impedance of the multilayer HIS
α	Mesh parameter of square metal patches' mesh
Δk_z	Wave number difference
$\Delta\varphi$	Phase difference of the waves exiting the waveguide
ε'	Real part of the permittivity
ε''	Imaginary part of the permittivity
ε_0	Permittivity of the free space
ε_1	Relative permittivity of the media above the structure
ε_2	Relative permittivity of the media below the structure
ε_{eff}	Effective relative permittivity
η_{eff}	Effective wave impedance
Θ	Angle of incidence to a surface
λ	Wavelength of the electromagnetic field
μ_0	Permeability of the free space
ω	Electromagnetic wave angular frequency
ω_0	Resonance angular frequency

1. Introduction

1.1. Background and motivation

The millimetre and submillimetre wavelength region is of increasing interest for many applications, namely, secure high-capacity communication systems, automotive and industrial radar, spectroscopy, medical diagnostics, radio astronomy, atmospheric remote sensing, etc. Despite a higher price of the basic components, e.g., phase shifters, in comparison with those at microwaves, millimetre wave systems meet expanding interests and demand of customers.

Traffic safety is one of the major concerns of the present society. The European Commission has taken numerous actions to increase traffic safety, such as: “European transport policy for 2010: time to decide”, eSafety, “Intelligent Car initiative” (which includes safety issues), and has regularly addressed this issue in research and development work programmes. The European Commission announced its intention to improve road safety in Europe by using new ICT systems, such as automotive radar equipment. By the European Commission mandate [21], the European Conf. of Postal and Telecommunications Administrations (CEPT) identified that the 79 GHz band is the most suitable band for the long term development and deployment of automotive short-range radar (SRR). Consequently, EC decided in 2004 to ultimately utilise the 79 GHz band for SRR [22], but authorised employment of SRR at 24 GHz on a temporal basis till July 1st 2013, in order to ensure commercial cost-effective readiness of 79 GHz technology before that time [23]. However, in December 2010 EC issued a call to stakeholders for their views on the proposed amendment to this Commission decision, emphasising that SRR technology at 79 GHz is not progressing in such a way as to guarantee availability even by July 2013 [24].

Regarding the operation frequency of the automotive radars, the 77-81 GHz frequency range (otherwise called the 79 GHz band) is now the targeted range due to the following reasons:

- it will be dedicated to the automotive applications,
- it offers decreased size and weight compared to the 24 GHz band,
- it ensures better angular resolution with moderate antenna size,
- the necessary 4 GHz frequency bandwidth is reachable for the needed high frequency components.

The main current challenges for developing systems for wireless application at millimetre wave frequencies are fabrication complexity, cost, and high level of losses of electronic components conventionally based, e.g., on semiconductor or ferroelectric technologies. As a result, the European Commission suggests an extension of the use of the 24 GHz band for SRR applications until January 1st, 2022, which means that novel disruptive and smart solutions are needed to develop high-performance and cost-efficient automotive radar in the near future. This work shows possible directions of elaborating such solutions, which can also be used for other applications, such as indoor communication systems and Internet-of-Things.

Many car manufacturers have already introduced single beam automotive radar into their expensive models. These radars usually include such features as adaptive cruise control (i.e. maintaining constant speed but not larger than the speed of a preceding vehicle), lane change assist, assisted stop-and-go and so on. For example, TRW Automotive / Autocruise S.A. has developed an automotive radar AC-20 at 76-77 GHz, with the range 1-200 m, field of view 11°, speed resolution 0.09 kilometre per hours, size $98 \times 98 \times 63\ \mathrm{mm}^3$ and weight 0.55 kg [25]. A traffic safety system with adaptive cruise control and side lane change assist valued ca. 2500 € can be purchased, e.g., as an option of Volkswagen Phaeton [26], which is an expensive vehicle itself. Therefore, the current price of the automotive radar prohibits penetration of this crucial active safety technology to the middle car segment, which is indispensable for significant improvement of the overall road safety.

From performance point of view, presently there is a lack of a 79 GHz scanning beam radar, which should have a field of view up to ±60° because the main feature of the future automotive radar is ability to scan the environments in order to determine possible obstacles and avoid dangerous traffic situations, which is not possible with a single beam radar. Consequently, a high performance beam steering antenna is needed. Mechanical beam steering realised by, e.g., phased array antennas with mechanical rotating phase shifters [27], or dielectric waveguide adjacent to a constantly rotating drum with a special grating structure [28], is rather complex and expensive, especially at millimetre wave frequencies, hence an electronic beam steering is required. Another solution, popular for a wide scope of applications, is beam switching utilising different types of beamforming techniques [29] to produce tilted beams by off-focus feeds. Several types of beamformers have been realised at millimetre wavelengths, e.g., standard power division using Butler matrices [30], quasi-optical beamformers based on Rotman lens [31], and substrate integrated reflectors [32],[33]. A typical drawback of these solutions is large insertion loss due to the complexity of the structure, low efficiency and poor radiation performance for large beam deviations. In addition, radar with beam switching, in contrast to beam steering, cannot provide required information in a sophisticated and rapidly changing traffic environment. This can be overcome by developing a high-performance millimetre wave phased array antenna [34] equipped with phase shifters, or by offering a novel beam steering solution.

Existing millimetre wave phase shifters change the phase by adjusting either the geometrical parameters of the device, e.g., changing the electrical length of a transmission line using semiconductor switches [35], [36], or material properties of its components, e.g., by applying magnetic or electric field [37]. Transmission line based phase shifters are not convenient, e.g., in phased arrays, due to the size and integration issues. Existing materials with controllable parameters usually are very lossy at the millimetre wavelengths. Therefore, artificial electromagnetic materials, also called metamaterials [38]-[40], combined with MEMS (microelectromechanical systems) fabrication technology [41], [42] can provide a prospective solution.

Artificial electromagnetic materials are periodic or non-periodic arrangements of structural elements, which exhibit unusual and advantageous electromagnetic properties engineered beforehand by utilising effective medium analytical models. The models are applicable thanks to the size of the structural element, which is much smaller than the wavelength of the electromagnetic field the artificial electromagnetic material interacts with. MEMS offer many advantages in manufacturing of artificial electromagnetic materials. MEMS are electrically controllable structures utilizing both electrical and mechanical properties. MEMS-based devices provide good functional parameters, such as low loss even at millimetre wave frequencies and excellent reliability, e.g., MEMS switches with 0.1 dB of insertion loss [43] and 1.5 trillion life cycles [44]. MEMS provide a good opportunity at millimetre and submillimetre wavelengths, where ferrites and ferroelectrics are not applicable due to higher insertion loss [45]-[47]. On the other hand, MEMS-based phase shifters in microstrip and coplanar waveguides usually suffer from high transmission line losses [48] and are not volume-efficient; that is why novel approaches of utilisation of MEMS are needed.

1.2. Scope and contents of the thesis

The objective of the work is to study novel MEMS tuneable HIS and to design analogue type phase shifters based on this surface operating at a frequency near 79 GHz, which is a standard frequency of anti-collision automotive radars. We use MEMS tuneable capacitors incorporated into a HIS, which can be used either for introducing a phase shift into the incident field in a rectangular metal waveguide, or for changing the propagation constant of a dielectric rod waveguide. We also study the feasibility of a smart reconfigurable HIS for a single chip electronic beam steering.

We propose [P1] to use MEMS in order to produce novel phase shifters based on an electronically reconfigurable high-impedance surface (HIS), which is a particular type of artificial electromagnetic materials. Typically, the HIS is a textured metal surface with impedance varying from some initial value to a very high value depending on the frequency of the incident electromagnetic field [49]. The MEMS tuneable HIS consists of a periodic two-dimensional arrangement of MEMS varactors placed on an electrically thin dielectric substrate with a ground plane [P1]-[P5].

The phase shifters can be developed by introducing the MEMS tuneable HIS in a rectangular metal waveguide [P6]-[P7] or dielectric rod waveguide [P8]-[P9], which affects the phase factor of the reflection coefficient of the incident wave, or the phase factor of the effective propagation constant of the waveguiding medium. Since the effective surface impedance is controlled with a bias voltage, the phase shifting effect is purely of an analogue type.

Electronic beam steering can be also achieved by inducing a gradient of the surface impedance throughout a larger MEMS tuneable HIS, which, in turn, creates a gradient of the phase of the reflection coefficient [P10]. Being controlled by a bias voltage applied to the individual rows of electrically small MEMS elements, the surface can reflect the incident beam in a programmed direction. Since the whole structure can be fabricated as a system-on-a-chip, implementation of this solution for automotive radar application can lead to a dramatic cost decrease due to the reduction of the antenna system complexity.

The design work, analytical and numerical analysis and millimetre wave measurements were carried out at the Aalto University School of Electrical Engineering, Department of Radio Science and Engineering (formerly, Helsinki University of Technology, Radio Laboratory), within SMARAD Centre of Excellence. The fabrication of the HIS prototypes described in [P1]-[P3] was performed at the Microfabrication Centre of the Helsinki University of Technology, and the fabrication of the prototypes described in [P4]-[P9] was performed at the Microsystem Technology Lab, KTH – Royal Institute of Technology (Stockholm, Sweden).

The research work described in this thesis has received funding from:

- the Academy of Finland through the TULE Research Programme in the frame of the MIRA project (novel electroacoustic solutions for micromechanical radios, 2003-2006);

– the Finnish Funding Agency for Technology and Innovation (TEKES) and the Swedish Governmental Agency for Innovation Systems (VINNOVA) through the NORDITE Scandinavian ICT Programme in the frame of the SARFA I and SARFA II project (RF MEMS Steerable Antennas for Automotive Radar and Future Wireless Applications, 2006-2010);
– the European Community's Seventh Framework Programme (FP7/2007-2013) under grant agreement n° 224197 in the frame of the FP7 project TUMESA (MEMS Tuneable Metamaterials for Smart Wireless Applications, 2008-2011);
– the Academy of Finland under the Centre of Excellence in Research Programme.

The remaining of the thesis is organised in the following manner:

Chapter 2 is devoted to the novel MEMS tuneable HIS. The chapter describes conventional HIS and its applications, analytical model of a multilayer HIS and shows results of numerical simulations of both multilayer and MEMS tuneable HIS. Design and actuation voltage of the MEMS varactors are analysed as well. Measurement results of the multilayer HIS are presented and show correspondence to the analytical model.

Chapter 3 is focused on the analogue type phase shifter based on the MEMS tuneable HIS integrated in a rectangular metal waveguide. The chapter describes analytical and numerical analysis of the phase shifter, fabrication of the MEMS-based HIS and presents measurements results.

Chapter 4 is focused on the analogue type phase shifter based on the MEMS tuneable HIS adjacent to a dielectric rod waveguide. The chapter describes analytical and numerical analysis of the phase shifter, fabrication of the MEMS tuneable HIS and shows measurements results of the analogue type phase shifter.

Chapter 5 is devoted to the feasibility study of the beam steering reflective MEMS tuneable HIS and includes analytical and numerical analysis of the large tuneable impedance surface performance for changing the direction of the reflected wave.

Chapter 6 gives summaries of the publications, and Chapter 7 draws conclusions and describes future work needed.

1.3. New scientific results

1. MEMS fabrication technology is proposed for developing artificial electromagnetic materials and enabling tuneability of their unique

engineering properties at the millimetre wave frequencies where conventional components exhibit high losses.

2. Novel MEMS tuneable high-impedance surface is proposed for different millimetre wave beam steering applications.

3. Analytical model of the multilayer and MEMS tuneable high-impedance surfaces is elaborated.

4. Analytical and numerical study reveals electromagnetic properties of the MEMS tuneable high-impedance surface and behaviour of the devices it is contained in for such applications as analogue type phase shifters and beam steering by the reflective tuneable impedance surface.

5. Measurements of the MEMS-based high-impedance surface as a back-short of a metal rectangular waveguide show resonant high-impedance behaviour of the prototypes, prove feasibility of the analogue type phase shifter and explain loss mechanisms.

6. Measurements over 100 million actuation cycles of the fabricated MEMS varactor designed for the tuneable HIS show no degradation of the MEMS varactor's membrane and high repeatability of the membrane deflection.

7. Measurements of the MEMS tuneable high-impedance surface placed adjacent to a dielectric rod waveguide and controlled by a bias voltage demonstrate analogue type phase shift of up to 70°.

2. High-impedance surfaces

2.1. Introduction: Artificial electromagnetic materials

As it was mentioned in Chapter 1, the high-impedance surface is a particular case of an artificial electromagnetic material, or metamaterial (metasurface) [38],[39],[40]. Artificial electromagnetic materials are periodic or non-periodic two or three dimensional arrangements of structural elements, which exhibits unusual and advantageous electromagnetic properties engineered beforehand by utilising elaborated effective medium analytical models. The models are applicable thanks to the dimensions of the structural element of the artificial electromagnetic material, which are taken to be much smaller than the wavelength of the electromagnetic field the artificial electromagnetic material interacts with, which makes the material effectively homogeneous. The advantageous properties, the artificial electromagnetic materials can provide, are, e.g., negative permittivity [50], negative permeability [51] or both [52],[53],[54], high impedance [49]. The structural elements of the artificial electromagnetic materials can be, e.g., wires [50], metal spheres [54], strips, patches, split-ring resonators [51], transmission lines [55],[56],[57], and their arrangement may provide with inductive, capacitive or resonant electromagnetic response to the interacting field. Some of those arrangements are shown in Fig. 1 and Fig. 2. The term metamaterials came into use in 2000 after the works of Smith et al. [58] on negative permeability and permittivity at microwave. Nowadays, there are attempts to develop metamaterials even at optical frequencies [59]. Despite the fact that the metamaterial concept is quite new, the application prospects of this new technology initiated very active research in this field.

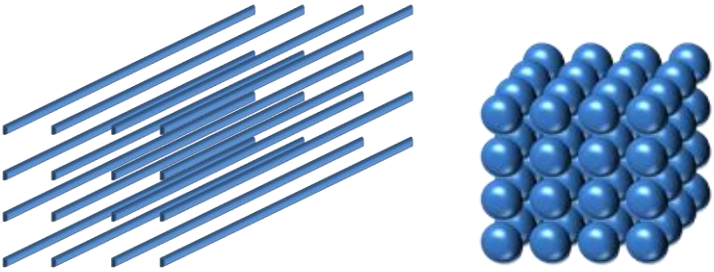

Fig. 1 Different types of artificial electromagnetic materials: 3D wire media (lhs), and 3D lattice of spheres (rhs).

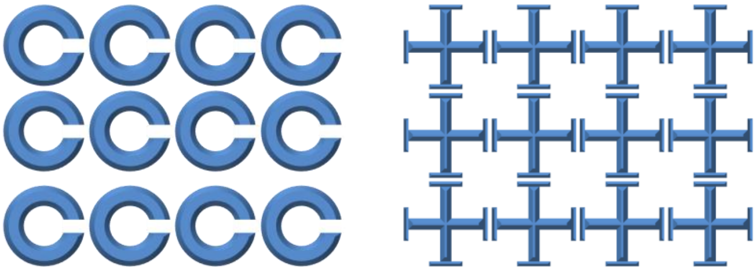

Fig. 2 Different types of artificial electromagnetic materials: split ring resonators (lhs), and Jerusalem crosses (rhs).

Present research in the field of artificial electromagnetic materials has, however, quite long background history [39],[60]. Probably the first work related to the abovementioned concepts was published back in 1892 by Lord Rayleigh [61], who had a goal to demonstrate relation between the refractive index and density of a material derived, almost simultaneously, by Lorenz and Lorentz. For that, he considered a 3-dimentional lattice of electrically small metal spheres, see Fig. 1, as a sample of effectively homogeneous medium modelling molecules of the material, and derived a formula for the refractive index of the medium as a function of the “inductive capacity (analogous of conductivity in the conduction problem)” and a geometrical parameters related to the size and period of the spheres. This concept was later reproduced by Kock for making a lens lighter by replacing heavy high-permittivity refractive material with a periodic arrangement of metal spheres [62].

First work describing negative refraction was published by Mandelshtam in 1944 [63]. Next year Mandelshtam presented a lattice with periodically varying effective permittivity that supports waves with negative group velocity [64] referring to earlier speculations of Lamb back in 1904. Later followed: works of Brillouin and Pierce on left-handed transmission lines with series capacitance and shunt inductances [65],[66]; work of Sivukhin, where he first mentioned a hypothetical medium with negative permittivity and permeability simultaneously [67]; work of Malyuzhinets on a structure similar to composite left/right-handed transmission lines [68], and others.

First thorough study of a medium with simultaneously negative permittivity and permeability was carried out by Veselago [69], who predicted most of fundamental properties of such media. However, practical implementations and possible applications of this work was not fully recognised before the end of the 20th century, when Pendry et al. published their papers on artificial plasma [50], artificial magnetism of an arrangement of split-ring resonators [51] and “perfect lens”, which is a slab with simultaneously negative permittivity and permeability able to focus a diverging light beam [70]. In 2000 Smith et al. realised experimentally first medium with negative permittivity and permeability constituted of thin wire and split-ring resonators [58]. These works engendered massive research on artificial electromagnetic materials during last decade.

2.2. Conventional high-impedance surface

Conventional high-impedance surface consists of a mesh of electrically small metal patches placed above a metal ground plane, see Fig. 3. Each patch may or may not be connected to the ground plane with a metal via. The space between the patches and the ground plane may or may not be filled with a dielectric. The term high-impedance surface (HIS) was first introduced in the PhD thesis of Sievenpiper in 1999 as a structure which reflects the incident plane waves in phase at the resonance frequency, and suppresses all propagating surface waves in a stop-band [49]. The HIS was proposed for improvement of the radiation pattern of an antenna [49], [71], leaky wave radiation [72], electronic beam steering [73], and other applications.

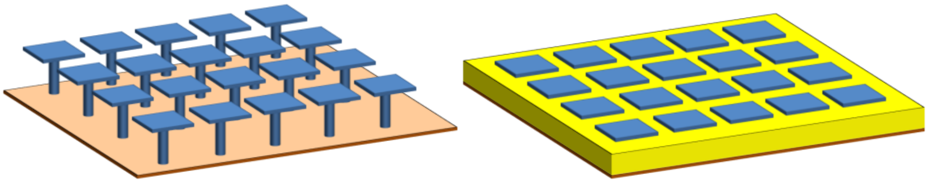

Fig. 3 Conventional high-impedance surface: a mesh of patches connected to a ground plane with metal vias (lhs), and a mesh of patches placed on a thin dielectric substrate with a ground plane, with or without connecting vias (rhs).

Most analytical models of the HIS use the transmission line formalism, where the equivalent surface impedance can be derived as a parallel connection of the capacitive impedance of the mesh of patches and an inductive impedance of the short grounded transmission line section formed between the mesh and the metal ground plane, see, e.g., [38],[49],[P3]. For developing an effective medium analytical model, Sievenpiper used the theory of conforming mapping for finding the capacitance between the neighbouring patches, and calculated the magnetic field through a solenoid of the same thickness as the HIS for finding the efficient inductance of the grounded dielectric substrate [49]. This model is approximate and does not take into account electromagnetic interactions between all metal patches, oblique incidence and dielectric losses.

The HIS evolved, to some extent, from a corrugated metal structure, i.e. a metal slab with a series of vertical slots cut into it, see Fig. 4, which has similar response to the electromagnetic field as the vias connected to the ground plane of the HIS, for a particular field polarisation. The corrugated metal structure was first studied by Cutler [74] in 1944 under military contract to build an antenna satisfying boundary conditions imposed by its location in an airplane [75]. Although classified, this work was circulated to laboratories and was cited later by different authors, e.g., in [76],[77] and [78]. As a result of this work, surface waves were discovered and the reactive corrugated electromagnetic surface able to guide the waves with energy contained very close to a (even bended) surface was developed. The corrugations were spaced close to each other comparing to the wavelength and were considered as short-circuited parallel plate stubs with impedance:

$$Z = Z_0 \tan\left(\frac{2\pi l}{\lambda}\right), \tag{1}$$

where Z_0 is the characteristic impedance, l is the length of the stub, and λ is the wavelength of the field.

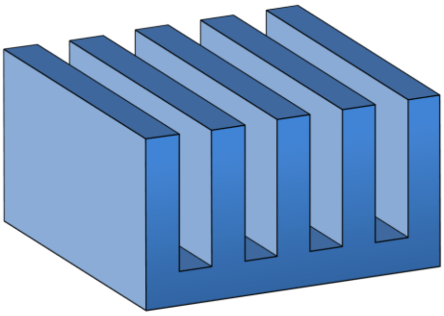

Fig. 4 Corrugated metal structure.

Later corrugated structures were studied, e.g., by Rotman [78] , Elliot [79], Vainshtain [80], Lee and Jones [81] and others. Kildal studied corrugated surfaces with transverse and longitudinal corrugations and introduced terms soft and hard electromagnetic surfaces [82].

Another category of research that has strong influence on the current development of the HIS theory is related to analytical modelling of periodic grids of metal strips or patches. The earliest work on this subject was done back in 1898 by Lamb [83], who studied a periodic grid of metal wires, and derived that, for wires with the diameter much smaller than the wavelength of the normally incident field, the reflection and transmission coefficient depend on the grid periodicity. Scattering from the grid for oblique incidence, wires with a diameter comparable to the grid period and different material of the wires was studied by von Ignatowsky in 1914 [84]. These studies were continued by Kontorovich [85], MacFarlane [86] and others. Later, Kontorovich et al. studied reflection properties of a wire mesh [87], i.e. of an arrangement of two grids of thin metal wires organised orthogonal to each other on the same plane, with an electrical connection in the intersections.

The HIS normally contains a mesh of metal patches with patch size close to, and patch separation much smaller than the period of the mesh, which means that the mesh of metal patches can be considered as a complementary structure of the mesh of thin wires. Consequently, the electromagnetic properties of the mesh of patches can be analysed utilising Babinet's principle, which claims that similar diffraction patterns are produced by two complementary gratings. The principle was extended by Booker to take into account polarisation of the incident field [88], which is now known as Booker's Extension of Babinet's principle. However, in case the metal mesh is placed on a dielectric substrate, the symmetry, which Babinet's principle relies on, is absent. An approximate formula for this case was derived by Compton et al. [89]. Dynamic model that takes into account dielectric substrate under the mesh of patches as well as electromagnetic interactions of all patches was proposed by Tretyakov and Simovski [90]. Luukkonen et al. developed an analytical model of planar grids and meshes and grounded dielectric substrate with and without metal vias, which is accurate even for oblique incidences, the two polarisations of the field, and non-square mesh [91]. According to this model, the effective surface impedance of the mesh of square metal patches for TM- and TE-polarisation of an incident field is, respectively [91]:

$$Z^{TM}{}_{mesh} = -j\frac{\eta_{eff}}{2\alpha}, \tag{2}$$

$$Z^{TE}{}_{mesh} = -j\frac{\eta_{eff}}{2\alpha\left(1-\frac{{k_0}^2}{{k_{eff}}^2}\frac{\sin^2\Theta}{2}\right)}, \tag{3}$$

where Θ is the angle of incidence, k_0 is the free space wave number, the mesh parameter α is:

$$\alpha = \frac{k_{eff}D}{\pi}\ln\left(\frac{1}{\sin\frac{\pi s}{2D}}\right), \tag{4}$$

where D is the period of the mesh, s is the separation of the patches, see Fig. 5, and the effective wave impedance, effective relative permittivity and effective wave number are:

$$\eta_{eff} = \sqrt{\frac{\mu_0}{\varepsilon_0\varepsilon_{eff}}},\ \ \varepsilon_{eff} = \frac{\varepsilon_1+\varepsilon_2}{2},\ \ k_{eff} = k_0\sqrt{\varepsilon_{eff}} \tag{5}$$

where ε_1 and ε_1 are relative permittivity of the media above and below the structure. Usually $\varepsilon_1 = 1$ (for air) and ε_2 is the permittivity of the dielectric substrate, which the mesh is placed on, or also $\varepsilon_2 = 1$, in case the patches are hold by the vias connected to the ground.

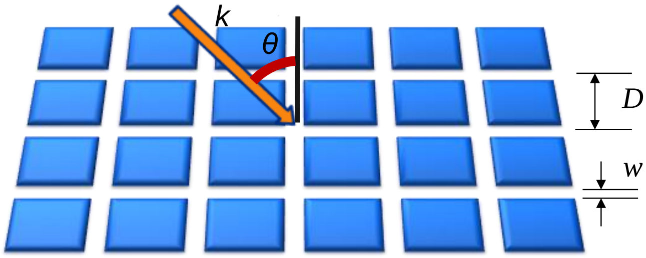

Fig. 5 Capacitive mesh of metal patches.

Consequently, for normal incidence, the effective surface impedance of the mesh of square metal patches transforms to an easy formula:

$$Z_{mesh} = \frac{1}{j\omega C_{eff}}, \tag{6}$$

where ω is the frequency of the wave and C_{eff} is the effective capacitance of the square mesh:

$$C_{eff} = \frac{2D\varepsilon_0\varepsilon_{eff}}{\pi}\ln\left(\frac{1}{\sin\frac{\pi s}{2D}}\right). \tag{7}$$

The analytical model derived in [91] considers lossless media below and above the mesh of patches, i.e., when relative permittivities are:

$$\varepsilon_{1,2} = \varepsilon'_{1,2} - j\varepsilon''_{1,2}\,, \;\; \varepsilon''_{1,2} = 0. \tag{8}$$

Still, if the dielectric losses are small, i.e.,

$$\varepsilon''_{1,2} \ll \varepsilon'_{1,2}, \tag{9}$$

Equations (2)-(4) give quite an accurate result if we rewrite Equation (5) as follows:

$$\eta_{eff} = \sqrt{\frac{\mu_0}{\varepsilon_0\varepsilon_{eff}}}\,, \;\; \varepsilon_{eff} = \frac{\varepsilon'_1+\varepsilon'_2}{2}, \;\; k_{eff} = k_0\sqrt{\frac{\varepsilon_1+\varepsilon_2}{2}}\;. \tag{10}$$

For large dielectric losses, i.e. when $\varepsilon'_{1,2}$ and $\varepsilon''_{1,2}$ are of the same order, the solution given by Equations (2)-(4) and (10) is approximate.

As it was mentioned before, the equivalent surface impedance of the HIS can be derived as a parallel connection of the capacitive impedance of the mesh of patches and an inductive impedance of the short grounded transmission line section formed between the mesh and the metal ground plane:

$$\frac{1}{Z_{eff}} = \frac{1}{Z_{mesh}} + \frac{1}{Z_d}. \tag{11}$$

If the mesh is placed on a dielectric substrate without vias connecting the patches to the ground plane, the input impedance of the grounded dielectric of thickness h, for normal incidence, can be written as (see, e.g. [92]):

$$Z_d = j\sqrt{\frac{\mu_0\mu_2}{\varepsilon_0\varepsilon_2}}\tan(k_0 h\sqrt{\varepsilon_2\mu_2}), \tag{12}$$

where ε_2 and μ_2 are the relative permittivity and permeability of the dielectric. Equation (12) takes into account dielectric losses of the substrate, and the Taylor series expansion can be used for analysing loss mechanism of the HIS, which is given in Section 2.3.2 and [P3]. For the case of very thin substrate comparing to the wavelength, Equation (12) transforms to ($\mu_2 = 1$):

$$Z_d \approx j\omega\mu_0 h, \tag{13}$$

which is similar to an approximate formula for the effective inductance of the HIS $L_{eff} \approx \mu_0 h$, derived by Sievenpiper by calculating magnetic field through an imaginary solenoid that purports to be formed by the metal patches, pins and ground plane [49]. Accurate effective impedance model of the grounded dielectric substrate with metal vias is derived in [91].

The HIS is a resonant structure, and at a resonance frequency

$$\omega_0 = \frac{1}{\sqrt{L_{eff} C_{eff}}} \tag{14}$$

the effective surface impedance is very high. In a lossless case the effective impedance is purely imaginary and tends to ±∞ at the resonance frequency, see Fig. 6, and for a dielectric substrate with losses the impedance is complex, see Fig. 7. The effective impedance of a structure is related to the reflection coefficient for a normally incident field as follows [92]:

$$R = \frac{Z_{eff} - \eta}{Z_{eff} + \eta}, \tag{15}$$

where η is the free space impedance. Consequently, the phase of the reflection coefficient changes in the vicinity of the resonance frequency smoothly from 180° (as for a metal plane) at lower frequencies where the effective impedance of the HIS is inductive, to 0° at the resonance, and back to -180° at higher frequencies where the effective impedance is capacitive, see Fig. 8. It should be noted, that the frequency dependence of the reflection phase of the HIS is practically independent on the loss tangent of the dielectric substrate, but the reflection amplitude has a dip at the resonance frequency if there are substrate losses, see Fig. 9.

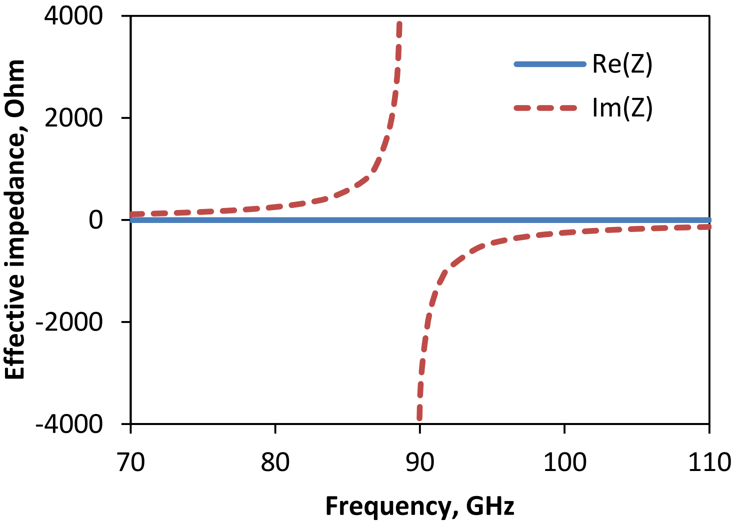

Fig. 6 Effective surface impedance of the HIS: lossless case, calculated.

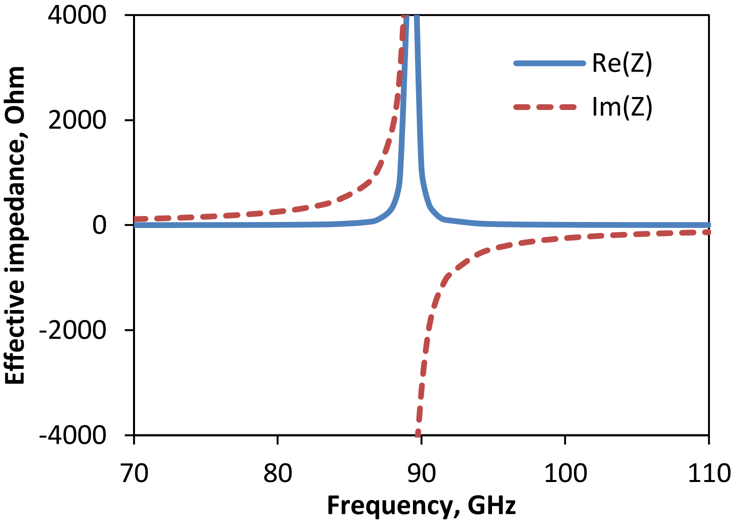

Fig. 7 Effective surface impedance of the HIS: dielectric substrate loss tangent 0.06, calculated.

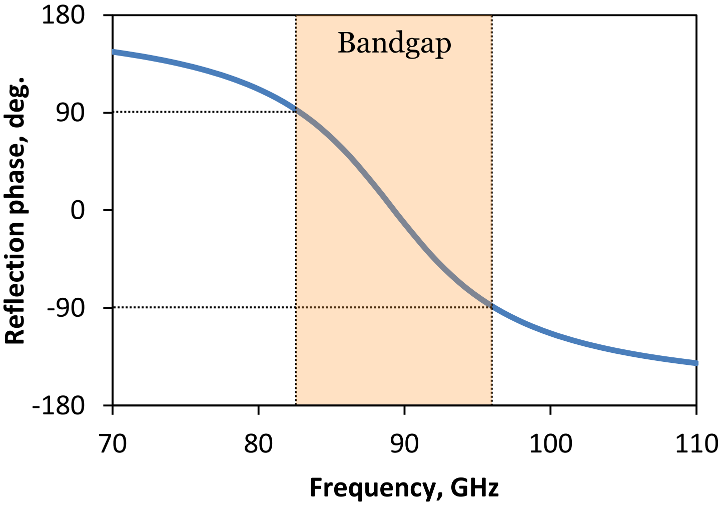

Fig. 8 Phase of the reflection coefficient of the HIS, calculated. The bandgap frequency range is shaded.

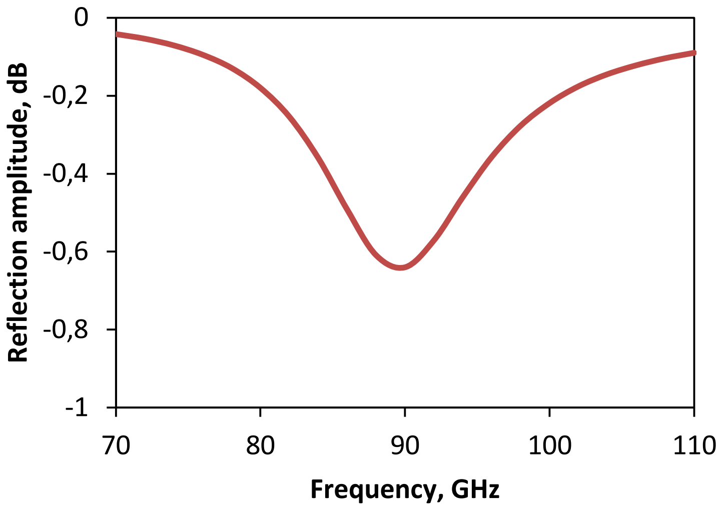

Fig. 9 Amplitude of the reflection coefficient of the HIS with dielectric loss tangent 0.06, calculated.

A bandgap of the HIS can be defined as the frequency range, where the phase of the reflection coefficient is between -90° and 90°. As it was mentioned before, one of the applications of the HIS is improvement of an antenna radiation pattern [71],[93],[94]. If the antenna is placed adjacent to the HIS and the operating frequency belongs to the bandgap of the HIS, the image currents will interfere constructively with the currents of the antenna, and the antenna gain will be increased. When the impedance of the HIS is equal to the free space impedance, i.e., 377 Ω, the radiation power drops down to the half of its maximum achievable when the HIS is at the resonance frequency and the image currents are in-phase with the antenna currents. For the lossless case, the phase of the reflection coefficient of ±90° corresponds to the surface reactive impedance equal to ±377 Ω, and for the HIS with losses this corresponds to the absolute value of the surface reactive impedance equal to 377 Ω.

If the HIS contains vias connecting the metal patches to the ground, the surface wave are suppressed within the bandgap, hence there is no sideway radiation, and the radiation pattern becomes smoother [95].

In the case when equivalent characteristic impedance of the HIS, $\sqrt{L_{eff}/C_{eff}}$ is much smaller than the free space impedance η, the bandgap can be calculated using the following equation [71]:

$$\frac{\Delta\omega}{\omega} = \frac{\sqrt{\mathrm{L_{eff}/C_{eff}}}}{\eta} \tag{16}$$

Concequently, as it can be seen from Equations (7) and (13), the bandgap is larger for thicker dielectric substrate, smaller period, and larger patch separation, which can be used for designing the HIS for a particular application.

2.3. Multilayer high-impedance surface

2.3.1. Effective surface impedance model

A multilayer HIS, as a first step towards the MEMS tuneable HIS, see Section 2.4, was studied analytically, numerically and empirically in [P1]-[P3], which present the first ever detailed treatment of a multilayer HIS. The multilayer HIS consists of three metal layers and two dielectric layers: grounded dielectric substrate and two capacitive meshes of metal patches shifted relative to each other in the direction of ***E***-field and separated by a thin dielectric film, see Fig. 10.

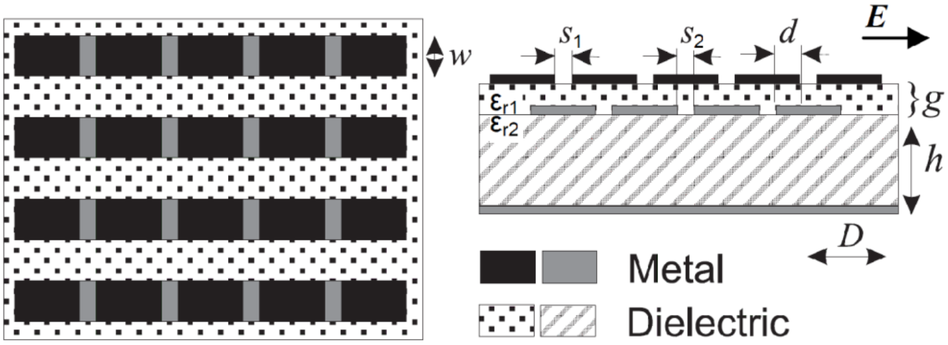

Fig. 10 Multilayer HIS (not to scale).

Since the size of the patches of the multilayer HIS is much smaller than the wavelength of the incident field (typically period D is ca. $\lambda/10$), we can analyse the electromagnetic behaviour of the structure in terms of effective surface impedance. Furthermore, we can consider the structure as a combination of 4 layers:

- the grounded dielectric substrate of permittivity ε_{r1} with input impedance Z_d,
- the capacitive mesh of lower metal patches placed on the interface of two dielectrics of permittivity ε_{r1} and ε_{r2} with input impedance Z_{mesh1},
- the array of parallel plate capacitors between the lower and upper metal patches filled with a dielectric film of permittivity ε_{r2} with input impedance Z_{pp}, and
- the second capacitive mesh of patches placed on the interface of the dielectric of permittivity ε_{r1} and air with input impedance Z_{mesh2}.

The effective circuit model of the multilayer HIS is a parallel connection of the four abovementioned effective impedances. Consequently, the total effective input impedance of the multilayer HIS is:

$$Z_{tot} = \left(Z_d{}^{-1} + Z_{mesh1}{}^{-1} + Z_{pp}{}^{-1} + Z_{mesh2}{}^{-1}\right)^{-1}, \qquad (17)$$

where the expressions for Z_d, Z_{mesh1} and Z_{mesh2} are given above, see Equations (12) and (2)-(10).

In order to analyse the mechanism of losses of the multilayer HIS, we need to derive an analytical model taking into account complex permittivities of the dielectrics [P3]. Due to the relatively large separations s_1 and s_2 between the patches (in the fabricated prototype, which will be described in the next section: D=120 µm, s_1=43 µm, s_2= 33 µm, d=22 µm), the impedance of the meshes is much smaller than Z_{pp}, and the influence of the real part of $Z_{mesh1,2}$ can be neglected for moderate dielectric losses. However, both Z_d and Z_{pp} should include complex permittivities (dielectric loss tangent). For Z_d it is useful to apply the Taylor series expansion to Equation (12):

$$Z_d = j\sqrt{\frac{\mu_0\mu_2}{\varepsilon_0\varepsilon_2}}\tan\left(k_0 h\sqrt{\varepsilon_2\mu_2}\right) =$$

$$= \frac{1}{3}\eta_0 (k_0 h)^3\, \varepsilon_2' \tan\delta_2 + j\eta_0 k_0 h\left(1 + \frac{1}{3}(k_0 h)^2 \varepsilon_2'\right) + O\left((k_0 h)^5\right) \qquad (18)$$

From this, we can derive the effective inductance of the multilayer HIS and the effective series resistance of the dielectric substrate [P3]:

$$L_{eff} \approx \mu_0 h\left(1 + \frac{1}{3}(k_0 h)^2 \varepsilon_2'\right), \;\; R_d \approx \frac{1}{3}\eta_0 (k_0 h)^3\, \varepsilon_2' \tan\delta_2. \qquad (19)$$

If the thickness of the substrate is much smaller than the wavelength of the incident field, we can take only the first term of the Taylor series, and the equivalent inductance of the grounded dielectric substrate and the whole multilayer HIS is, as mentioned before,

$$L_{eff} \approx \mu_0 h. \qquad (20)$$

This leads to an important conclusion that for a relatively thin substrate the reflection phase and the resonance frequency of the HIS do not depend on the complex permittivity of the dielectric substrate. The approximate Equation (20) becomes violated, however, very fast with increasing thickness of the grounded substrate, and the deviation between the approximate and exact value is proportional to ε_2', i.e., to the real part of the relative permittivity of the dielectric substrate. The series resistance of the dielectric substrate is proportional to permittivity and loss tangent of the medium, and the third power of the substrate thickness. Hence, the HIS loss increases dramatically with increased thickness.

The impedance of the parallel plate capacitor Z_{pp} formed by overlapping between the upper and lower patches consists of capacitance and active resistance:

$$Z_{pp} = \frac{1}{j\omega C_{pp}} + R_{pp}. \qquad (21)$$

For capacitors with very thin gap comparing to the dimensions of the overlapping, e.g., $g < 0.01\sqrt{d \cdot w}$, which holds for the fabricated prototype with g=0.24 µm, the capacitance can be calculated with a standard parallel plate capacitance formula, because the field is very strong between the plates and fringing fields can be neglected. However, for a large gap of the capacitor, e.g., $g > 0.1\sqrt{d \cdot w}$, the fringing fields start to play an important role, and they should be taken into account. One of the approximate expressions for the parallel plate capacitors, which include the fringing fields, is Palmer's formula [96]:

$$C_{pp} = \frac{\varepsilon_0 \varepsilon'_1 w d}{g}\left[1 + \frac{g}{\pi d} + \frac{g}{\pi d}\ln\frac{\pi d}{g}\right]\left[1 + \frac{g}{\pi w} + \frac{g}{\pi w}\ln\frac{\pi w}{g}\right]. \qquad (22)$$

The resistance of the parallel plate capacitor is:

$$R_{pp} = \frac{g}{\omega \varepsilon_0 \varepsilon'_1 w d \cdot \tan\delta}. \qquad (23)$$

The equations given above allow calculating the total effective surface impedance taking into account dielectric losses.

2.3.2. Influence of the material electromagnetic parameters on the performance of the HIS

In the multilayer HIS, the field is concentrated in the gap between the upper and lower array of patches. If this gap is filled with a dielectric film, the properties of the dielectric play a crucial role in the multilayer HIS electromagnetic response [P3]. Fig. 11 and Fig. 12 show the phase and amplitude of the calculated reflection coefficient of the multilayer HIS for different values of the dielectric film loss tangent for a multilayer HIS with following parameters: D=120 µm, d=22 µm, w=60 µm, g=0.24 µm, h=21 µm, see Fig. 10. When the loss tangent of the dielectric film between the upper and lower layer is larger than 0.057, the real part of the reflection coefficient is always negative and the reflection phase never reaches value of 0° varying moderately around 180°. When the loss tangent is equal to 0.057, the absolute value of the surface impedance at the resonant frequency is equal to the free space wave impedance and the reflection coefficient is zero. In this case, the reflection phase exhibits a 180° jump as it can be seen in Fig. 11. The reflection coefficient curve on the Smith chart in this case touches at the resonance frequency the centre of the chart, see Fig. 13. For the dielectric material with lower losses, i.e., with loss tangent less than 0.057 for the considered case, at the resonance frequency the real part of the reflection coefficient is positive, the surface impedance is higher than the free space wave impedance, and the reflection phase is equal to 0°. Fig. 11 also shows that the resonance frequency does not depend on the dielectric substrate loss tangent, because the series inductive impedance of the substrate ωL_{eff} is much larger than the series resistance R_d for the case of thin substrates, as it was mentioned in the previous section.

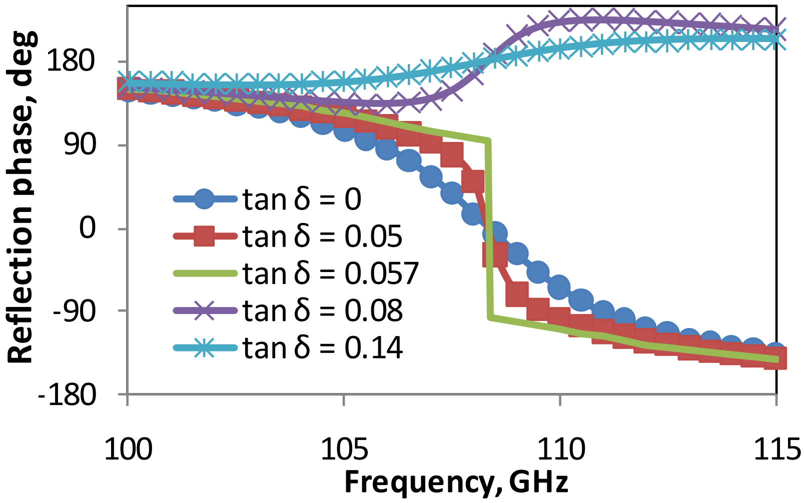

Fig. 11 Phase of the reflection coefficient of the multilayer HIS for different values of the loss tangent of the dielectric between the upper and lower patches, calculated.

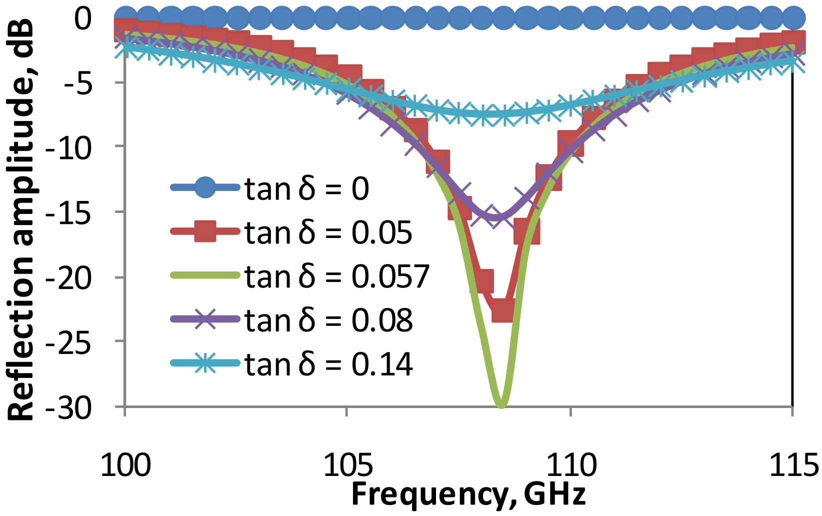

Fig. 12 Amplitude of the reflection coefficient of the multilayer HIS for different values of the loss tangent of the dielectric between the upper and lower patches, calculated.

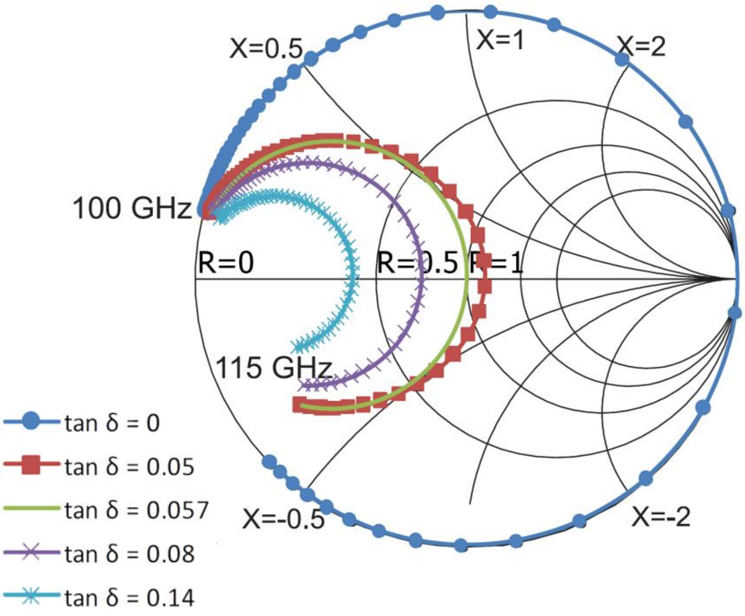

Fig. 13 Reflection coefficient of the multilayer HIS for different values of the loss tangent of the dielectric between the upper and lower patches; Smith chart, calculated.

2.3.3. Fabrication and measurement of the multilayer HIS

We have fabricated a multilayer HIS on an SU8 substrate where the gap between the upper and lower patches is filled with silicon dioxide film, see Fig. 14 [P1]. The period of the structure is 120 μm, the height of the dielectric substrate is 20 μm, and the gap between the upper and lower patches is 0.23 μm, and overlapping of the patches is 22 μm × 60 μm. The patches' material is aluminium.

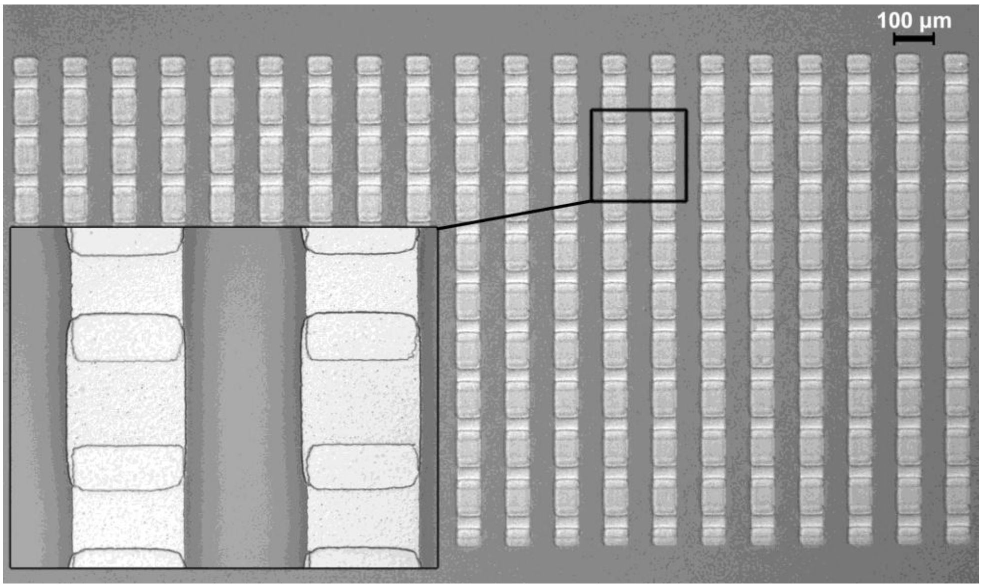

Fig. 14 Optical image of the fabricated multilayer HIS [P1].

The fabricated structure was characterised by placing is as a backshort of a rectangular metal waveguide WR-10 in order to measure S_{11}-parameter. The measurement results of the reflection phase and amplitude are presented in Fig. 15 together with the analytical and numerical results, where the loss tangent of silicon dioxide film is 0.06. The Smith chart of the S_{11}-parameter is given in Fig 16. The results show good agreement. The resonance, which can be clearly observed at the Smith chart, occurs at 106 GHz. For the frequencies on the lower limit of the measured frequency range, the phase of the reflection coefficient is about 180°, and the amplitude of the reflection coefficient is close to 0 dB, which means that the impedance of the structure is very low and it performs as a metal sheet. In the vicinity of the resonance frequency the phase starts to change by about 50° and the reflection amplitude goes down to -7 dB, which means that the absolute value of the surface impedance increases. However, the reflection phase does not reach 0° at the resonance, as it should be for a HIS, indicating that the absolute value of the surface impedance does not reach the free space wave impedance. This can be explained by large losses in the SiO_2 film between the patches, as it was discussed in the previous section. Eliminating the dielectric from the layer between the patches by replacing film-separated patches with an arrangement of MEMS varactors allows reducing the HIS loss and enables its reconfigurability.

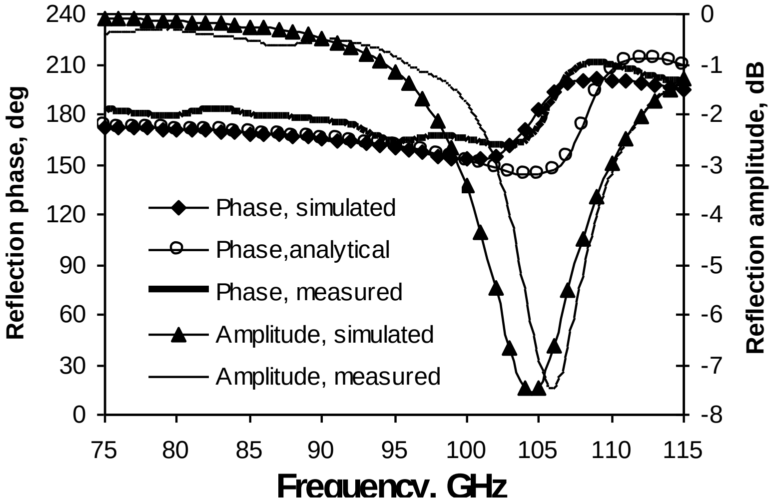

Fig. 15 Measured, calculated and simulated S_{11} of the multilayer HIS with SiO_2 as a thin film between the upper and lower patches [P1].

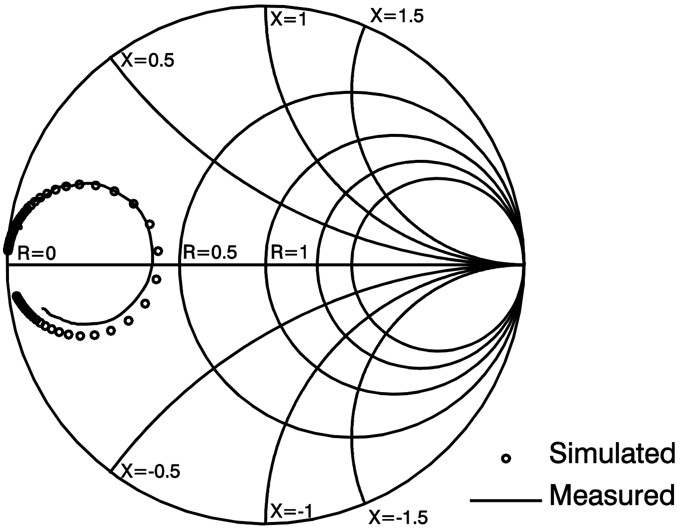

Fig. 16 Smith chart of the measured and simulated results of the S_{11}*-parameter of the multilayer HIS [P1].*

2.4. MEMS tuneable high-impedance surface

2.4.1. Introduction

We proposed to use MEMS varactors in order to enable low-loss tuneability of the HIS at millimetre wavelength for different applications [P1]. First implementation of tuneability of the conventional HIS was demonstrated by Sievenpiper and was based on integration of diode varactors between the patches of the HIS [97]. In this configuration the structure becomes very similar to the one developed by Lam et al. back in 1988 [98], which is a grid of diode varactors placed adjacent to a metal ground plane and proposed for phase shifting applications. Higgins et al. demonstrated a Ka-band phase shifter based on metal waveguide with tuneable impedance sidewalls controlled by InP triple quantum barrier varactors [99]. In contrast with diode varactors and other conventional reconfigurable components (e.g. based on ferroelectrics), utilisation of MEMS varactors allows manufacturing low loss tuneable devices even at high – millimetre and submillimetre wave – frequencies, e.g. phase shifters [48]. Examples of demonstrated up to date MEMS tuneable artificial electromagnetic materials include: analogue tuneable terahertz filter based on an arrangement of split-ring resonators with MEMS comb-drive [100], tuneable Q-band filter based on a coplanar waveguide with embedded complementary split-ring resonators controlled by MEMS switch [101], X-band and Ku-band switchable composite righ/left-handed transmission line [102], [103].

2.4.2. Design of the MEMS tuneable HIS

The proposed MEMS tuneable HIS consists of a two-dimensional periodical arrangement of coupled MEMS capacitors, much smaller than the wavelength of an incident field, placed on a grounded dielectric substrate, see Fig. 17, [P4].

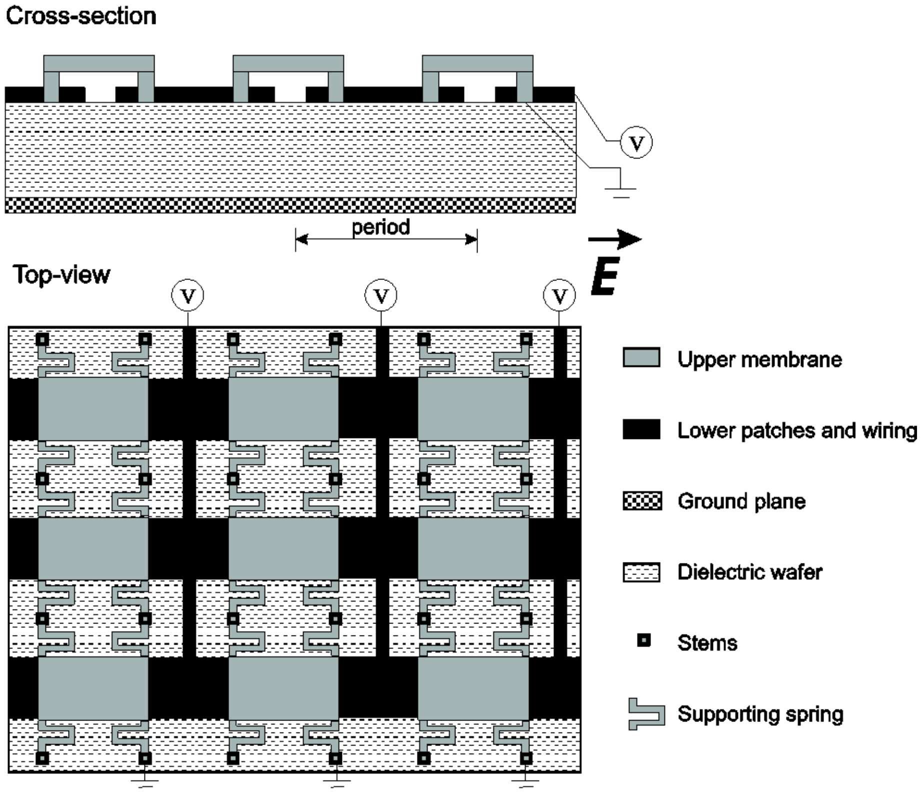

Fig. 17 Design of the MEMS tuneable high-impedance surface (not to scale) [P4].

The structure is a particular case of the multilayer HIS, discussed in Section 2.3, if we replace the thin film between the upper and lower metal patches with air. The structure is resonant thanks to the capacitive response of the mesh of the MEMS varactors and inductive response of the thin grounded dielectric substrate. At the resonance frequency, the effective surface impedance becomes very high, and the phase of the reflection coefficient is equal to 0° instead of 180°, as for a metal surface. For mechanical purposes, the upper membranes are now fixed on four stems with supporting springs, which introduce parasitic inductance to the capacitive layer of MEMS varactors. The upper membranes and lower patches are connected in rows to the bias voltage sources through the stems and by the bias wires, respectively. The connection is done perpendicular to the E-field in order to avoid current flow along the bias wires and consequent short-circuiting of the capacitive mesh.

If an actuation voltage is applied to the MEMS varactors, the resonance frequency shifts. At the same time the phase of the reflection coefficient of the HIS changes, as well as the phase factor of the propagation constant of the reflected field. This can be used in development of analogue type phase shifters where the MEMS tuneable HIS is embedded into waveguiding structures, see Chapters 3 and 4. Also, the proposed MEMS tuneable high-impedance surface can be used directly as a smart reflecting beam steering surface if each row of the MEMS capacitors is controlled independently, and an electrically tuneable gradient of the reflection phase is induced on the surface, see Chapters 5. Changing the gradient of the reflection phase throughout the surface will change the direction of the field reflected from the high-impedance surface.

Following restrictions was applied to the design of the MEMS tuneable HIS due to the fabrication constrains:

a. The thickness of the substrate should be not less than 100 μm, otherwise a 4-inch wafer will be very difficult to handle. However the thickness should be less than one quarter of the guided wavelength in order to provide the inductive response to the incident field.
b. The feature size should be not less than 1 μm, which is a limit of manufacturing precision.
c. The gap of the MEMS varactors should be within 0.5 – 3 μm range.

Next sections of this chapter describe properties of the designed MEMS varactors, provide an analytical model of the MEMS tuneable HIS, show numerical results of its electromagnetic behaviour, depict fabrication procedure and report results of the reliability study of the fabricated MEMS varactors.

2.4.3. MEMS varactors and actuation voltage

MEMS capacitive switches and varactors are frequently and successfully used for fabrication of low-loss distributed true-time delay phase shifters [104], filters [105], VCO [106], impedance tuners [107], etc. Typically, a fixed-fixed configuration of the MEMS parallel plate capacitor is used, see Fig. 18. Electromechanical analysis of such structures allows calculating the string constant of the membrane, dependence of the gap on the applied voltage and the pull-down voltage of the MEMS capacitor [41]. When a voltage is applied to the electrode, the membrane bends down, and the capacitance between these plates increases. The spring constant of the fixed-fixed membrane can be represented as a sum of two parts. First part is caused by the stiffness of the upper plate, and second part is due to the residual stress in the membrane induced during the fabrication. The value of the spring constant component due to the residual stress is highly dependent on the fabrication process. In the worst cases it can be equal or even more than the stiffness component of the spring constant resulting to a higher value of the voltage needed for the actuation of the MEMS capacitor. Decreasing of the residual stress of the MEMS membrane is described in Section 2.4.6 and [P5]. The stiffness of the membrane, in turn, can be reduced by implementing serpentine-type springs for fixing the membrane on the stems, see Fig. 19.

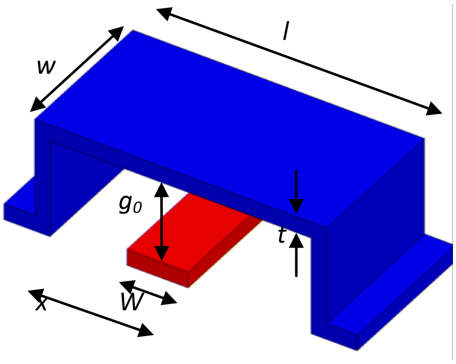

Fig. 18 MEMS parallel plate capacitor: fixed-fixed beam.

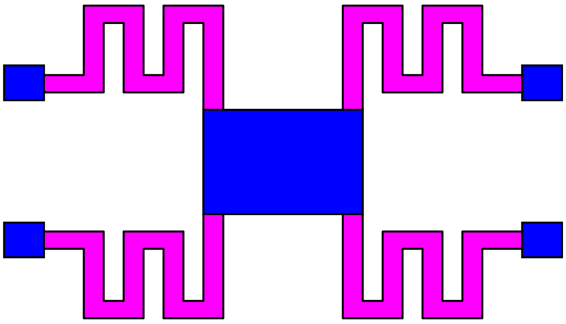

Fig. 19 Serpentine-type springs for decreasing the stiffness of the membrane of the MEMS parallel plate capacitor.

The dependence of the gap g between the membrane and the pull-down electrode of a parallel plate MEMS capacitor on the applied voltage can be found be equating the electrostatic force, which exists on the plates, to the mechanical restoring force due to the stiffness of the membrane. This results in [41]:

$$V = \sqrt{\frac{2k}{\varepsilon_0 W w} g^2 (g_0 - g)}, \tag{24}$$

where k is the spring constant, W is the width of the actuation electrode, w is the width of the fixed-fixed membrane, g_0 is the initial gap between the actuation electrode and the membrane. The dependence is shown in Fig. 20.

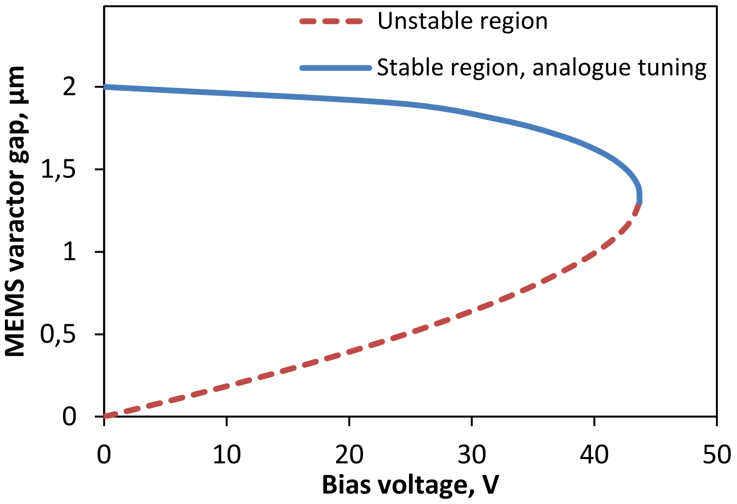

Fig. 20 Dependence of the gap between the membrane and the pull-down electrode of a parallel plate MEMS capacitor on the applied voltage

As we can see in Fig. 20, the gap between the membrane and the actuation electrode of the parallel plate MEMS varactor can be tuned in an analogue way only by one-third of its initial value, after which the membrane collapses to the actuation electrode due to predominance of the electrostatic forces over the restoring forces. This does not depend on the dimensions of the MEMS varactor and can be derived directly from Equation (23). Consequently, the maximum capacitance ratio between the upper and lower state of the gradually tuned MEMS varactor cannot exceed 1.5. In practice the capacitance ratio 1.5 for the standard configuration of the MEMS capacitor is seldom attained.

To increase the gradual tuning capacitance ratio, a special complex design of the MEMS varactors for HIS is chosen [P9]. The idea is to segregate two functions and have:

- lower patches of thickness t_p for creating an effective capacitance of the HIS between the membrane and lower patches for the electromagnetic field, and
- a separate thin actuation electrode of thickness t_e placed between the lower patches for applying the bias voltage between the membrane and the electrode, see Fig. 21, [P9].

This way, the restriction imposed by electrostatics does not influence the RF domain, and the MEMS capacitance, which represents a major part of the HIS effective capacitance, can be tuned by a larger factor than 1.5. This is because the limitation of the one-third of the initial gap applies to the gap $g_o+t_p-t_e$ between the membrane and the actuation electrode, see Fig. 21, whereas the upper surface of the lower patch can be very close to the membrane at the lowest stable down-state of the membrane. For example, for g_o = 1 µm, t_p = 1 µm and t_e= 0.2 µm, the maximum theoretical capacitance ratio is 2.5. Referring to Fig. 20, the described design of the MEMS varactor behaves as if we shift the axis of ordinates upwards by t_p-t_e, or, e.g., by 0.8 µm. Increasing of the capacitance ratio allows attaining much larger tunability of the effective surface impedance of the MEMS-based HIS, which is needed for optimal performance of the proposed applications, see next sections.

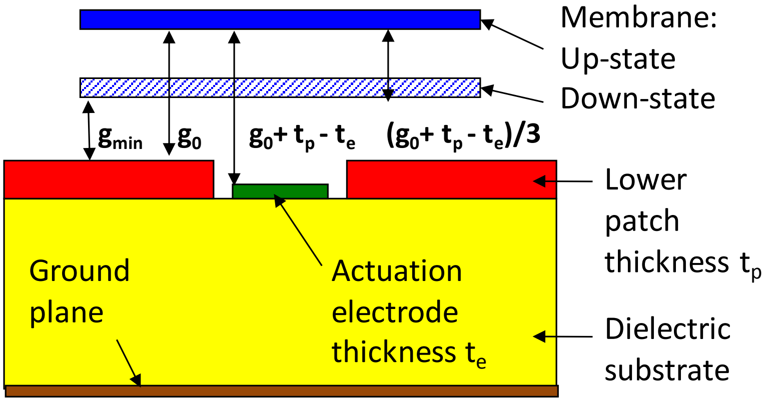

Fig. 21 Schematic design of the MEMS varactor with extended tuning range for MEMS tuneable HIS [P9].

The exact dimensions of the designed MEMS varactors and all other parameters of the fabricated HIS are given in Appendix A. Using formulas from [41], the actuation voltage of the MEMS varactor described above with these dimensions is estimated to be 40 V.

2.4.4. Analytical model and numerical simulations

The analytical model of the MEMS tuneable HIS follows from the effective surface impedance model of the multilayer HIS given in Section 2.3.1 and [P3]. The difference between the two cases is that for the MEMS tuneable design the thin dielectric film between the upper and lower patches is replaced with an air gap between the MEMS membrane and the lower patches. Consequently the MEMS tuneable HIS can be considered as a combination of 4 layers connected in parallel:

- the grounded dielectric substrate of permittivity ε_{r1} with input impedance Z_d, see Equation (12),
- the capacitive mesh of lower metal patches placed on the interface of the dielectric substrate of permittivity ε_{r1} and air ($\varepsilon_{r2} = 1$) with input impedance Z_{mesh1}, see Equations (2)-(7)
- the array of parallel plate capacitors between the MEMS membrane and lower metal patches filled with air with input impedance Z_{pp}, and
- the second mesh of MEMS membranes placed in air with input impedance Z_{mesh2}.

In contrast with the multilayer HIS, the effective impedance of the parallel plate MEMS varactors Z_{pp} is purely imaginary, i.e. its resistance $R_{pp} = 0$, see Equation (21). Capacitive part of the impedance of the mesh of the membranes Z_{mesh2}, calculated with Equations (2)-(7), becomes smaller for the MEMS tuneable HIS because the effective relative permittivity of the media around the membranes is approximately equal to one. Hence in many cases this effective capacitance may be neglected. However, since the membrane is supported with meander springs, Z_{mesh2} has inductive component, which can be either estimated with approximate formulas given, e.g., in [108], or found by extracting the circuit parameters from numerical simulations.

Fig. 22 shows the phase of the reflection coefficient of the MEMS tuneable HIS calculated according to the analytical model given above. The frequency dependence of the reflection phase for the gap of the MEMS varactors equal to 3.3 μm is given in Fig. 22 (lhs). The dependence of the reflection phase on the gap of the MEMS varactors for the operating frequency 77 GHz is given in Fig. 22 (rhs). Results of numerical simulation of the reflection coefficient phase of the MEMS tuneable HIS with the same dimensions carried out with Ansoft HFSS are depicted in Fig. 23, and show good agreement with the analytical results.

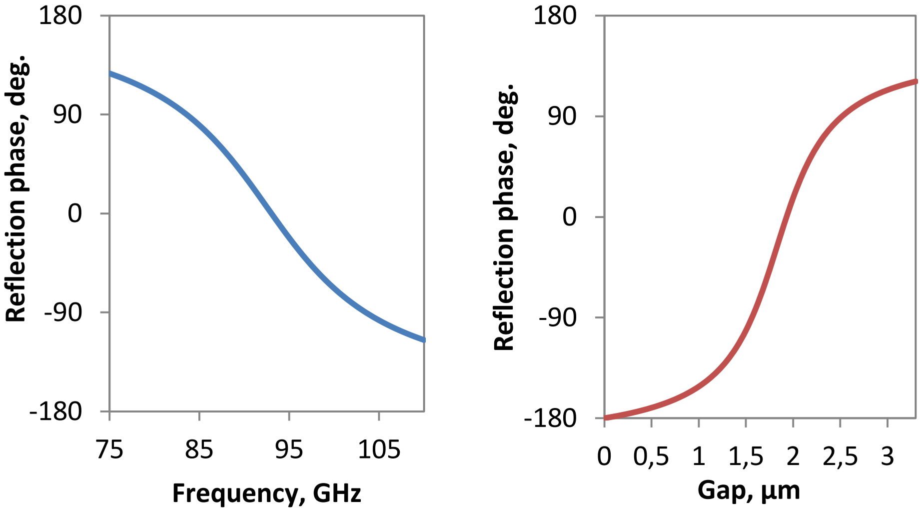

Fig. 22 Calculated phase of the reflection coefficient of the MEMS tuneable HIS: frequency dependence (lhs, the gap of the MEMS varactors is 3.3 µm), and dependence on the gap of the MEMS varactors (rhs, the frequency is 77 GHz).

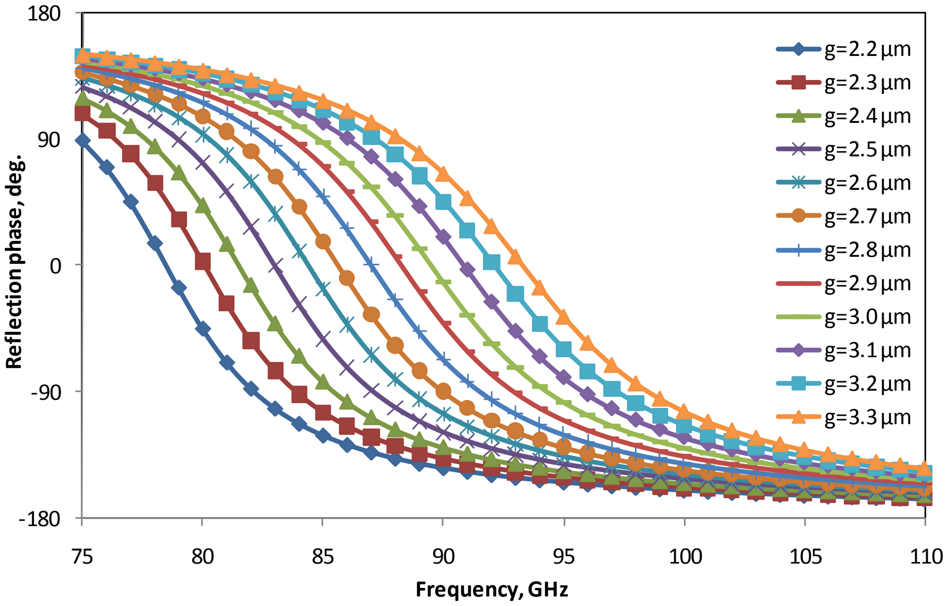

Fig. 23 Simulated phase of the reflection coefficient of the MEMS tuneable HIS for different values of the gap of the MEMS varactors.

As it was discussed in Section 2.3.2, the electromagnetic parameters of the dielectric substrate (permittivity and loss tangent) do not affect the performance of the multilayer HIS (i.e. the resonance frequency and the losses), if the substrate thickness is much smaller than the guided wavelength. However, if the thickness becomes comparable to the wavelength, especially high losses in the dielectric substrate can influence the HIS loss at the resonance. The effect becomes even more pronounced if the lower patches are placed close to each other, while the MEMS capacitance is small either due to the small overlapping or large gap between the membrane and the lower patches. In this case the electromagnetic field is concentrated not only in the air gap of the MEMS varactors (dash field lines in Fig. 24), but also enters the dielectric substrate (solid field lines in Fig. 24) due to the capacitive mesh formed by the lower patches. The field strength in the dielectric, however, decreases rapidly with increasing separation between the lower patches, i.e. with decreasing capacitance of the mesh.

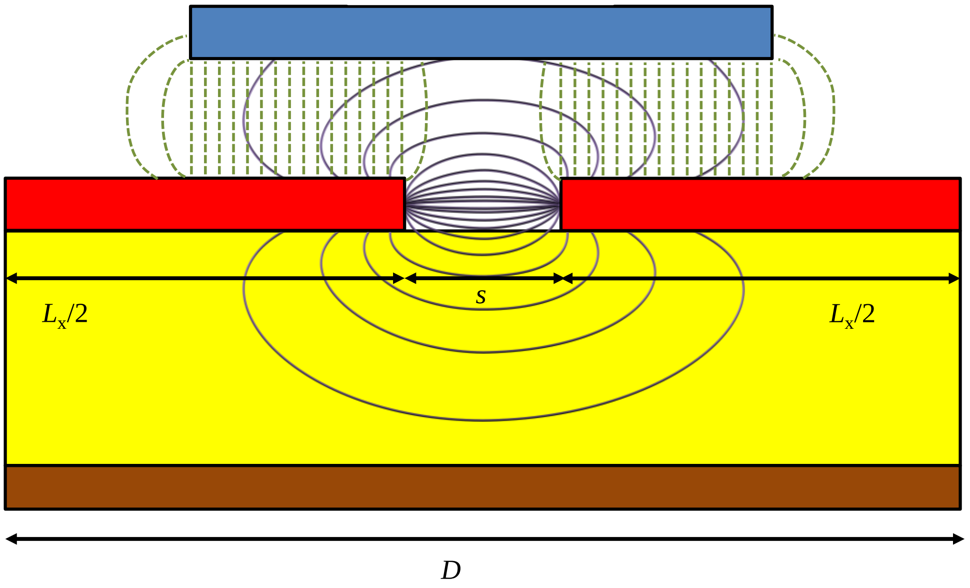

Fig. 24 Schematic side view of the MEMS tuneable HIS with field lines.

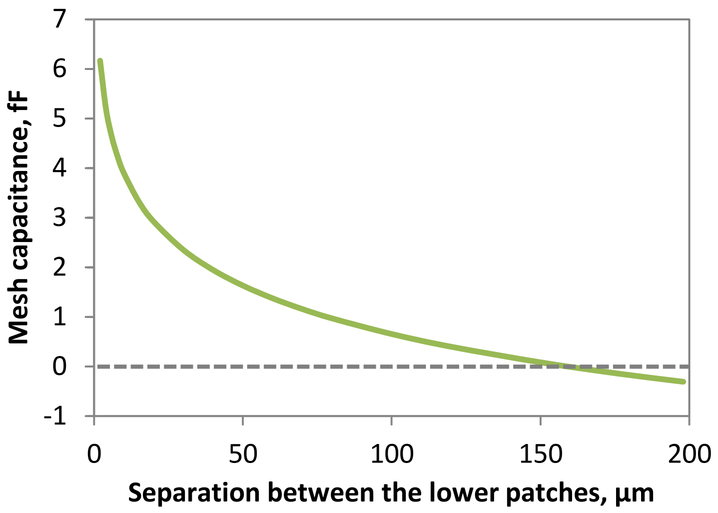

Fig. 25 Calculated dependence of the effective capacitance of the mesh of patches on the separation s between the patches, with constant period D = 250 µm; patch length L_x is variable: $L_x = D – s$.

As we can see in Fig. 25, the effective capacitance of the mesh of patches (see Fig. 5), calculated with Equation (7), decreases dramatically when the patch separation changes from 2 µm to 20 µm. After that the slope is more gradual, and eventually the curve passes to the negative region at 160 µm, which means that the equivalent impedance of the mesh of patches becomes inductive. Although Equation (7) is accurate only for separation much smaller than the period of the mesh, which in this case is 250 µm, the results shown in Fig. 25 agree very well with the simulations of the complete MEMS tuneable HIS with the variable separation between the lower patches. Fig. 26 shows dependence of the resonance frequency and the resonance loss (amplitude of the S_{11}-parameter) on the separation between the lower patches of the MEMS tuneable HIS, with constant overlapping and gap between the MEMS membrane and the lower patches, as well as with a constant period of the HIS. For keeping the overlapping, i.e. the MEMS capacitance, constant, the length of the MEMS membrane is variable: it increases the same amount as the separation between the lower patches. As we can see in Fig. 26, the resonance frequency of the HIS increases due to decrease of the mesh capacitance of the lower patches, which is a part of the total efficient capacitance of the MEMS tuneable HIS. (The resonance frequency is obviously inversely proportional to the square root of the effective capacitance and effective inductance.) The change is dramatic for small values of the separation and more gradual for larger values of the separations, similarly to the change of the mesh capacitance in Fig. 25. Also we can notice a decrease of the resonance frequency for the patches separation above 155 µm, which means that the effective impedance of the mesh of patches becomes inductive and is growing as we can see from calculated results of Fig. 25.

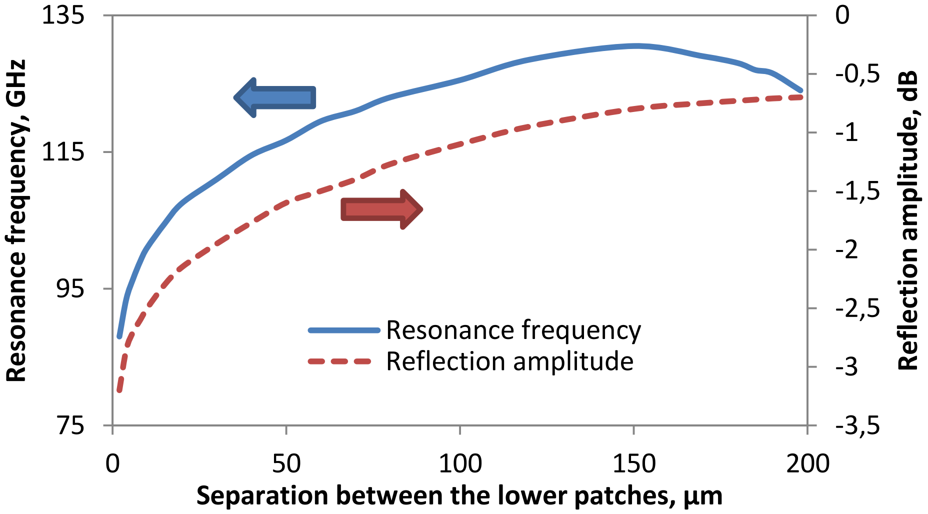

Fig. 26 Simulated dependence of the resonance frequency and the resonance loss (amplitude of the S_{11}-parameter) on the separation between the lower patches of the MEMS tuneable HIS.

The loss at the resonance frequency is decreasing always with increasing separation between the lower patches due to the decreased field strength inside the dielectric substrate. The loss tangent of the dielectric substrate for the simulation is taken to be 0.003, which is the value of the loss tangent we measured at W-band in an open resonator characterising the substrate used in the fabrication of the MEMS tuneable HIS. The conclusion is that it is advantageous to use a larger value of the separation between the lower patches while designing the MEMS tuneable HIS in order to avoid field concentration in the dielectric and to decrease losses at the resonance.

As it was mentioned before, the springs supporting the MEMS membrane introduce additional inductance to the HIS. The simulation results below show how strong the effect is for different parameters of the spring (length, width, and spacing, see Fig. 27). Both the resonance frequency of the MEMS tuneable HIS and its loss at the resonance is affected.

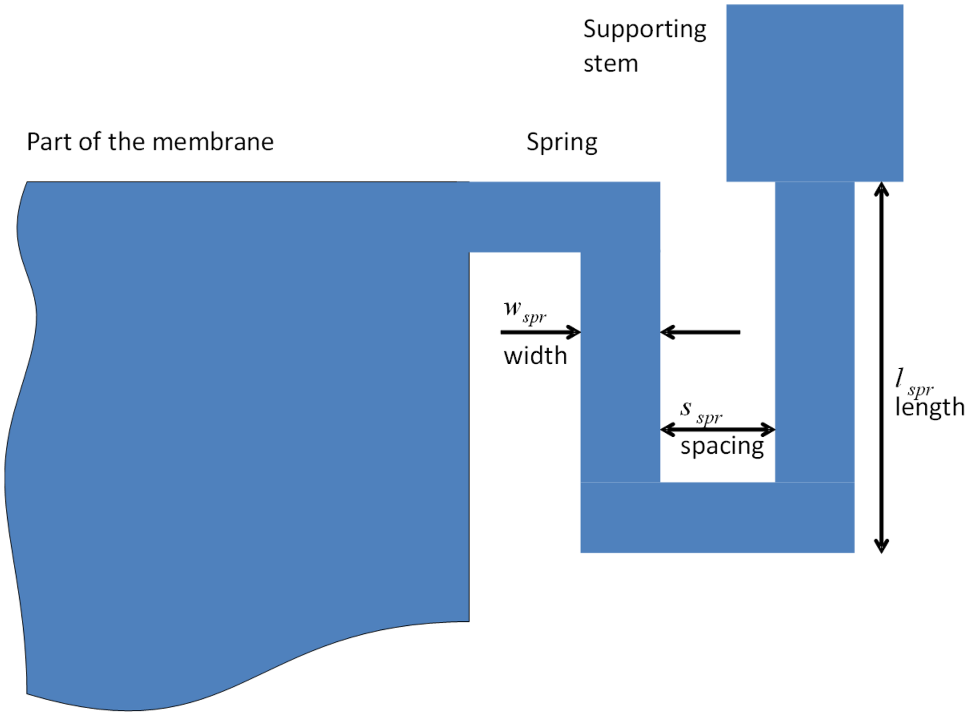

Fig. 27 Schematic top view of the spring supporting a membrane of the MEMS tuneable HIS (compare also with Fig. 17).

Fig. 28 and Fig. 29 show simulated frequency dependence of the phase and amplitude of the reflection coefficient of the MEMS tuneable HIS for different lengths of the springs, which support the MEMS membrane. Obviously, the additional inductance introduced by the springs to the total effective inductance of the MEMS tuneable HIS is larger for a larger length l_{spr} of the spring. This results in decreasing the resonance frequency of the HIS with increasing length of the spring. At the same time, the resonance becomes less sharp and the losses at the resonance decrease. Similarly, the resonance frequency and the resonance losses decrease if the spacing s_{spr}

between the turns of the spring increase, which increases the spring inductance and the total effective inductance of the MEMS tuneable HIS, see Fig. 30. On the other hand, increasing the width of the spring w_{spr} results in decreasing of the spring inductance and sheet resistance, thus increasing the resonance frequency and decreasing the resonance losses, see Fig. 31.

The conclusion is that it is beneficial, from the point of view of losses, to choose longer springs with larger separation between the spring's turns. This goes in the same direction with the requirements towards smaller spring stiffness and consequently smaller actuation voltage.

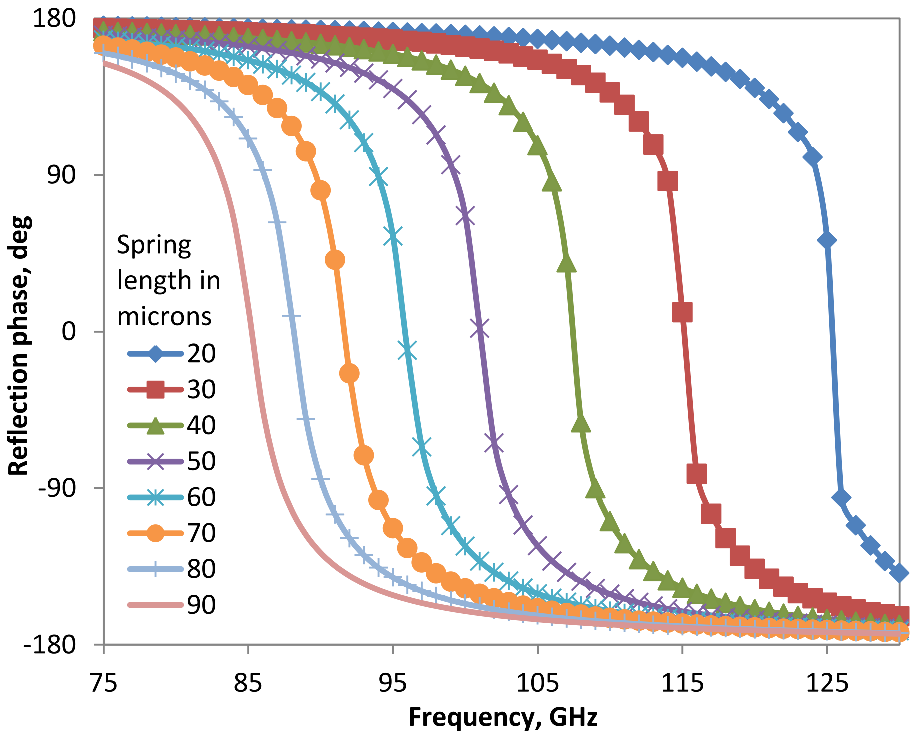

Fig. 28 Simulated frequency dependence of the phase of the reflection coefficient of the MEMS tuneable HIS for different lengths l_{spr} of the spring supporting the MEMS membrane.

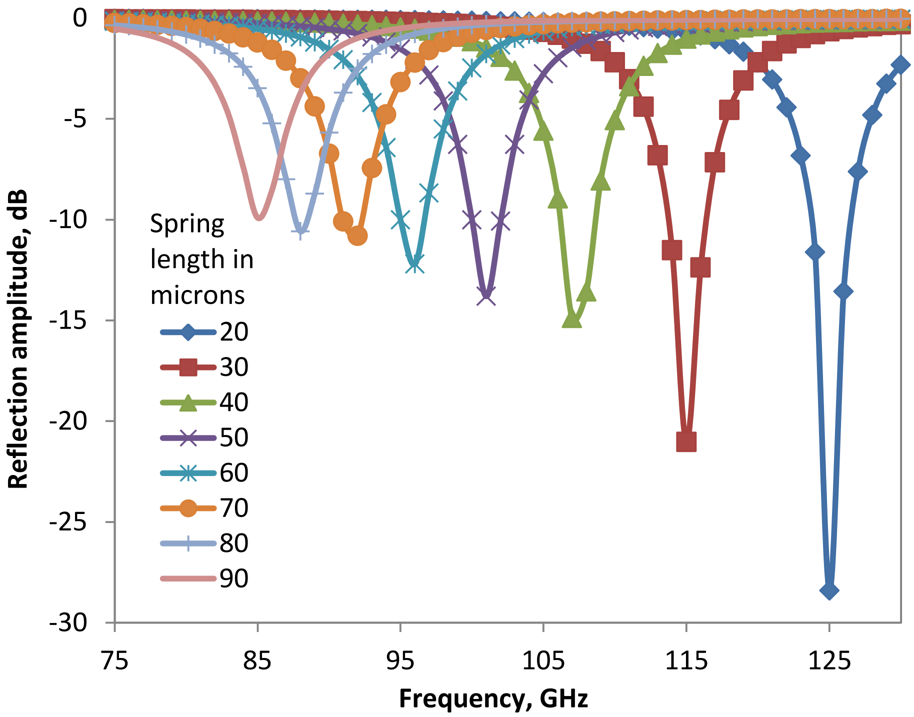

Fig. 29 Simulated frequency dependence of the reflection coefficient amplitude of the MEMS tuneable HIS for different lengths l_{spr} of the spring supporting the MEMS membrane.

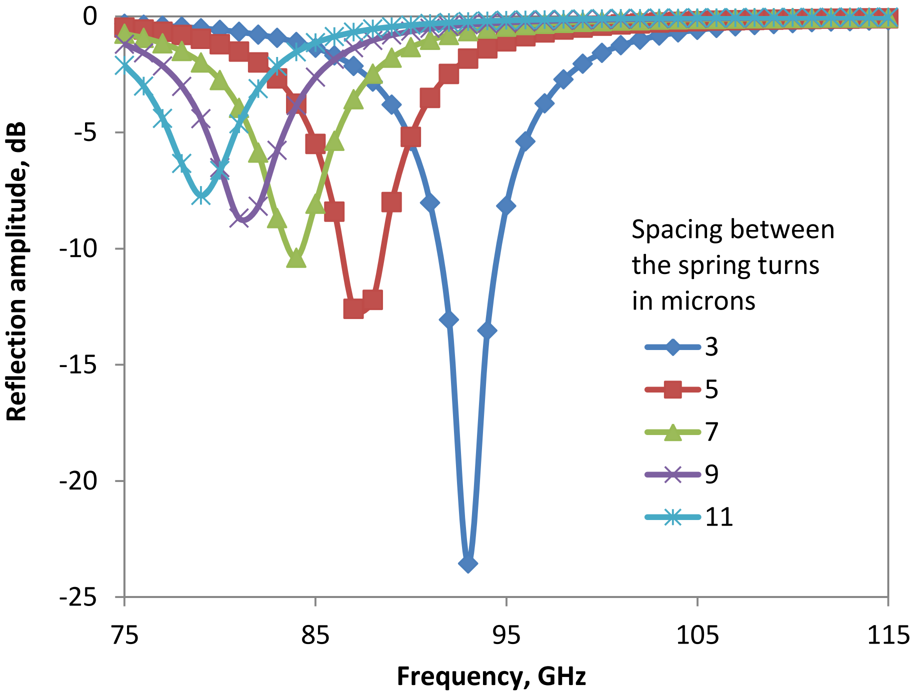

Fig. 30 Simulated frequency dependence of the reflection coefficient amplitude of the MEMS tuneable HIS for different spacing s_{spr} between the turns of the spring supporting the MEMS membrane.

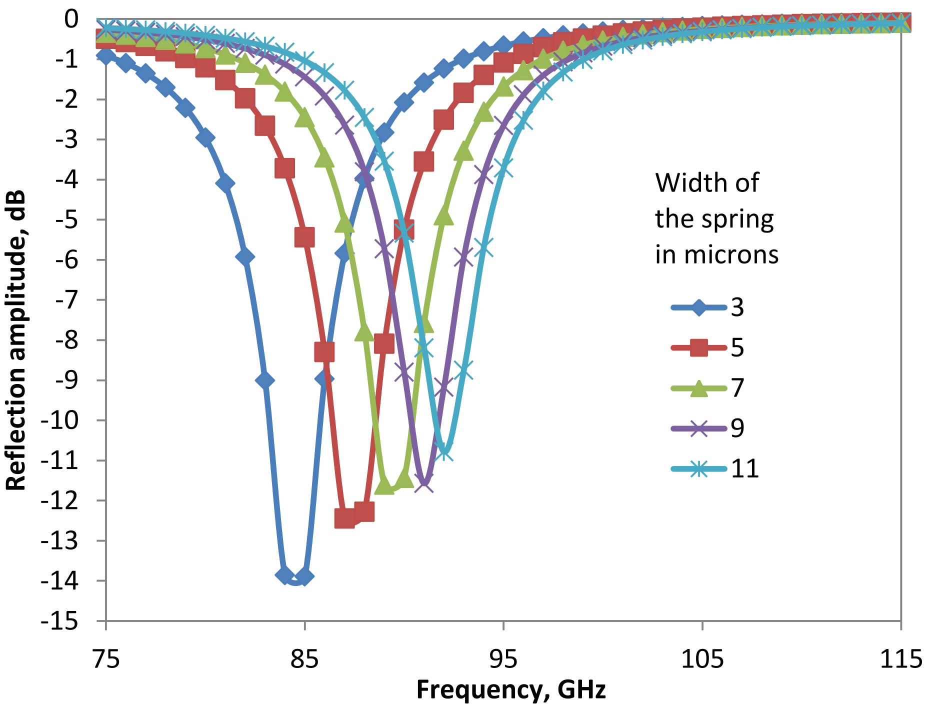

Fig. 31 Simulated frequency dependence of the reflection coefficient amplitude of the MEMS tuneable HIS for different width w_{spr} of the spring supporting the MEMS membrane.

2.4.5. Fabrication

Few rounds of fabrication of the MEMS tuneable HIS prototypes of different size and for different applications were carried out, see [P2], [P4]-[P6], [P8]-[P9] and Fig. 32. The material of the dielectric substrate is ORMOCER® for the prototypes described in [P2], microwave glass AF-45 in [P4]-[P5], and high-resistivity silicon for all other prototypes. The detailed description of the fabrication process used in all but the first fabrication round is given in [P5]. Dimensions of all elements of the prototypes described in [P4]-[P6], [P8]-[P9] are given in Appendix A. The key dimensions are:

- the dielectric substrate thickness 110 µm;
- the period of the HIS 250 µm (for phase shifting applications) and 350 µm (for direct beam steering application);
- the initial gap of the MEMS varactors 2 µm;
- the overlapping between the MEMS membrane and lower patches (MEMS capacitance area) 140 µm × 25 µm.

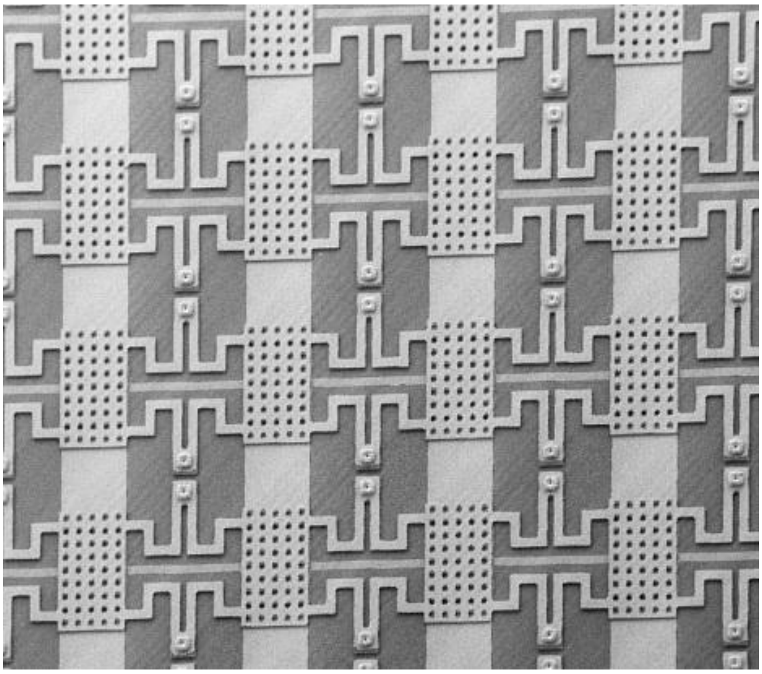

Fig. 32 Fabricated prototype of the MEMS tuneable HIS.

One of the most important novel MEMS design features developed for manufacturing MEMS tuneable HIS is a triple layer membrane used to form the MEMS varactors of the HIS. Each membrane consists of a one-micron thick monocrystalline silicon layer covered from both top and bottom with half-micron layers of gold. The fabrication process is designed in such a way, that gold deposition on the monocrystalline core of the membrane is done under the same conditions and in antipodal direction, see Fig. 4 in [P6]. The symmetry of the fabrication process balances out the stress induced in the membrane by the metallisation, which allows attaining previously unmatched near-perfectly flat and high-reliability metal-coated mono-crystalline silicon membranes. The flatness of the large 200 µm × 140 µm membrane was measured to be within the range of 20-40 nm. The interferometric measurements of the membrane deflection and the curvature while applying the bias voltage show no plastic deformation of the membrane and smooth change of the gap of the MEMS varactor [P6]. The life-cycle and repeatability measurement of the membrane deflection over 100 million actuation cycles shows virtually no degradation of the membrane actuated and unactuated position [P6]. After 100 million actuation cycles the measurement was stopped without observing any failure of the MEMS varactor.

Most of the MEMS membranes are fabricated with few-micron holes for etching out the sacrificial layer under the membrane for releasing the membrane, see Fig. 32. Consequently, the overlapping area between the membrane and the lower patch decreases, which may result in decrease of the capacitance formed by the membrane and patch. However, if the diameter of the etching holes is less than three times larger than the gap between the membrane and patch, the fringing fields formed on the edge of the holes compensate the decrease of the overlapping area, and the MEMS capacitance is not changing [41]. Fig. 33 shows the simulated dependence of the resonance frequency on the etching holes size of the MEMS tuneable HIS, for a MEMS varactor gap equal to 2 µm. As we can see, up to the hole radius equal to 3 µm (or diameter 6 µm) the resonance frequency of the MEMS tuneable HIS does not change at all. Since the resonance frequency depends in this simulation only on the effective MEMS capacitance, this result perfectly corresponds to the previously given reference that etching holes with the diameter three times larger than the gap does not affect the MEMS capacitance. For a larger hole diameter, the capacitance starts to decrease rapidly, i.e. the resonance frequency of the MEMS tuneable HIS increases. For visualising the above-mentioned effect of the fringing capacitance, the calculated resonance frequency is plotted in Fig. 33 for the case when the area of the solid metal parallel plate capacitance A_{solid} is smaller than the area of the simulated MEMS varactors A_{MEMS} by the total area of all etching holes A_{holes} ($A_{\mathrm{solid}} = A_{\mathrm{MEMS}} - A_{\mathrm{holes}}$). The difference between the two curves in Fig. 33 accounts for the effect of the etching hole fringing capacitance.

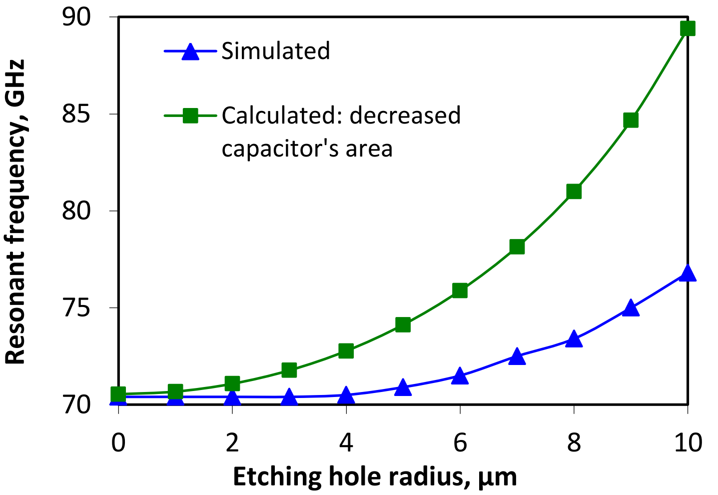

Fig. 33 Dependence of the resonance frequency of the MEMS tuneable HIS on the size of the etching hole in the MEMS membrane. Simulated (as fabricated) and calculated (for a capacitor with decreased overlapping area by the total area of the membrane etching holes).

2.5. Conclusion

In this chapter we have discussed conventional and novel MEMS tuneable high-impedance surfaces.

The historical background and major milestones, which led to development of the conventional HIS as an artificial electromagnetic material, are presented in Section 2.1.

The present state-of-the-art of the analytical model of the conventional HIS is given in Section 2.2. The conventional HIS consists of a periodic mesh of metal patches placed on an electrically thin dielectric substrate with a ground plane. The electromagnetic behaviour of the HIS can be analysed by an effective surface impedance model due the fact that the period of the structure is much less than the wavelength of the field interacting with the HIS. Consequently, the structure can be considered as effectively homogeneous. Also the analytical model assumes that the HIS can be subdivided into two layers connected electrically in parallel: the capacitive mesh of the patches and grounded dielectric substrate (with or without vias). Total surface impedance of the HIS can be calculated through the effective impedances of these layers, which can be found for different polarisations and angles of incidence. The surface impedance of the HIS becomes very high at the resonance frequency and the phase factor of the reflection coefficient changes from 180° to 0°.

In Section 2.3 a multilayer HIS is introduced and studied as a first step towards a MEMS tuneable HIS. A multilayer HIS consists of two meshes of patches separated by a thin dielectric film, shifted relatively to each other, and placed on a grounded dielectric substrate. The effective surface impedance analytical model is developed and used for analysis of the influence of the material electromagnetic parameters on the performance of the HIS. It was found that large dielectric loss of the thin film separating the capacitive meshes of patches decreases dramatically the impedance of the HIS at the resonance frequency. Consequently, if the surface impedance is less than the free space wave impedance, the reflection phase of the HIS never reaches a value of 0°, varying moderately around 180°. This was proved experimentally by measuring S_{11}-parameter of the fabricated multilayer HIS.

Section 2.4 is devoted to the novel MEMS tuneable HIS, which consists of a periodical two-dimensional arrangement of coupled MEMS varactors placed on a grounded dielectric substrate. Both design of the structure and fabrication constraints are presented. MEMS varactors are studied with a focus on decreasing of the actuation voltage and increasing of the tuning range. A special design of the MEMS varactor with an additional actuation electrode is elaborated for large analogue tuning of the MEMS membrane defection. Particular distinctions of the analytical model of the MEMS tuneable HIS comparing to the model of the multilayer HIS given in Section 2.3 are discussed. Numerical simulations are used to study: the dependence of the MEMS tuneable HIS reflection coefficient on the deflection of the MEMS membrane; the dependence of the HIS performance on the separation between the lower patches; and the dependence of the HIS performance on the parameters of the spring supporting the membrane. Finally, fabrication of the prototypes is discussed together with a reliability and repeatability study of the MEMS varactor. The life-cycle measurement of the MEMS varactor's membrane deflection over 100 million actuation cycles shows virtually no degradation. In addition, the influence of the etching holes in the membranes is evaluated and proved to have no effect on the resonance frequency of the MEMS tuneable HIS if the diameter of the holes is less than three times larger than the initial gap of the MEMS varactor.

Next chapters are devoted to different applications of the described MEMS tuneable HIS.

3. MEMS tuneable HIS for millimetre wave beam steering applications

3.1. Introduction

As it was mentioned in Section 2.4.2, MEMS tuneable HIS can be used in electronic beam steering applications either as a phase shifting element in waveguiding structures or as a reflecting beam steering surface. First demonstration of beam steering with a HIS was done by Sivenpiper et al. in 2001 [73]. In that work a plane wave of frequency in the range of 2.8 – 5.0 GHz was reflected by the HIS in a desired direction by changing the gradient of the reflection phase over the surface. The gradient of the surface impedance (and hence the gradient of the reflection phase) was controlled by diode varactors placed between neighbouring patches of the HIS.

Another way of using HIS in beam steering applications is development of phase array antennas based on an assembly of waveguiding structures, where the phase is controlled by embedded tuneable HIS. A Ka-band phase shifter based on a metal waveguide with tuneable HIS introduced in the sidewalls of the waveguide was demonstrated by Higgins et al. in 2003 [109]. The HIS (called in the paper "electromagnetic crystal") was controlled by InP triple quantum barrier varactors.

In this chapter we discuss development of the analogue type phase shifters based on the MEMS tuneable HIS embedded in waveguides and report feasibility study of a large MEMS-based HIS as a reflective beam steering surface.

3.2. Analogue type phase shifters based on the MEMS tuneable HIS integrated in a rectangular metal waveguide

3.2.1. Analytical and numerical analysis

Section 3.2 is devoted to analogue type phase shifters based on the MEMS tuneable HIS integrated in a rectangular metal waveguide. Three different designs of the HIS integration are considered: side walls integration, integration in the corner of a waveguide bend, and backshort integration, see Sections 3.2.1.1-3.2.1.3. Two first design options form a transmission type phase shifter, and the third one a reflection type phase shifter. The reflection type phase shifter with a HIS is prototyped and characterised, see Section 3.2.2.

3.2.1.1. Side walls integration

Fig. 34 shows design of a transmission type phase shifter based on a rectangular metal waveguide with MEMS tuneable HIS integrated in the narrow side walls of the waveguide. The reconfigurable impedance of the waveguide section with embedded HIS affects the propagation constant of the wave in this section providing a phase shifting mechanism.

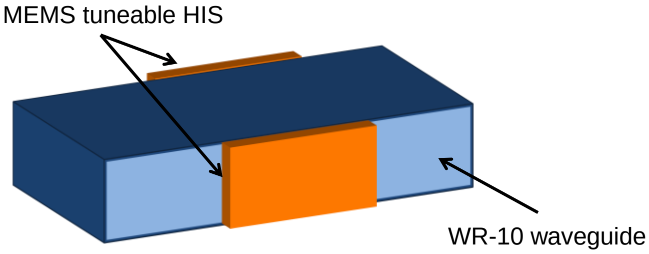

Fig. 34 Design of a transmission type phase shifter based on a rectangular metal waveguide with MEMS tuneable HIS integrated in the narrow side walls of the waveguide.

When the high-impedance surface is tuned from the high impedance state (resonance) to the low impedance state (out-of-resonance), the phase difference of the waves exiting the waveguide can be calculated as follows:

$$\Delta\varphi \approx \Delta k_z \cdot l \ , \tag{25}$$

where l is the length of the impedance surface and Δk_z is the wave number difference equal to the parallel to the *E*-field projection of the difference of the wave vector in the HIS section $\vec{k}_{HIS}$ (which is the same as the wave vectors in free space $\vec{k}_0$) and the wave vector in the metal waveguide $\vec{k}_{wg}$ [92]:

$$\Delta k_z = \left|\vec{k}_{HIS} - \vec{k}_{wg}\right| = k_0 - \sqrt{k_0^{\,2} - \left(\frac{\pi}{a}\right)^2} = \frac{2\pi f}{c} - \sqrt{\left(\frac{2\pi f}{c}\right)^2 - \left(\frac{\pi}{a}\right)^2} \ , \tag{26}$$

where a is the width of the waveguide cross-section (perpendicular to the *E*-field), f is the frequency of the wave and c is the speed of light.

If only one impedance surface is embedded into the narrow wall of the metal waveguide instead of two opposite HIS as in Fig. 34, the wave vectors in the HIS section is [110]:

$$k_{HIS} = \sqrt{k_0^{\,2} - \left(\frac{\pi}{2a}\right)^2} \ , \tag{27}$$

and the resulting phase difference of the wave exiting the waveguide will be significantly smaller.

Depending on the realisation of the bias voltage of the MEMS varactors of the HIS, there may be two ways of controlling the phase of the phase shifter. First, if all MEMS varactors are connected to a common actuation voltage source, the impedance of the surface can be changed gradually by a gradual change of the gap of the MEMS varactors. In this case the phase shift is purely analogue. Second, the MEMS varactors may be connected to a different actuation voltage sources (row-by-row perpendicular to the wave vector). In this case, the MEMS varactors may be actuated in a switch regime, reconfiguring a part of the surface from a high impedance state to a low impedance state. This allows changing the effective length of the high impedance section of the waveguide, which affects the phase shift. The phase shift will be of a quasi-analogue type, with a phase shift step depending on the period of the HIS.

Results of numerical simulations of the phase shift, which appears when the HIS is tuned from a low impedance state to a high impedance state, is shown in Fig. 3 of [P6] and correspond very well to the analytical results calculated with Equations (25)-(26). In W-band the maximum achievable phase shift can be in the range of 150°-210° for a 6 mm long HIS. The phase shift is larger for a smaller wavelength and has linear dependence on the length (or effective length) of the high impedance inclusion, see Fig. 4 in [P1], as implied by Equation (25).

3.2.1.2. Integration in the corner of a waveguide bend

Another possibility for development of an analogue type phase shifter is introducing a MEMS tuneable HIS in the corner of a bend waveguide, see Fig. 35.

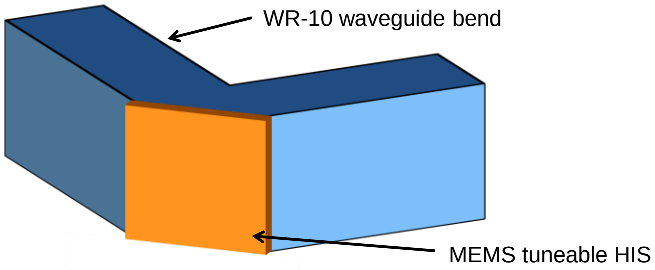

Fig. 35 Design of a transmission type phase shifter based on a rectangular metal waveguide bend with MEMS tuneable HIS integrated in the corner of the bend (E-bend option).

Results of numerical simulations of the phase shift which occurs when the MEMS tuneable HIS is tuned from the high impedance state to the low impedance state at a particular operation frequency is shown in Fig. 36 for both E-bend and H-bend of the rectangular metal waveguide WR-10. In order to reduce computational time, the high impedance state is emulated by a perfect magnetic conductor (PMC), and the low impedance state by a perfect electric conductor (PEC).

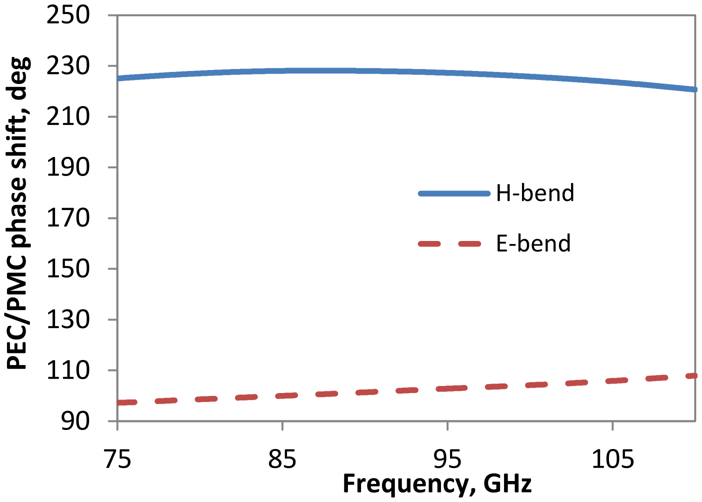

Fig. 36 Phase shift, which occurs when the tuneable impedance surface embedded in the waveguide bend is tuned from the PEC state to the PMC state; simulated for H-bend and E-bend.

Return loss of the phase shifter is quite large when the impedance surface is in a low impedance state, whereas there is a wide frequency band of low return loss for a high impedance state of the surface in the corner of the waveguide bend, see Fig. 37. In order to decrease this loss, which is due to reflections, another configuration of the waveguide bend can be considered and optimised by fine-tuning the dimensions of the bend, see Fig. 38 (design) and Fig. 39 (S_{11}-parameters).

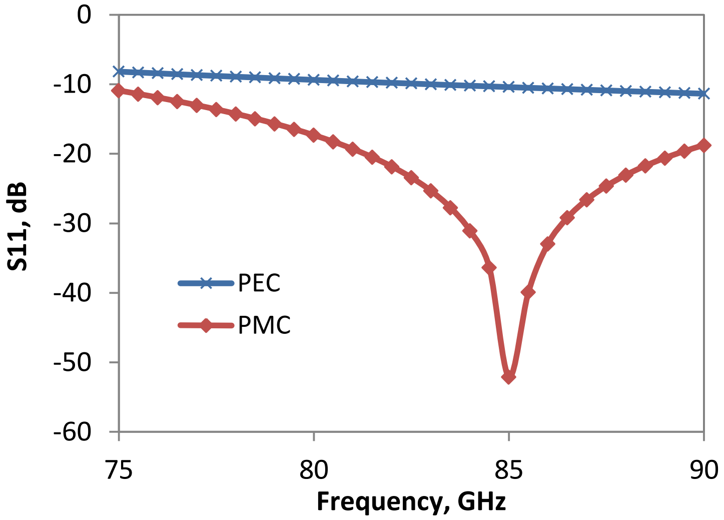

Fig. 37 Simulated S_{11}-parameters of the phase shifter with a PEC or PMC embedded in the waveguide bend.

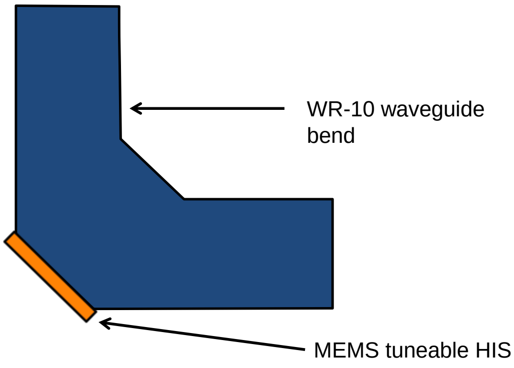

Fig. 38 Top view of the design of a transmission type phase shifter based on a rectangular metal waveguide bend with a MEMS tuneable HIS integrated in the corner of the bend ("cut" bend corner option).

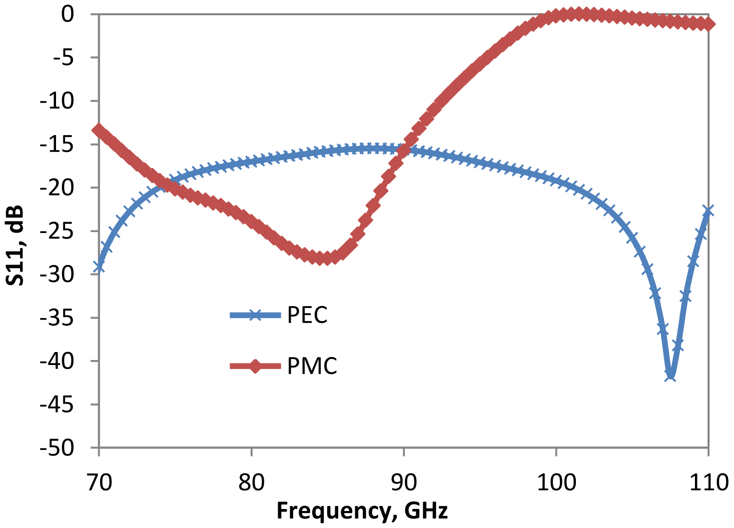

Fig. 39 Simulated S_{11}-parameters of the phase shifter with PEC or PMC embedded in the waveguide bend shown in Fig. 38.

3.2.1.3. Backshort integration

Integration of the MEMS tuneable HIS as a backshort of a rectangular metal waveguide, see Fig. 40, is the most efficient configuration of the metal waveguide phase shifter with a HIS in terms of losses. On the other hand, in this configuration the value of the maximum phase shift cannot be increased by choosing a larger structure as in case of the side wall integration (see Section 3.2.1.1). Here, for particular design dimensions of the HIS, the maximum achievable phase shift depends only on the tuneability of the MEMS varactors, which determines the change of the surface impedance. An example of the phase shifter tuning range is shown in Fig. 41 as a dependence of the reflection phase on the MEMS varactor gap for two realisation of the capacitance ratio. For the capacitance ratio equal to 1.5 (tuning range $\mathcal{A}$), the maximum analogue type phase shift is 163°, whereas for the capacitance ratio equal to 2.5 (tuning range $\mathcal{B}$), the maximum analogue type phase shift is 252°. A way to increase the tuning range of the MEMS varactors is discussed in Section 2.4.4. Also maximum achievable phase shift can be increased by decreasing the bandgap of the HIS by optimising its parameters as discussed in Section 2.2.

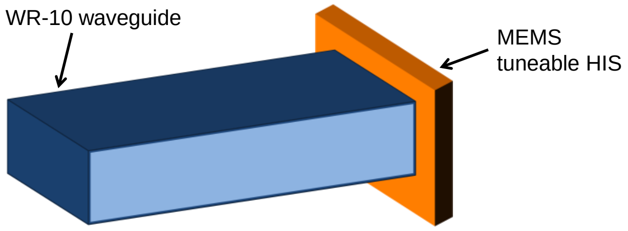

Fig. 40 Design of a reflection type phase shifter based on a rectangular metal waveguide with MEMS tuneable HIS integrated as a backshort of the waveguide.

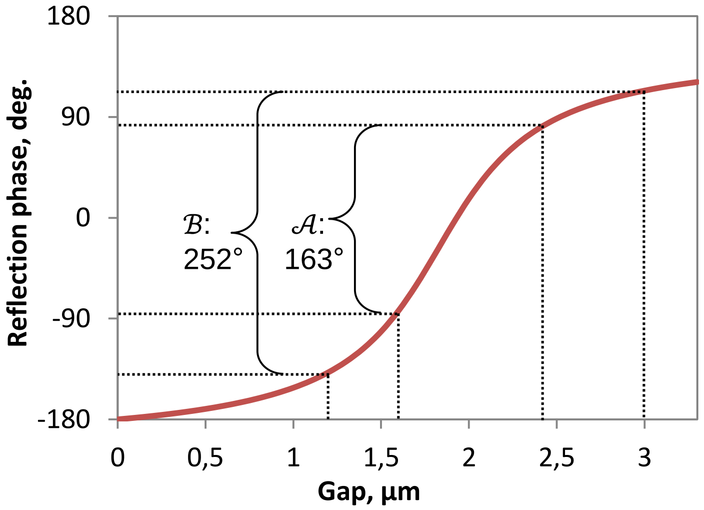

Fig. 41 An example of the reflection phase shift range for the MEMS capacitance ratio equal to 1.5 (range $\mathcal{A}$) and equal to 2.5 (range $\mathcal{B}$).

3.2.2. Measurement

As mentioned in Section 2.4.5, few rounds of fabrication of the MEMS tuneable HIS prototypes were carried out. Characterisation of all prototypes show distinctive behaviour of the structures as high-impedance surfaces: the reflection phase changes from almost 180° at lower frequencies to 0° at a resonance frequency, and back to almost -180° at higher frequencies. The resonance and out-of-resonance loss depends on the quality of the fabrication and integration of the prototypes and are respectively:

1) 5 dB and 2 dB [P2]
2) 18 dB and 7 dB [P4], [P5]
3) 3.5 dB and 0.7 dB [P6], see Fig. 42 (prototype image), and Fig. 43 (measured reflection phase and amplitude).

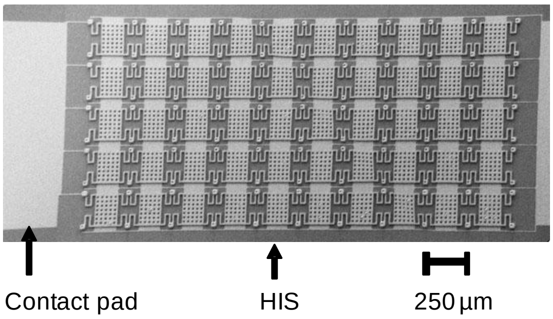

Fig. 42 SEM image of the fabricated MEMS-based HIS for a reflection type metal waveguide phase shifter [P6].

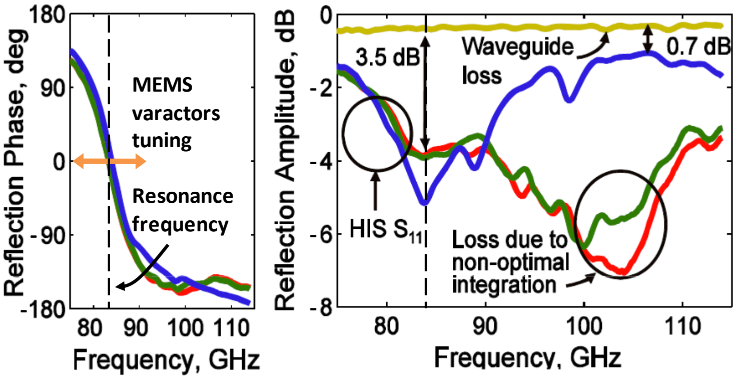

Fig. 43 Measured S_{11}-parameter of the reflection type phase shifter with a MEMS-based HIS as a backshort of the WR-10 waveguide over W-band. Reflection phase is 0° at the resonance frequency of 83.4 GHz. Minimum insertion loss of the HIS outside the resonance is 0.7 dB [P6].

Loss at resonance can be decreased by improving the fabrication procedure (choosing a better dielectric substrate, decreasing roughness of the metal surfaces, better removing of all chemical residuals). Out-of-resonance loss can be decreased by improving the integration of the HIS into the waveguide as discussed in [P7].

The actuation of the MEMS varactors of the prototype was not realised due to fabrication challenges. This – together with realisation of the better waveguide integration – is a subject of further development.

3.3. Analogue type phase shifter based on the MEMS tuneable HIS adjacent to a dielectric rod waveguide

3.3.1. Design and numerical analysis

Dielectric waveguides are promising transmission lines at millimetre wavelengths. It has been previously shown that a dielectric rod waveguide section with two transitions to a metal waveguide can have lower loss than a standard metal waveguide section, even at millimetre wavelengths [111]-

[113]. Being an open transmission line, dielectric waveguide can be affected by light, magnetic field, etc., allowing to design different types of devices, e.g., phase shifters. It is known, see, e.g., [110], that the propagation constant of a dielectric waveguide depends on the impedance of the adjacent ground plane.

The proposed analogue type phase shifter is based on the dielectric rod waveguide (DRW) with adjacent MEMS tuneable HIS, which changes the phase factor of the propagation constant inside the waveguide, see Fig. 44, [P8], [P9]. For W-band applications, Port 1 and Port 2 of the DRW should be matched to WR-10 rectangular metal waveguide sections. The optimal cross-section of the DRW for such matching is 0.5 × 1.0 mm^2 and tapering length is 6 mm [110].

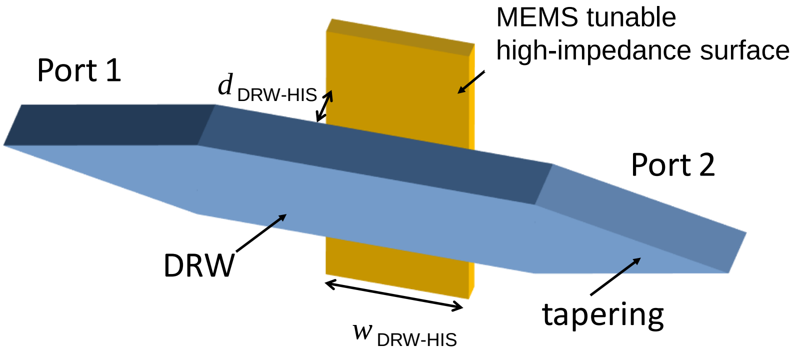

Fig. 44 Design of the analogue type phase shifter based on MEMS tuneable HIS placed adjacent to a dielectric rod waveguide.

Fig. 45 gives simulated values of the maximum possible phase shift of the phase shifter for an ideal case of tuning the impedance surface of length $w_{\text{DRW-HIS}}$ = 8 mm from PEC state to PMC state [P8]. The simulation shows high potential performance of such a phase shifter if MEMS tuneable HIS can be reconfigured from a very high to a very low impedance state.

The phase shift depends dramatically on the distance $d_{\text{DRW-HIS}}$ between the DRW and HIS, see Fig. 46, due to strong concentration of the electromagnetic field in close vicinity of the DRW [P8].

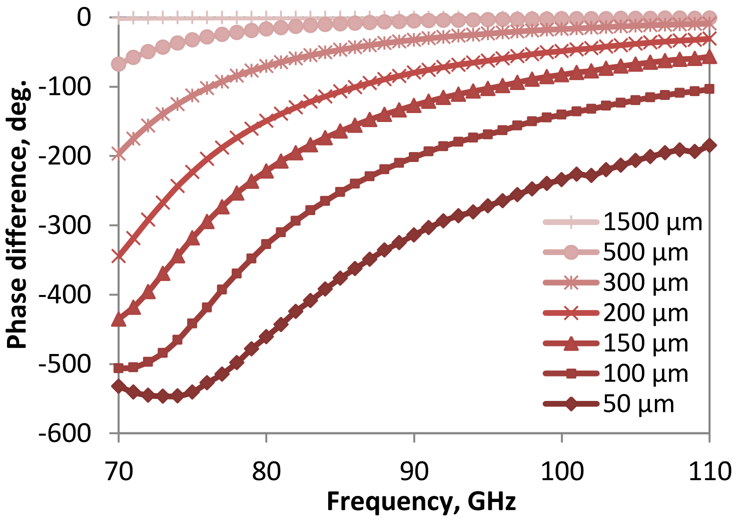

Fig. 45 Simulated phase shift of the DRW with an adjacent PMC (high-impedance surface at resonance) compared to an adjacent PEC (high-impedance surface out of resonance); for different distance $d_{DRW-HIS}$ between the DRW and HIS [P8].

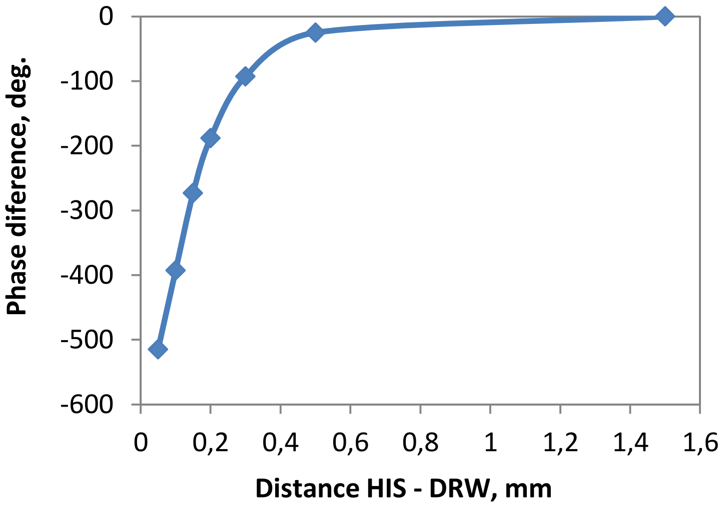

Fig. 46 Simulated dependence of the phase shift of the DRW with an adjacent tuneable HIS on the distance between the DRW and HIS at 80 GHz.

3.3.2. Fabrication and measurements

Two samples of the MEMS tuneable HIS with 120 × 24 MEMS varactors placed on a high resistivity silicon substrate with a period of 250 µm and a total size of 6 x 30 mm² were fabricated and measured [P9], see Fig. 46 and Fig. 47. The fabrication procedure is described in [P5] and [P6] and is the same as for the prototypes of the reflection type phase shifter, see Section 3.2. All varactors are connected by a bias voltage line to two contact pads, see Fig. 47. The tapering part (6 mm) of the DRW with cross-section 0.5 × 1.0 mm² made of high resistivity silicon is fixed with a foam holder (for Sample 1), see Fig. 48 (lhs), and Teflon film (for Sample 2), see Fig. 48 (rhs), the WR10 waveguides for measuring S-parameters.

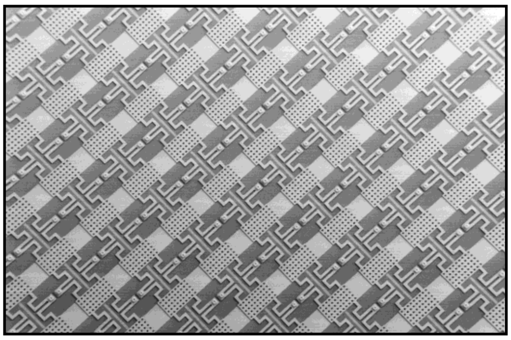

Fig. 47 SEM image of the fabricated MEMS tuneable HIS for an analogue type phase shifter based on a DRW; part of the large structure is shown [P9].

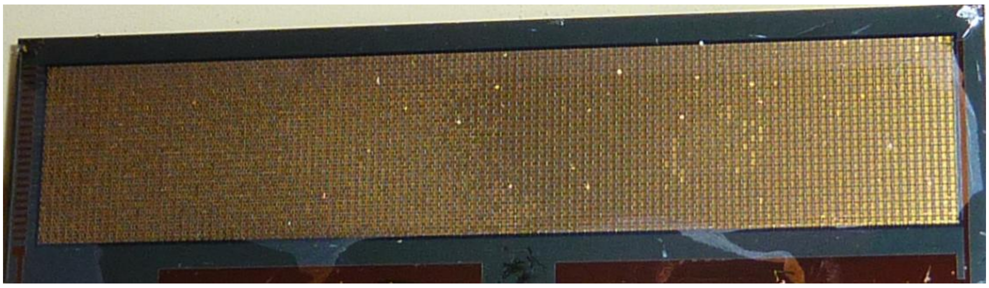

Fig. 48 Optical image of the fabricated MEMS tuneable HIS (Sample 2) for an analogue type phase shifter base on a DRW; two large contact pads common for all MEMS varactors are seen on the bottom edge of the image.

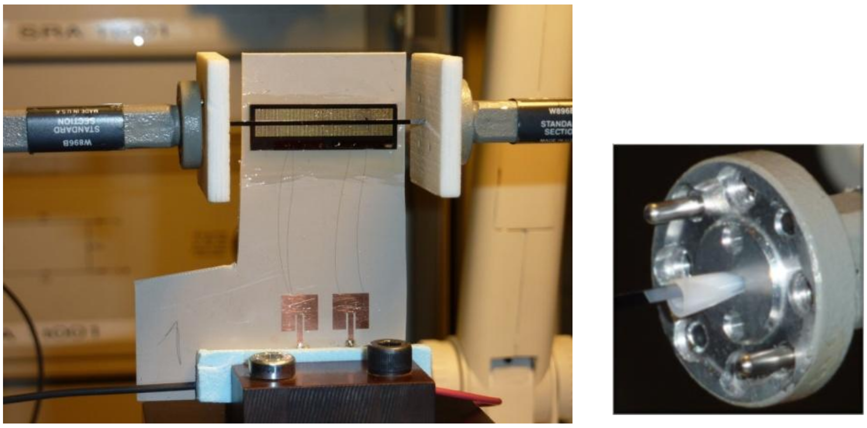

Fig. 49 Measurement setup: Sample 1 and DRW mounted with foam holders (lhs); mounting of the DRW with Teflon film for Sample 2 (rhs).

The S-parameters of the phase shifter are measured for both samples of the MEMS tuneable HIS, which are biased with a gradually changing voltage from 0 V to 40 V. The analogue type phase shift shown in Fig. 50 and Fig. 51 is a difference between S_{21} of the voltage biased phase shifter and S_{21} of the unbiased phase shifter, for Sample 1 and Sample 2, respectively.

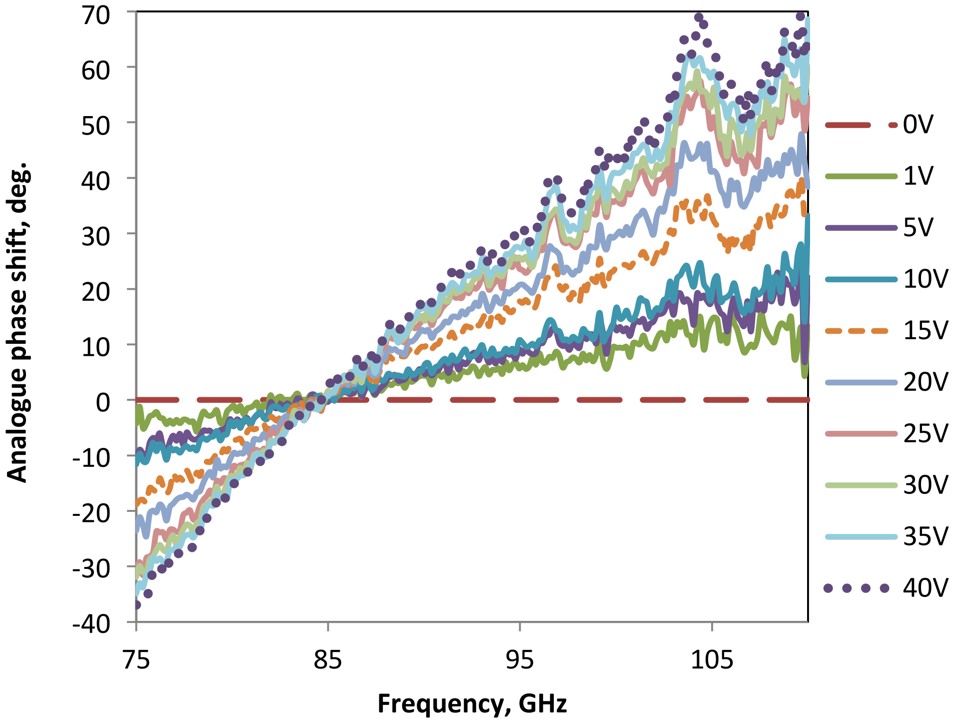

Fig. 50 Measured analogue type phase shift of the DRW with an adjacent MEMS tuneable HIS, Sample 1.

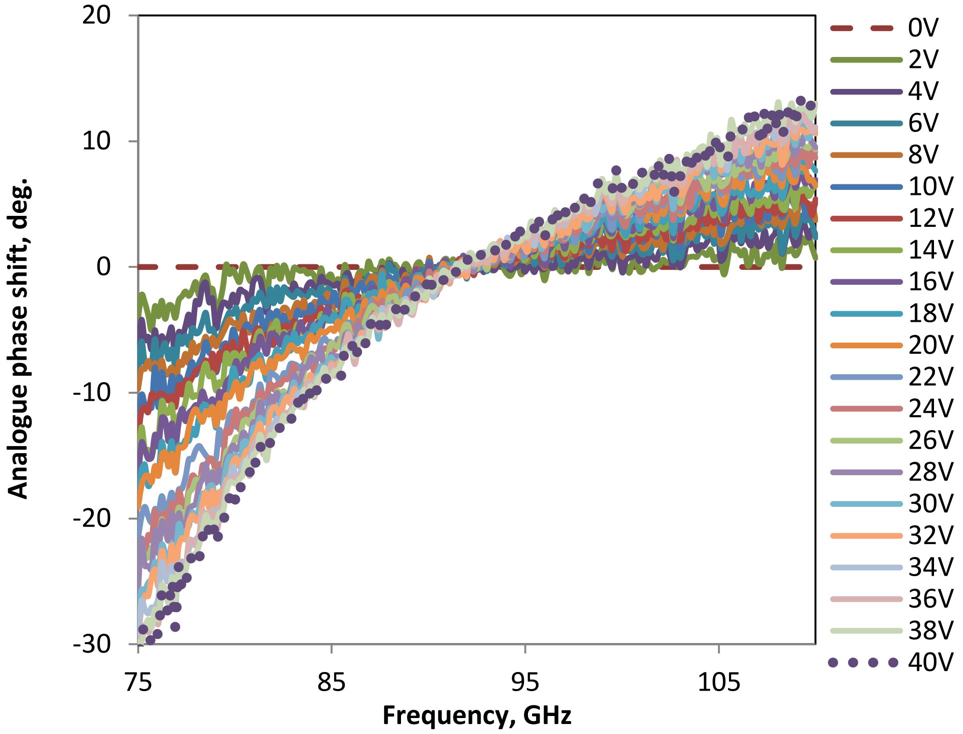

Fig. 51 Measured analogue type phase shift of the DRW with an adjacent MEMS tuneable HIS, Sample 2 [P9].

Fig. 52 shows dependence of the phase shift on the bias voltage for both samples at extreme frequencies of the measured range: 76 GHz and 109 GHz, where the phase shift turned out to be maximal. First thing to note is that the observed phase shift is purely of analogue type, which was one of the major objectives of the described research. Second, the fact that the phase shift has almost linear dependence on the bias voltage may mean that the effective impedance of the MEMS tuneable HIS changes only moderately and full range of MEMS varactors actuation is not achieved with the maximum bias voltage of 40 V. Larger phase shift values are anticipated for a larger impedance change. Third, the phase shift is 0° for intermediate frequencies of the measured frequency range, which allows expecting the phase shift to be much larger outside W-band.

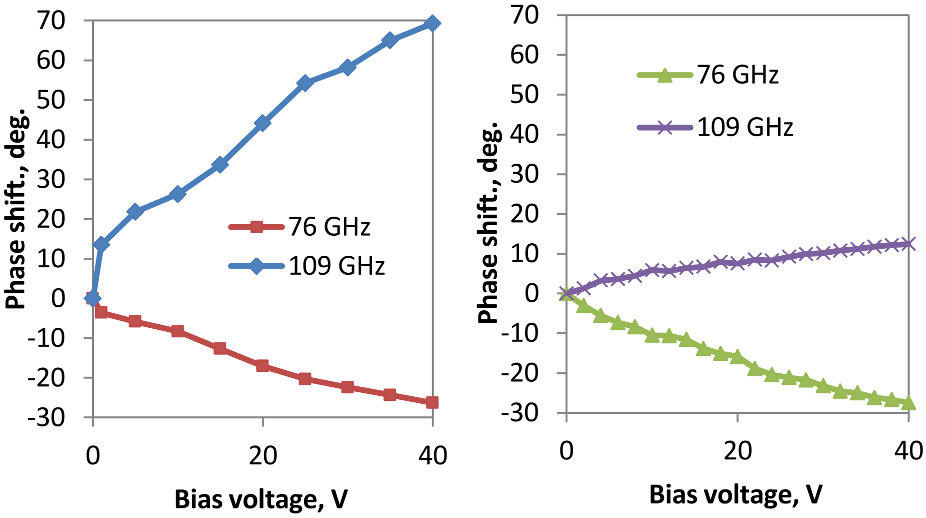

Fig. 52 Measured dependence of the phase shift on the bias voltage; Sample 1 (lhs) and Sample 2 (rhs) [P9].

The measured insertion loss of the phase shifter is shown in Fig. 53 for Sample 1 (lhs) and Sample 2 (rhs). The figure of merit of the phase shifter, defined as a ratio of the maximum phase shift to the maximum insertion loss, does not exceed value 5°/dB, which is small comparing to other existing millimetre wave phase shifters, see next section. The insertion loss of the phase shifter with Sample 2 of MEMS tuneable HIS is much smaller than the insertion loss of the phase shifter with Sample 1 due to both better matching of the DRW to the metal waveguide (Teflon film instead of the foam holder) and better quality of the fabricated sample. Measured with Teflon film, the phase shifter with Sample 1 would show figure of merit 10°/dB. The insertion loss of Sample 2 of the MEMS tuneable HIS is between 1.7 dB and 5 dB, which can be further decreased by optimizing the MEMS fabrication procedure. The insertion loss of the DRW matched to the rectangular metal waveguide is between 1.5 dB and 2 dB, which can be improved at W-band to be as low as 0.4 dB [112]. Thus, figure of merit can be improved both by increasing the phase shift and by decreasing the losses. As assessed in [P8], MEMS tuneable HIS can potentially achieve figure of merit up to 100°/dB in case of better MEMS fabrication quality, better DRW insertion loss including transition to the metal waveguide, and if the maximum tuneable range of the MEMS varactors is realised.

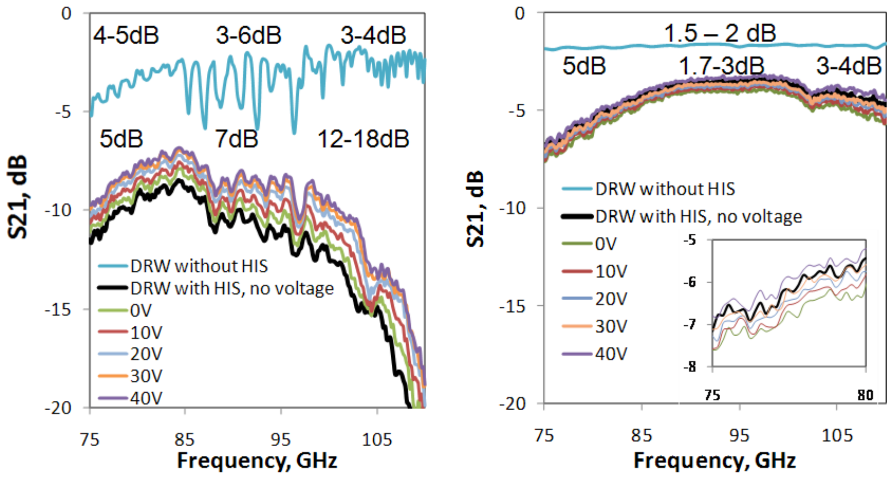

Fig. 53 Measured insertion loss of the phase shifter; Sample 1 (lhs) and Sample 2 (rhs) [P9].

3.3.3. State-of-the-art millimetre wave phase shifters

The next table gives an overview of existing millimetre wave phase shifters.

Frequency, GHz	Type	Design	Substrate	Loss, dB	Control voltage, V	Phase shift	Figure of merit	Year	Ref.
1-40	MEMS	switched line	GaAs	2-4	98	discrete, 4 bits	67°/dB @40GHz	2001	[114]
1-70	MEMS	distributed transmission line	quartz	3	19	analogue	55°/dB @40GHz, 74°/dB @60GHz	2003	[115]
26-30	PIN	switched filters	InGaAs	7	0.7	discrete, 5 bits	45°/dB	2011	[116]
30-36	PIN	switched filters	GaAs	7	17	discrete, 3 bits	25°/dB	1994	[117]
30-40	MEMS	distributed transmission line	quartz	2	20	discrete, 2 bits	112°/dB	2003	[118]
32-36	MEMS	switched line	Si	3	45	discrete, 4 bits	112°/dB	1999	[119]
33-36	FET	switched filters	GaAs	16.5	5	discrete, 4 bits	22°/dB	1998	[120]
33-36	PIN	switched line	-	10	-	discrete, 4 bits°	36°/dB	2004	[121]
34-39	CMOS	switched line	SiGe	2-9	1.8	quasi-analogue: 4 bit + analogue fifth bit	40°/dB	2009	[122]
40 (0-40)	paraelectric	distributed transmission line loaded with BST varactors	sapphire	9-28	40	analogue up to 600°	27°/dB	2007	[123]
40 (1-40)	MEMS	distributed transmission line	SiO2	1.8	16	analogue up to 290° @ 40 GHz	54°/dB	2006	[124]

Frequency, GHz	Type	Design	Substrate	Loss, dB	Control voltage, V	Phase shift	Figure of merit	Year	Ref.
43-45	FET	switched line	GaAs	7.5	2	discrete, 4 bits	48°/dB	1992	[125]
61-64	PIN	reflection	GaAs	11	2	discrete, 3 bits	39°/dB	1987	[126]
65-110	Liquid crystals	filled taper in rectangular metal waveguide	-	7	10	300-500° @ 65-110 GHz, only two states	60-78°/dB	2006	[127]
67-78	CMOS	switched line	SiGe	19	-	discrete, 4 bits	19°/dB	2009	[128]
75-110	varactor	reflection	GaAs	8,7	-	analogue	40°/dB	1993	[129]
75-110	MEMS	dielectric blocks over CPW	Si	3.5	30	discrete, 15°+30°+5x45°	70-100° /dB	2009	[130]
75-110	MEMS	distributed transmission line	glass	2.7	30	discrete, 3 bits	93-100°/dB	2004	[131]
75-110	MEMS	MEMS tuneable HIS adjacent to DRW	Si	5-7	40	analogue, up to 32° (70° with larger loss)	5°/dB	2011	[P9]
92-96	FET	loaded line	GaAs	11-15	1.5	discrete, 4 bits	24°/dB	1999	[132]
92-96	HEMT	switched line	GaAs	7	3	discrete, 4 bits	40-60°/dB	2007	[133]

3.4. Beam steering reflective surface with MEMS tuneable HIS

3.4.1. Introduction

Electronic beam steering based on a varactor-tuned HIS for microwave frequencies was proposed by Sievenpiper in 2001 and improved in 2003 [73], [134]. Varactor diodes were connected between each two neighbouring metal patches of the patch array of the surface. Applying bias voltage to the varactors changed the effective capacitance of the surface and consequently effective input impedance. A gradient of the reflection phase could be created by adjusting bias voltages so that a gradient of effective surface impedance was generated throughout the surface. As a result, the beam incident to the tuneable impedance surface could be electrically steered by applying different bias voltage combinations. Beam steering of ±40° was reported with 14 dB gain and total efficiency 30 % at non-steered (mirror reflection) state. According to the authors' conclusions, several dB loss was due to utilisation of relatively lossy MicroMetrics silicon hyperabrupt varactors and phase errors caused by non-optimised voltage control.

Similarly, MEMS tuneable varactors can be used for controlling the surface impedance of the HIS in order to achieve electronic beam steering. As the MEMS varactors of the HIS are connected in rows, as described above, the applied bias voltage can be different for each row and we can create a gradient of the effective surface impedance of the structure, resulting in a gradient of the reflection phase throughout the HIS. Changing the gradient we obtain electronic beam steering of the reflected beam, see Fig. 54.

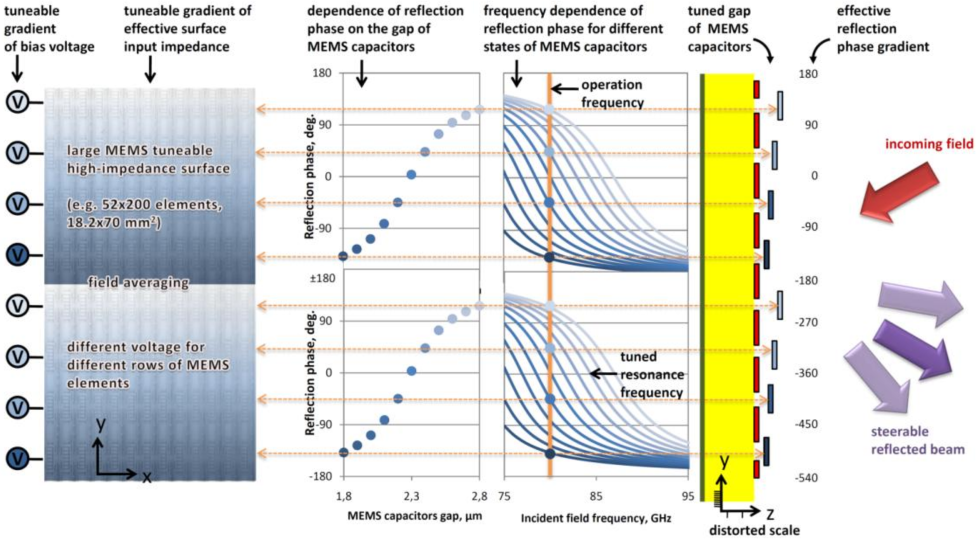

Fig. 54 MEMS-based HIS with induced tuneable gradient of the effective surface impedance for electric beam steering.

Thanks to the electrically small period of the HIS (small size of MEMS varactors) achievable by MEMS fabrication, we can implement sawtooth grating of the reflection phase, see Fig. 55. The bias voltage is applied to the MEMS varactors so that several sections with maximal (in an ideal case close to 360°) phase gradient appear. Due to 360° periodicity, the phase gradient will multiply the overall effective phase difference throughout the surface and dramatically increase steering angle.

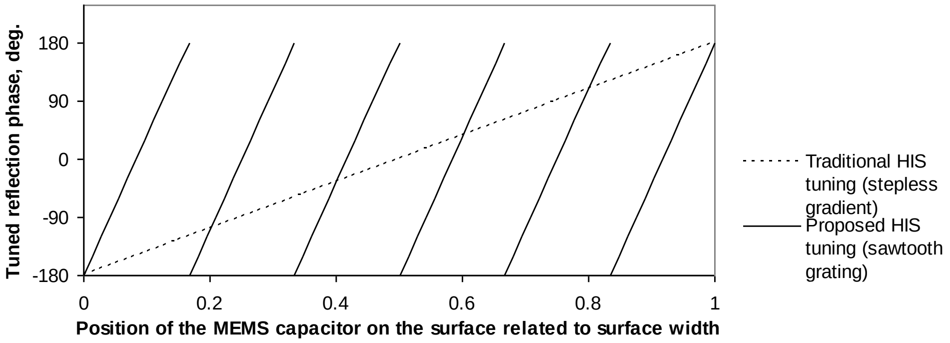

Fig. 55 Schematic representation of the alternative ways of HIS tuning: Traditional (dotted line) - stepless gradient of the reflection phase with maximum phase difference on the opposite edges; Proposed (solid lines) sawtooth gradient of the reflection phase for larger steering angle.

Implementation of MEMS fabrication technology for enabling tuneability of a HIS as a reflective beam steering surface allows achieving the following advances:

- Development of small beam steering reflective surface operating at millimetre wavelengths due to miniaturising abilities of MEMS technology;
- Reduction of system complexity due to replacement of, e.g., a phased array antenna by a single smart surface fabricated on a chip;
- Increased radiation efficiency due to the low loss intrinsic to MEMS devices,
- Improved radiation pattern due to more accurate voltage control enabled by electrically smaller period of the structure;
- Increased tuning angle of the steered beam due to electrically small period of the structure, which allows accurate inducing of large gradient of the reflection phase;
- Cost-effectiveness due to reduced cost of system integration (low system complexity) and batch manufacturing with MEMS technology.

Since the MEMS varactors are connected to the bias voltage in rows, the reflected beam can be steered in one dimension only. If steering in the second dimension is required, it can be realised by a complex bias voltage network, which allows controlling each MEMS varactor independently. Alternatively, a folded reflectarray structure as in [135] can be used for controlling the direction of the beam in the second dimension.

3.4.2. Numerical analysis

Derived analytical model for the MEMS tuneable HIS is given in Section 2.4.4 and is valid also for calculating impedance and reflection coefficient of a large beam steering HIS. On the other hand, it is important to study the radiation pattern of the reflective MEMS tuneable HIS especially because of inherent feature of the MEMS varactors' limited tuneability, see Section 2.4.3. This feature limits the available range of the HIS reflection phase to, e.g., -102°... 120°. Consequently, if a phase gradient, calculated for a particular angle of beam steering requires some section of the HIS to reflect the incident wave with a phase within ranges -180°...-102° and 120°...180°, this should be replaced by -102° or 120°, respectively. This creates discontinuities in the programmed phase gradient and can affect the radiation pattern of the reflected steered beam. On the other hand, since the period of the structure is much smaller than the wavelength, the effect of the limited tuning range may be minor thanks to averaging of the electromagnetic field above HIS.

Numerical simulation of the exact model of the reflective MEMS tuneable HIS radiation pattern is practically impossible since it contains hundreds of unit cells. That is why an approximate model consisting of variable impedance strips, see Fig. 56, is used to study the radiation pattern of a reflective impedance surface [P10]. Impedance boundary conditions are applied separately for each 350 μm wide strip according to calculations of the required phase distribution for particular reflective beam steering angles. Fig. 57 shows the normalised radiation pattern of the wave reflected from the variable impedance surface for 45° oblique incidence and calculated steering angle of 0° (i.e. 45° degree beam steering). Numerical simulations are given both for limited reflection phase tuning range and full tuning range, and show no advantage of the full tuning range. On the other hand, increasing number of the strips (and consequently the width of the structure), expectedly narrows the beamwidth and decreases the backward reflections, see Fig. 9 in [P10]. As we can see in Fig. 57, the steering angle of the main beam agrees very well with the programmed value of 0°, although the side lobes, especially in the backward and mirror reflection directions, still need to be optimised. Similar results are obtained for other incidence and steering angles [P10].

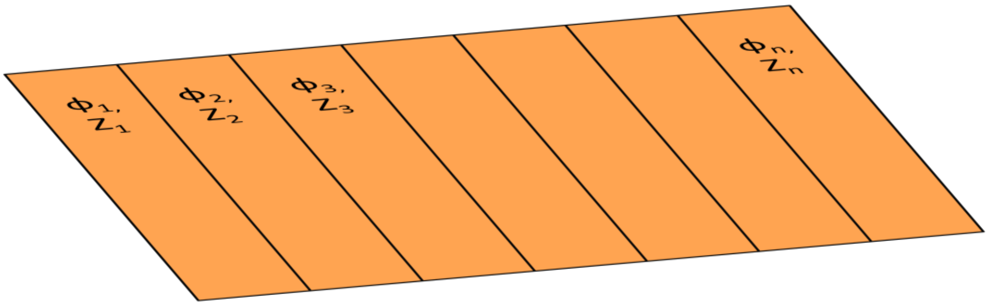

Fig. 56 Simplified model of the variable impedance surface for simulation of the radiation pattern.

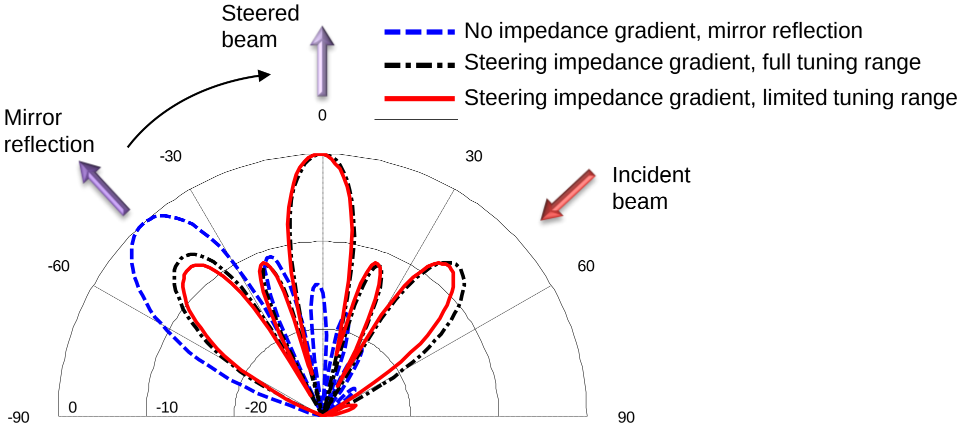

Fig. 57 Normalised radiation pattern of the surface with tuneable impedance gradient at 80 GHz, which is programmed for reflecting a beam incident from 45° to 0°. Mirror reflection pattern is shown for reference [P10].

3.4.3. Prototyping

The minimum aperture of the steering device (phased array antenna, reflective beam steering surface) can be estimated from the requirement for the angular resolution of the long range radar to be better than 5°, which is determined by the beamwidth of the main lobe. The minimum aperture in the steering direction for 5° angular resolution, in case of matched polarisations, is (for 77 GHz):

$$Aperture = \frac{wavelength}{beamwidth} = \frac{3.9\ mm}{5° \cdot \, 2\pi/_{360°}} = 44.7\ mm.$$

Since the MEMS tuneable HIS steer the beam in oblique directions, the width of the HIS is chosen to be 70 mm or 200 unit cells of 350 µm. The width of the HIS in the direction perpendicular to the steering plane was chosen to 18.2 mm or 52 unit cells, because for the target application (automotive radar) the beam width requirements in this plane are less demanding.

SEM images and an optical image of a large fabricated prototype of MEMS-based HIS with 200 × 52 MEMS capacitors is shown in Fig. 58 and Fig. 59, respectively. Due to fabrication challenges related to the reliable performance of such a large array of MEMS varactors, tunability of the prototype is not yet realised. Nevertheless, the results of previously described analytical and numerical analyses as well as measurement results of MEMS tuneable HIS allow arriving to a conclusion about potential usability of the MEMS tuneable HIS for direct beam steering application on a single chip device.

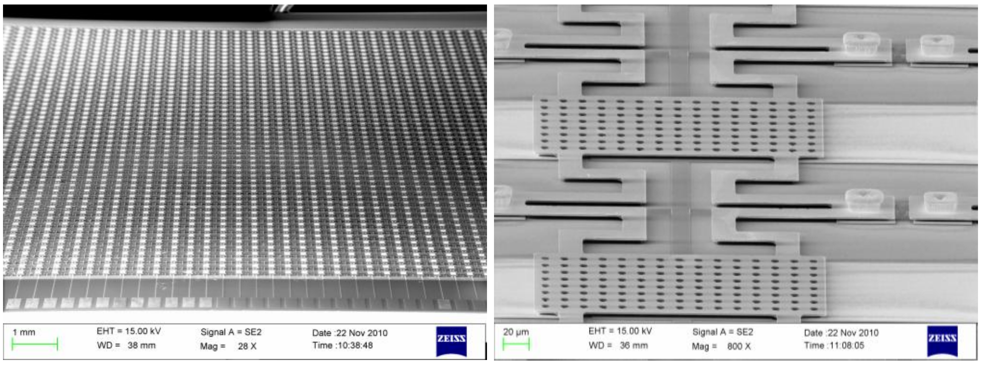

Fig. 58 SEM images of the fabricated MEMS-based HIS prototype.

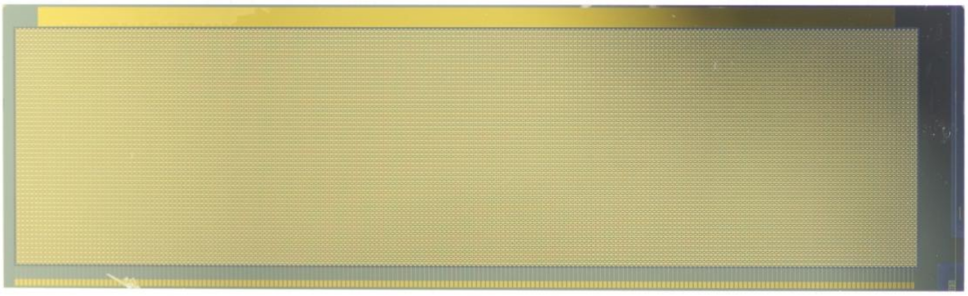

Fig. 59 Optical image of the fabricated MEMS-based HIS prototype.

3.5. Conclusion

In this chapter MEMS tuneable HIS is studied as a phase shifting and beam steering device for millimetre wave applications.

Section 3.2 shows different possibilities of embedding HIS inside a rectangular metal waveguide in order to control the phase of the wave propagated inside the waveguide. The HIS can be introduced in the narrow walls of a rectangular metal waveguide, in the corner of a waveguide bend for a transmission type phase shifter, and as a backshort of a waveguide for a reflecting type phase shifter. Both analytical analysis and numerical results show possibility of analogue type phase shift. Measurement results of the MEMS-based HIS prototype proved a resonant behaviour of the structure with very high impedance at the resonance frequency 83 GHz. The reflection phase changes smoothly from almost 180° at lower limit of the measured W-band to 0° at the resonance, and to -180° at the higher limit of the W-band. Minimum insertion loss of the HIS outside of the resonance is 0.7 dB and at the resonance it is 3.5 dB. The insertion loss value can be further improved by optimising the fabrication procedure and integration of the HIS inside the waveguide.

Section 3.3 describes an analogue type phase shifter based on the MEMS tuneable HIS adjacent to a dielectric rod waveguide. Numerical simulations show that potential analogue type phase shift can cover full 360° for relatively small size of the HIS. The value of the phase shift depends dramatically on the distance between the waveguide and the HIS since the propagating field is strongly concentrated inside and in vicinity of the waveguide. Appropriate distance for the studied case would be around 100 μm. A MEMS tuneable HIS with 120 × 24 varactors with period of 250 μm was fabricated on a high resistivity silicon substrate. Analogue type phase shift of up to 70° is measured when the bias voltage of the MEMS tuneable HIS adjacent to the dielectric rod waveguide is changed from 0 V to 40 V.

Section 3.4 studies feasibility of the single chip beam steering device based on inducing reconfigurable gradient of the reflection phase throughout the MEMS tuneable HIS. Simulated radiation pattern of a simplified model of the reconfigurable impedance surface shows a possibility of steering the direction of the reflected beam by inducing impedance throughout the structure with periodicity much smaller than the wavelength. Limitations of MEMS technology on the impedance tuneability do not affect the radiation pattern.

4. Summary of the publications

Paper [P1]: MEMS fabrication technology is proposed for enabling tuneability of a high-impedance surface (HIS). The tuneable multilayer HIS consists of electrically small MEMS varactors coupled to each other and placed on a dielectric substrate with a ground plane. The MEMS tuneable HIS is proposed for developing an analogue type millimetre wave low loss phase shifter based on a rectangular metal waveguide. A prototype of a multilayer HIS with a thin film filling the capacitors' gap is designed, microfabricated and measured as a back-short of a WR-10 waveguide proving resonance behaviour of the structure. The simulation and measurement results of S11-parameter show good agreement.

Paper [P2]: Dependence of the multilayer HIS behaviour on the electromagnetic properties of the material, which fills the gap of the capacitors is analysed numerically. The maximum loss tangent value of the material, which allows reflection phase transition from 180° to 0° and -180° is found. A multilayer MEMS-based HIS with air filling the capacitors' gap is designed, analysed, manufactured and measured. Analysis of the reflection phase dependence of the MEMS varactor's gap shows the range of the analogue tuneability of the reflection phase. Results of the S11-parameter measurements prove the high-impedance behaviour of the structure and show agreement with the simulation results.

Paper [P3]: An analytical model of the multilayer HIS is proposed. Equivalent circuit and effective resonant circuit parameters are introduced for simplification of the HIS design and analysis of the dependence of the materials' electromagnetic properties on the performance of the HIS. Analytical and numerical analysis of the multilayer HIS performance with different values of loss tangent of the dielectric is carried out. Analytical, numerical and measurement results show good agreement.

Paper [P4]: An improved MEMS-based HIS design with supporting springs and triple-layer membrane of the MEMS capacitors is introduced for lower actuation voltage, near-ideal flatness and high mechanical robustness. The improved MEMS-based HIS is designed, analysed numerically, fabricated and measured. Electronic beam steering using the MEMS tuneable HIS is proposed.

Paper [P5]: A novel fabrication procedure for realising analogue tuneable MEMS varactors to be used in HIS is proposed and carried out. MEMS varactor's membrane deflection is simulated and measured, showing good agreement and low actuation voltage.

Paper [P6]: A MEMS-based HIS is designed for analogue type phase shifter based on a rectangular metal waveguide. Analytical and numerical analysis of the phase shift of the waveguide with embedded tuneable HIS in the waveguide's sidewalls is carried out. Good agreement between analytical and simulation results is found. Insertion loss of the MEMS-based HIS is dramatically decreased by improved fabrication procedure and usage of the high resistivity silicon as a dielectric substrate of the HIS. Reliability and repeatability study of the MEMS varactor is performed including measurement of the membrane deflection over 100 million actuation cycles showing virtually no degradation. Measurement of the membrane curvature shows invariance over actuated membrane deflection. The varactor's gap changes in an analogue way with the applied actuation voltage.

Paper [P7]: A novel method of integrating MEMS chips into rectangular metal waveguides is proposed and demonstrated for decreasing the insertion loss and integration of the bias voltage lines for controlling the MEMS chip. Measurement results of a conventional interface with increasing air gaps between the waveguide and a reflective metal surface show strong insertion loss even with very small air gap. The proposed interface performs as good as, or better than direct metal contact. Narrow side wall openings for bias lines do not affect the performance of the interface.

Paper [P8]: An analogue type phase shifter based on a dielectric rod waveguide with an adjacent MEMS tuneable HIS is proposed. The phase shifting and loss performance is assessed by numerical simulations of magnetic and electric walls adjacent to the dielectric rod waveguide in order to bypass computational complexity and mimic tuneability of HIS. A large prototype of the MEMS-based HIS is fabricated and the proposed device is characterised. Both numerical and measurement results show promising phase shift performance once a tuneable HIS is realised.

Paper [P9]: A new prototype of the MEMS-based HIS placed adjacent to a dielectric rod waveguide shows an analogue type phase shift with bias voltage applied to the MEMS varactors. A novel design of the MEMS varactors for increased tuneability range is introduced.

Paper [P10]: Beam steering with a MEMS-based HIS is studied in W-band. The radiation pattern of a surface with different impedance is analysed numerically for normal and oblique incidence. The steering range is achieved from -45° to 45° with respect to the normal direction.

5. Conclusions and future work

This work studies novel MEMS tuneable HIS for millimetre wave phase shifting and beam steering applications. The MEMS tuneable HIS consists of a two-dimensional periodic arrangement of coupled MEMS varactors placed on a grounded dielectric substrate with a period much smaller than the wavelength of the electromagnetic field interacting with the structure. MEMS fabrication technology is proposed for enabling tuneability of the HIS because of its advantage over conventional components in term of losses at millimetre wave frequency. An analytical model of the multilayer and MEMS tuneable HIS is elaborated taking into account dielectric losses and their effect on the performance of the HIS. Different models of millimetre wave analogue type phase shifters with a MEMS tuneable HIS embedded in the waveguiding structures are proposed and studied both analytically and numerically showing a large potential phase shift. Tuneability of the MEMS varactors and its influence to the phase shift and beam steering are studied, and an advanced design of the MEMS varactors for increased tuneability is proposed. Several prototypes of the MEMS tuneable HIS are fabricated and characterised. The life-cycle measurement of the MEMS varactor's membrane deflection over 100 million actuation cycles shows virtually no degradation. The membrane deflects in an analogue wave with applied bias voltage. Measurements of the prototypes as a backshort of the rectangular metal waveguide correspond to analytical and numerical results and show clear resonance behaviour of the HIS with reflection phase transition from 180° to 0° at the resonance and to -180°. Measurements of the S_{21}-parameter of a silicon dielectric rod waveguide with an adjacent MEMS tuneable HIS controlled by a bias voltage demonstrate analogue type phase shift of up to 70°.

Further work can continue in two directions. The first direction is to improve insertion loss of the MEMS-based HIS. This can be attained by combining following improvement factors: choice of better fabrication material, optimisation fabrication procedure, and development of better integration methods of the HIS to the waveguides. The second direction is development of the fabrication procedure for reliable actuation of the large array of MEMS varactors, which is challenging because even small modulation of the dimension or electromechanical properties in the hundreds of varactors decrease or even prevent tuneability of the whole structure. Despite of these challenges the work shows potential of implementation of the MEMS tuneable HIS for millimetre wave phase shifting and beam steering application especially in industrial fabrication environment.

References

[1] D. Chicherin, S. Tretyakov, and A.V. Räisänen, “Reconfigurable high-impedance surfaces using MEMS capacitors for multi-octave tunability and beam steering,” *Proc. of Third Annual SMARAD Centre of Excellence Research Seminar, Helsinki University of Technology Radio Laboratory Publications, Report S270*, April 8, 2005, pp. 19-22.

[2] D. Chicherin, S. Dudorov, D. Lioubtchenko, V. Ovchinnikov, S. Tretyakov, and A.V. Räisänen, “Reconfigurable MEMS-Based high-impedance surfaces for millimetre and submillimetre wave phase shifters,” *Proc. of the 4th ESA Workshop on Millimetre Wave Technology and Applications/TSMMW2006/MINT-MIS2006*, Espoo, Finland, February 15-17, 2006, pp. 515-520.

[3] D. Chicherin, S. Dudorov, D. Lioubtchenko, V. Ovchinnikov, S. Tretyakov, and A.V. Räisänen, “MEMS-based high-impedance surfaces for millimetre and submillimetre wave applications,” *Third Workshop on Metamaterials and Special Materials for Electromagnetic Applications and TLC*, Rome, March 30-31, 2006.

[4] D. Lioubtchenko, D. Chicherin, S. Dudorov, V. Ovchinnikov, J. Mallat, and A.V. Räisänen “Passive and active devices based on dielectric rod waveguides for millimetre wavelengths,” *Proc. of the 4th Microwave Materials And Their Applications Conf.,* Oulu, June 12-15, 2006, p. 104.

[5] I.S. Nefedov, D. Chicherin, and A.J. Viitanen, “Infrared cloaking based on wire media,” *Proc. of SPIE Conf. Photonics Europe 2008,* April 7-11, 2008, vol. 6987, pp. 698728-698728-8.

[6] A.V. Räisänen, J. Ala-Laurinaho, D. Chicherin, S. Dudorov, A. Karttunen, D. Lioubtchenko, O. Luukkonen, J. Mallat, P. Pousi, A. Tamminen, and M. Vaaja, “Mm- and submm-wave research activities at MilliLab and SMARAD,” *Proc. of the Global Symp. on Millimeter Waves 2008*, 21-24 April 2008, Nanjing, China, pp. 136-137.

[7] D. Chicherin, S. Dudorov, M. Sterner, J. Oberhammer, and A.V. Räisänen, “Rectangular metal waveguide phase shifter controlled with MEMS high-impedance surface,” *Proc. of XXXI Finnish URSI Convention on Radio Science Electromagnetics 2008*, October 28, 2008, Espoo, Finland, pp. 27-28.

[8] D. Chicherin, M. Sterner, Z. Baghchehsaraei, J. Oberhammer, S. Dudorov, Z. Du, T. Zvolensky, A. Vorobyov, M. de Miguel Gago, E. Fourn, R. Sauleau, T. Labia, G. El Haj Shhade, F. Bodereau, P. Mallejac, J. Åberg, C. Simovski, A.V. Räisänen, "MEMS tunable metamaterials for beam steering millimeter wave applications," *Proc. of NATO Research Workshop on Advanced materials and technologies for micro/nano-devices, sensors and actuators: From fundamentals to applications,* June 29 - July 2, 2009, St. Petersburg, Russia, p.45.

[9] M. Sterner, D. Chicherin, A.V. Räisänen, G. Stemme, and J. Oberhammer, "RF MEMS high-impedance tuneable metamaterials for millimeter-wave beam steering," *Proc. of GigaHertz Symp.,* March 9-10, 2010, Lund, Sweden.

[10] T. Zvolensky, D. Chicherin, A. Räisänen, C. Simovski, "Beam-steering MEMS-loaded antenna based on planar lines," *Proc. of 4th European Conf. on Antenna and propagation*, April 12-16, 2010, Barcelona, Spain.

[11] M. Sterner, D. Chicherin, A.V. Räisänen, G. Stemme, and J. Oberhammer, "RF MEMS tuneable high-impedance metamaterial surfaces for millimeterwave applications," *Micro Structure Workshop 2010*, Stockholm, Sweden, May 4-5, 2010.

[12] T. Zvolensky, D. Chicherin, A. Räisänen, and C. Simovski, "Leaky-wave regimes on MEMS-loaded transmission lines for mm-wave applications," *Progress in Electromagnetics Research M*, vol. 13, pp. 157-171, 2010.

[13] M. Sterner, D. Chicherin, A.V. Räisänen, G. Stemme, and J. Oberhammer, "Reliability investigation of stress-compensated metal-coated monocrystalline-silicon membranes for MEMS tuneable high-impedance surfaces," *MEMSWAVE Conf. 2010,* June 28-30, 2010, Otranto, Italy, MEMS_S3_2_msterner.pdf.

[14] D. Chicherin, M. Sterner, J. Oberhammer, S. Dudorov, D. Lioubtchenko, V. Ovchinnikov, and A.V. Räisänen, "MEMS tunable metamaterials surfaces and their applications," *Asia Pacific Microwave Conference 2010,* Yokohama, Japan, December 7-10, 2010, pp. 239-242, invited.

[15] T. Zvolensky, D. Chicherin, A.V. Räisänen, and C. Simovski, “Leaky-wave antenna based on MEMS-loaded microstrip line,” *IET Microwaves, Antennas and Propagation*, vol. 5, no. 3, pp.357-363, 2011.

[16] Z. Du, D. Chicherin, and A.V. Räisänen, “MEMS-based high impedance surface for beam steering at 80 GHz,” *Proc. of Global Symp. on Millimeter Waves 2011*, Espoo, Finland, May 23-25, 2011.

[17] T. Zvolensky, M. Sterner, D. Chicherin, H. Hakojärvi, J. Oberhammer, C. Simovski, and A.V. Räisänen, “Leaky-wave antenna at 77 GHz,” *Proc. of European Microwave Conf. 2011*, Manchester, UK, October 9-14, 2011.

[18] M. Sterner, N. Somjit, U. Shah, S. Dudorov, D. Chicherin, A.V. Räisänen, and J. Oberhammer, “Microwave MEMS devices designed for process robustness and operational reliability,” *International Journal of Microwave and Wireless Technologies,* , vol. 3, no. 5, pp. 547-563.

[19] D.V. Lioubtchenko, V. Ovchinnikov, D. Chicherin, and A.V. Räisänen, “Millimeter wave phase shifters based on dielectric rod waveguide”, *IEEE Conf. on Electromagnetics in Advanced Applications and IEEE-APS Topical Conf. on Antennas and Propagation in Wireless Communications (ICEAA - IEEE APWC 2011)*, September 12-17, 2011, Torino, Italy.

[20] A. Vorobyov, R. Sauleau, E. Fourn, D. Chicherin, A. Räisänen, J. Oberhammer, and Z. Baghchehsaraei, “Iris-Based 2-bit waveguide phase shifters and transmit-array for automotive radar applications,” *European Conf. on Antenna and Propagation 2012*, submitted.

[21] Decision no. 676/2002/EC of the European Parliament and of the European Council of 7 March 2002 on a regulatory framework for radio spectrum policy in the European Community (Radio Spectrum Decision), available at http://eur-lex.europa.eu/LexUriServ/LexUriServ.do?uri=OJ:L:2002:229:0015:0023:EN:PDF, read March 10, 2011.

[22] European Commission Decision no. 2004/545/EC of 8 July 2004 on the harmonisation of radio spectrum in the 79 GHz range for the use of automotive short-range radar equipment in the Community, available at http://eur-lex.europa.eu/LexUriServ/LexUriServ.do?uri=OJ:L:2004:241:0066:0067:EN:PDF, read March 10, 2011.

[23] European Commission Decision no. 2005/50/EC of 17 January 2005 on the harmonisation of the 24 GHz range radio spectrum band for the time-limited use by automotive short-range radar equipment in the Community, available at http://eur-lex.europa.eu/LexUriServ/LexUriServ.do?uri=OJ:L:2005:021:0015:0020:EN:PDF, read March 10, 2011.

[24] European Commission public consultation of 14 December 2010, Short range radars in vehicles for road safety, call to stakeholders for their views on the proposed amendment to commission decision 2005/050/EC, available at http://ec.europa.eu/information_society/policy/ecomm/radio_spectrum/_document_storage/consultations/2010_srr/srr_public_consultation.pdf, read March 10, 2011.

[25] TRW Automotive / Autocruise S.A., automotive radar AC-20 specifications, http://www.adaptive-cruise-control.com/medias/5/1172588419.pdf, read March 10, 2011.

[26] Volkswagen Phaeton price list, available at http://cdn.volkswagen.co.uk/assets/common/pdf/pricelists/phaeton-gp-iii-pricelist.pdf, read March 10, 2011.

[27] H. Kirino and K. Ogawa, "A 76 GHz phased array antenna using a waffle-iron ridge waveguide," *European Conf. Antennas Propagation*, *EUCAP2010*, Barcelona, Spain, April 2010, p. C32P2-2.

[28] W. Menzel, "Millimeter-wave radar for civil applications," *European Radar Conf.*, Paris, France, September 2010, pp. 261-264.

[29] P.S. Hall and S.J. Vetterlein, "Review of radio frequency beamforming techniques for scanned and multiple beam antennas," *IEE Proc. H. on Microwaves, Antennas, and Propagation*, vol. 137, no. 5, pp. 293-303, October 1990.

[30] P. Chen, Z. Kuai, J. Xu, H. Wang, J. Chen, H. Tang, J. Zhou, and K. Wu, "A multibeam antenna based on substrate integrated waveguide technology for MIMO wireless communications," *IEEE Trans. Antennas Propagation*, vol. 57, no. 6, pp. 1813-1821, June 2009.

[31] Y.-J. Chen, W. Hong, F. Wu, Z.-Q. Kuai, C. Yu, J.-X. Chan, J.-Y. Zhou, H.-J. Tang, “Substrate integrated waveguide (SIW) Rotman lens and its Ka-band multibeam array antenna applications,” *IEEE Trans. Antennas Propagation*, vol. 56, no. 8, pp. 2504-2513, August 2008.

[32] Y.-J. Chen and K. Wu, “Millimeter wave substrate integrated waveguide multibeam antenna based on the parabolic reflector principle,” *IEEE Trans. Antennas Propagation*, vol. 56, no. 9, pp. 3055-3957, September 2008.

[33] M. Ettorre, A. Neto, G. Gerini, and S. Maci, “Leaky-wave slot array fed by a dual reflector system,” *IEEE Trans. Antennas Propagation*, vol. 56, no. 10, pp. 3143-3149, October 2009.

[34] R.C. Hansen, *Phased Array Antennas*, John Wiley and Sons, Inc., New-York, 1998.

[35] D. Teeter, R. Wohlert, B. Cole, G. Jackson, E. Tong, P. Saledas, M. Adlerstein, M. Schindler, and S. Shanfield, “Ka-band GaAs HBT PIN diode switches and phase shifters,” *IEEE Microwave and Millimeter-Wave Monolithic Circuits Symp. Digest,* 1994, pp. 183-186.

[36] J. Putnam, M. Barter, K. Wood, and J. LeBlanc, “A monolithic GaAs PIN switch network for a 77 GHz automotive collision warning radar,” *IEEE MTT-S International Microwave Symp. Digest,* 1997, pp. 753-756.

[37] D.K. Ghodgaonkar, R. Hughes, F. Selmi, V.V. Varadan, and V.K. Varadan, “Ferroelectric phase shifters for electronically steerable antenna systems,” *IEEE Antennas and Propagation Society International Symp. Digest*, 1992, pp. 272-275.

[38] S. Tretyakov, *Analytical Modeling in Applied Electromagnetics*, Artech House, Boston, 2003.

[39] C. Caloz and T. Itoh, *Electromagnetic Metamaterials: Transmission Line Theory and Microwave Applications, the Engineering Approach*, John Wiley and Sons, Inc., Hoboken, NJ, USA, 2006.

[40] F. Capolino (editor), *Theory and Phenomena of Metamaterials*, CRC Press, Boca Raton, FL, USA, 2009.

[41] G. Rebeiz, *RF MEMS: Theory, Design, and Technology*, John Wiley & Sons, Inc., Hoboken, 2003.

[42] V. Varadan, K.J. Vinoy, and K.A. Jose, *RF MEMS and Their Applications*, John Wiley & Sons, Ltd, Chichester, 2003.

[43] S.P. Pacheco and L.P.B. Ketehi, “Microelectromechanical K-band switching circuits”, *Proc. of the 29th European Microwave Conf.*, 5-7 October 1999, pp. 45-48.

[44] T. Seki, Y. Uno, K. Narise, T. Masuda, K. Inoue, Y. Adachi, K. Hosoya, and F. Sato, “RF-MEMS contact switch technology in OMRON,” *Proc. International Symp. on RF MEMS and RF Microsystems*, Trento, Italy, July 6-8, 2009, pp. 15-18.

[45] C. Vittoria, “Ferrite uses at millimeter wavelengths,” *Journal of Magnetic Materials*, vol. 21, no. 2, pp. 109-118, 1980.

[46] A.S. Tatarenko and G. Srinivasan, ”A strain engineered voltage tunable millimeter-wave ferrite phase shifter,” *Microwave and Optical Technology Letters*, vol. 53, no. 2, pp. 261-264, 2011.

[47] Z. Zhao, X. Wang, K. Choi, C. Lugo, and A.T. Hunt, “Ferroelectric phase shifters at 20 and 30 GHz,” *IEEE Trans. Microwave Theory and Techniques*, vol. 55, no. 2, pp. 430-437, 2007.

[48] J.-J. Hung, L. Dussopt, and G.M. Rebeiz, “Distributed 2- and 3-bit W-band MEMS phase shifters on glass substrates,” *IEEE Trans. Microwave Theory and Techniques,* vol. 52, no. 2, pp. 600-606, 2004.

[49] D. Sievenpiper, *High-impedance Electromagnetic Surfaces*, Ph.D. dissertation, Dept. Elect. Eng., University of California at Los Angeles, CA, 1999, available at http://optoelectronics.eecs.berkeley.edu/ThesisDan.pdf .

[50] J.B. Pendry, A.J. Holden, D.J. Robbins, and W.J. Stewart, “Low frequency plasmons in thin-wire structures,” *Journal of Physics: Condensed Matter*, vol. 10, pp. 4785-4809, 1998.

[51] J.B. Pendry, A.J. Holden, D.J. Robbins, and W.J. Stewart, “Magnetism from conductors and enhanced nonlinear phenomena,” *IEEE Trans. Microwave Theory and Techniques*, vol. 47, no. 11, pp. 2075-1084, Nov. 1999.

[52] R.W. Ziolkowski, "Pulsed and CW gaussian beam interactions with double negative metamaterial slabs," *Optics Express*, vol. 11, no. 7, pp. 662-681, April 2003.

[53] A. Alù and N. Engheta, "Guided modes in a waveguide filled with a pair of single-negative (SNG), double-negative (DNG) and/or double-positive (DPS) layers," *IEEE Trans. Microwave Theory and Techniques*, vol. 52, no. 1, pp. 192-210, January 2004.

[54] C.L. Holloway, E.F. Kuester, J. Baker-Jarvis, and P. Kabos, "A double negative (DNG) composite medium composed of magnetodielectric spherical particles embedded in a matrix," *IEEE Trans. Antennas Propagation*, vol. 51, no. 10, pp. 2596–2603, October 2003.

[55] A.K. Iyer and G.V. Eleftheriades, "Negative refractive index metamaterials supporting 2-D waves," *IEEE MTT International Symp. Digest*, vol. 2, Seattle, WA, US, June 2002, pp. 412-415.

[56] A.A. Oliner, "A periodic-structure negative-refractive-index medium without resonant elements," *Proc. IEEE-AP-S USNC/URSI National Radio Science Meeting*, San Antonio, TX, June 2002, p. 41.

[57] C. Caloz and T. Itoh, "Application of the transmission line theory of left-handed (LH) materials to the realization of a microstrip LH transmission line," *Proc. IEEE-AP-S USNC/URSI National Radio Science Meeting*, vol. 2, San Antonio, TX, June 2002, pp. 412-415.

[58] D.R. Smith, W.J. Padilla, D.C. Vier, S.C. Nemat-Nasser, and S. Schultz, "Composite medium with simultaneously negative permeability and permittivity," *Physical Review Letters*, vol. 84, no. 18, pp. 4184-4187, 2000.

[59] V.M. Shalaev, W. Cai, U.K. Chettiar, H.-K. Yuan, A.K. Sarychev, V.P. Drachev, and A.V. Kildishev, "Negative index of refraction in optical metamaterials," *Optics Letters*, vol. 30, no. 24, pp. 3356-3358, 2005.

[60] C. Simovski and S. Tretyakov, "Historical notes on metamaterials" in F. Capolino (editor), *Theory and Phenomena of Metamaterials*, CRC Press, Boca Raton, FL, USA, 2009.

[61] J.W. Strutt Baron Rayleigh, “On the influence of obstacles arranged in rectangular order upon the properties of a medium,” *Philosophical Magazine*, vol. 34. pp. 431-502, 1892, available at http://ia600108.us.archive.org/14/items/scientificpapers04rayliala/scientificpapers04rayliala.pdf.

[62] W.E. Kock, “Metallic delay lenses,” *Bell System Technical Journal*, vol. 27, pp. 58-82, 1948.

[63] L.I. Mandelshtam, “Lecture on some problems of the theory of oscillations,” in *Complete Collection of Works*, vol. 5, Moscow, Academy of Sciences, pp. 428-467, 1944 (in Russian).

[64] L.I. Mandelshtam, “Group velocity in a crystal lattice,” *Zhurnal Eksperimentalnoi i Teoreticheskoi Fiziki* (*Journal of Experimental and Theoretical Physics*), vol. 15, n. 9, pp. 476-478, 1945 (in Russian).

[65] L. Brillouin, *Wave Propagation in Periodic Structures*, McGraw-Hill, New York, USA, 1946.

[66] J.R. Pierce, *Traveling-Wave Tubes*, D. Van Nostrand, New York, USA, 1950.

[67] D.V. Sivukhin, “The energy of electromagnetic waves in dispersive media,” *Opt. Spektrosk.*, vol. 3, pp. 308-312, 1957.

[68] G.D. Malyuzhinets, “A note on the radiation principle,” *Zhurnal Technicheskoi Fiziki (Journal of Technical Physics)*, vol. 21, pp. 940-942, 1951 (in Russian).

[69] V. Veselago, “The electrodynamics of substances with simultaneously negative values of ε and μ,” *Sov. Physics Uspekhi*, vol. 10, no. 4, pp. 509-514, 1968 (Originally in Russian in *Uspekhi Fizicheskikh Nauk*, vol. 92, p. 517, 1967).

[70] J.B. Pendry, “Negative refraction makes a perfect lens,” *Physical Review Letters*, vol. 85, no. 18, pp. 3966-3969, 2000.

[71] D. Sievenpiper, L. Zhang, R.F.J. Broas, N.G. Alexpolous, and E. Yablonovitch, “High-impedance electromagnetic surfaces with a forbidden frequency band,” *IEEE Trans. Microwave Theory and Techniques*, vol. 47, no. 11, pp. 2059-2074, November 1999.

[72] D.F. Sievenpiper, “Forward and backward leaky wave radiation with large effective aperture from an electronically tunable surface,” *IEEE Trans. Antennas and Propagation*, vol. 53, no. 1, pp. 236-247, January 2005.

[73] D. Sievenpiper, J. Schaffner, B. Loo, G. Tangonan, R. Harold, J. Pikulski, and R. Garcia, “Electronic beam steering using a varactor-tuned impedance surface,” *IEEE International Symp. of Antenna and Propagation Society Digest*, Boston, Massachusetts, USA, 8-13 July 2001, vol. 1, pp. 174-177.

[74] C.C. Cutler, “Electromagnetic waves guided by corrugated conducting surfaces,” Bell Telephone Labs., New York, unpublished classified report, October 1944, cited by [75] and [77].

[75] C.C. Cutler, “Genesis of the corrugated electromagnetic surface,” *IEEE Antennas and Propagation Society International Symp. Digest,* 1994, vol. 3, pp. 1456-1459.

[76] L.G.H. Huxley, *A Survey of the Principles & Practice of Wave Guides*, Cambridge University Press, New York, USA, 1947.

[77] A. Harvey, “Periodic and guiding structures at micro-wave frequencies,” *IRE Trans. Microwave Theory and Techniques*, vol. 8, pp. 30-61, 1960.

[78] W. Rotman, “A study of single surface corrugated guides,” *Proc. IRE*, vol. 39, no. 8, pp. 952-959, August 1951.

[79] R. Elliot, “On the theory of corrugated plane surfaces,” *IRE Trans. Antennas Propagation* , vol. 2, pp. 71-81, April 1954.

[80] L.A. Vainshtein, “Propagation of electromagnetic waves on a corrugated surface,” *Soviet Phys.-Tech. Journal* 1, p. 379, 1956.

[81] S. Lee and W. Jones, “Surface waves on two-dimensional corrugated surfaces,” *Radio Science*, vol. 6, pp. 811-818, 1971.

[82] P.-S. Kildal, “Artificially soft and hard surfaces in electromagnetics,” *IEEE Trans. Antennas Propagation*, vol. 38, pp. 1537-1544, October 1990.

[83] H. Lamb, “On the reflection and transmission of electric waves by a metallic grating,” *Proc. London Mathematical Society*, ser. 1, vol. 29, pp. 523-544, 1898.

[84] W. von Ignatowsky, “Theory of the grating,” *Annalen der Physik*, vol. 44, pp. 369-436, May 1914.

[85] M.I. Kontorovich, “Screening properties of a closed grid,” *Zhurnal Technicheskoi Fiziki (Journal of Technical Physics)*, vol. 9, pp. 2195–2210, 1939 (in Russian).

[86] G.G. MacFarlane, “Surface impedance of an infinite wire grid, at oblique angles of incidence,” *Journal IEE, Part IIIE,* vol. 93, pp. 1523-1527, 1946.

[87] M.I. Kontorovich, V.Y. Petrunkin, N.A. Yesepkina, and M.I. Astrakhan, “The coefficient of reflection of a plane electromagnetic wave from a plane wire mesh,” *Radio Engineering and Electron. Physics*, no. 7, pp. 222-231, 1962.

[88] H.G. Booker, “Slot aerials and their relation to complementary wire aerials (Babinet's principle),” *Journal IEE, Part IIIA*, vol. 93 , no. 4, pp. 620-626, 1946.

[89] R.C. Compton, L.B. Whitbourn, and R.C. McPhedran, “Strip gratings at a dielectric interface and application of Babinet’s principle,” *Applied Optics*, vol. 23, no. 18, pp. 3236-3242, 1984.

[90] S.A. Tretyakov and C.R. Simovski, “Dynamic model of artificial reactive impedance surfaces,” *Journal of Electromagnetic Waves and Applications*, vol. 17, no. 1, pp. 131-145, 2003.

[91] O. Luukkonen, C. Simovski, G. Granet, G. Goussetis, D. Lioubtchenko, A.V. Räisänen, and S.A. Tretyakov, “Simple and accurate analytical model of planar grids and high-impedance surfaces comprising metal strips or patches,” *IEEE Trans. Antennas and Propagation*, vol. 56, no. 6, pp. 1624-1632, 2008.

[92] A.V. Räisänen and A. Lehto, *Radio Engineering for Wireless Communication and Sensor Application*, Artech House, Boston, Massachusetts, May 2003.

[93] D. Sievenpiper, R. Broas, and E. Yablonovitch, “Antennas on high-impedance ground planes,” *IEEE MTT-S International Microwave Symp. Digest*, 1999, pp. 1245-1248.

[94] A. P. Feresidis, G. Goussetis, Shenhong Wang, and J. C. Vardaxoglou, "Artificial magnetic conductor surfaces and their application to low-profile high-gain planar antennas," *IEEE Trans. Antennas and Propagation*, vol. 53, pp. 209-215, 2005.

[95] D. Sievenpiper, J. Schaffner, and J. Navarro, "Axial ratio improvement in aperture antennas using high-impedance ground plane," *Electronics Letters*, vol. 38, pp. 1411-1412, 2002.

[96] B. Palmer, "Capacitance of a parallel-plate capacitor by the Schwartz-Christoffel transformation," *Trans. of AIEE*, vol. 56, p. 363, March 1927.

[97] D. Sievenpiper, J. Schaffner, R. Loo, and G. Tangonan, "Reconfigurable antennas based on electrically tunable impedance surfaces," *Proc. European Microwave Conf.*, London, UK, September 2001, pp. 1-4.

[98] W. Lam, C. Jou, H. Chen, K. Stolt, N. Luhmann, and D. Rutledge, "Millimeter-wave diode-grid phase shifters," *IEEE Trans. MTT*, vol. 36, no. 5, pp. 902-907, May 1988.

[99] J. Higgins, H. Xin, A. Sailer, and M. Rosker, "Ka-band waveguide phase shifter using tunable electromagnetic crystal sidewalls", *IEEE Trans. MTT*, vol. 51, no. 4, pp. 1281-1288, 2003.

[100] W. M. Zhu, H. Cai, T. Mei, T. Bourouina, J. F. Tao, G. Q. Lo, D. L. Kwong, and A. Q. Liu, "A MEMS tunable metamaterial filter," *IEEE International Conf. Microelectromechanical Systems (MEMS)*, 2010, pp. 196-199.

[101] I. Gil, F. Martin, X. Rottenberg, and W. De Raedt, "Tunable stop-band filter at Q-band based on RF-MEMS metamaterials," *Electronics Letters*, vol. 43, pp. 1153-1153, 2007.

[102] T. Jang, S.-H. Hwang, Y.-S. Bang, J.-M. Kim, Y.-K. Kim, C.-W. Baek, and S. Lim, "Switchable composite right/left-handed (S-CRLH) transmission line using MEMS switches," *IEEE Microwave and Wireless Components Letters*, vol. 19, pp. 804-806, 2009.

[103] J. Perruisseau-Carrier, K. Topalli, and T. Akin, "Low-loss Ku-band artificial transmission line with MEMS tuning capability," *IEEE Microwave and Wireless Components Letters*, vol. 19, pp. 377-379, 2009.

[104] N. S. Barker and G. M. Rebeiz, “Distributed MEMS true-time delay phase shifters and wide-band switches,” *IEEE Trans. Microwave Theory and Techniques*, vol. 46, no. 11, pp. 1881-1890, 1998.

[105] J.-H. Park, H.-T. Kim, Y. Kwon, and Y.-K. Kim, “Tunable millimeter-wave filters using a coplanar waveguide and micromachined variable capacitors,” *Journal of Micromechanics and Microengineering*, vol. 11, no. 6, pp. 706-712, 2001.

[106] A. Dec and K. Suyama, “Micromachined electro-mechanically tunable capacitors and their applications to RF IC's,” *IEEE Trans. Microwave Theory and Techniques*, vol. 46, no. 12, pp. 2587-2596, 1998.

[107] T. Vähä-Heikkilä, J. Varis, J. Tuovinen, and G. M. Rebeiz, “W-band RF MEMS double and triple-stub impedance tuners,” *IEEE MTT-S International Microwave Symp. Digest*, Long Beach, CA, USA, June 2005, pp. 923-926.

[108] G. Stojanovic, L. Živanov, and M. Damnjanovic, “Novel efficient methods for inductance calculation of meander inductor,” *The International Journal for Computation and Mathematics in Electrical and Electronic Engineering*, vol. 25, no. 4, pp.916-928, 2006.

[109] J. Higgins, H. Xin, A. Sailer, and M. Rosker, “Ka-band waveguide phase shifter using tunable electromagnetic crystal sidewalls”, *IEEE Trans. Microwave Theory and Techniques*, vol. 51, no. 4, pp. 1281-1288, 2003.

[110] S. Dudorov, *Rectangular Dielectric Waveguide and Its Optimal Transition to a Metal Waveguide*, Doctor’s dissertation, Dept. Elect. Comm. Eng., Helsinki University of Technology, Finland, 2002.

[111] D. Lioubtchenko, S. Tretyakov, and S. Dudorov, *Millimeter-Wave Waveguides*, Kluwer Academic Publishers, The Netherlands, 2003.

[112] D. Lioubtchenko, S. Dudorov, J. Mallat, J. Tuovinen, and A.V. Räisänen, “Low loss sapphire waveguides for 75-110 GHz frequency range,” *IEEE Microwave and Wireless Components Letters*, vol. 11, no. 6, pp. 252-254, 2001.

[113] D.V. Lioubchenko, S.N. Dudorov, and A.V. Räisänen, “Development of rectangular open dielectric waveguide sections for the frequency range of 75-110 GHz,” *Proc. of the 31st European Microwave Conf.,* London, 2001, vol. 2, pp. 201-204.

[114] M. Kim, J.B. Hacker, R.E. Mihailovich, and J.F. DeNatale, “A DC-to-40 GHz four-bit RF MEMS true-time delay network,” *IEEE Microwave and Wireless Components Letters*, vol. 11, no. 2, pp. 56-58, February 2001.

[115] H.-T. Kim, S. Lee, J. Kim, J.-H. Park, Y.-K. Kim, and Y. Kwon, “A V-band CPS distributed analog MEMS phase shifter,” *IEEE MTT-S International Microwave Symp. Digest*, June 2003, vol. 3, pp. 1481-1484.

[116] J. G. Yang and K. Yang, “Ka-band 5-Bit MMIC phase shifter using InGaAs PIN switching diodes,” *IEEE Microwave and Wireless Components Letters*, vol. 21, pp. 151-153, 2011.

[117] D. Teeter, R. Wohlert, B. Cole, G. Jackson, E. Tong, P. Saledas, M. Adlerstein, M. Schindler, and S. Shanfield, “Ka-band GaAs HBT PIN diode switches and phase shifters,” *IEEE MTT-S International Microwave Symp. Digest*, May 1994, pp. 451-454.

[118] J.S. Hayden and G.M. Rebeiz, “Very low-loss distributed X-band and Ka-band MEMS phase shifters using metal-air-metal capacitors,” *IEEE Transactions on Microwave Theory and Techniques*, vol. 51, no. 1, pp. 309-314, January 2003.

[119] B. Pillans, S. Eshelman, A. Malczewski, J. Ehmke, and C. Goldsmith, ”Ka-band RF MEMS phase shifters,” *IEEE Microwave and Guided Wave Letters*, vol. 9, no. 12, pp. 520-522, December 1999.

[120] K. Maruhashi, H. Mizutani, and K. Ohata, “A Ka-band 4-bit monolithic phase shifter using unresonated FET switches,” *IEEE MTT-S International Microwave Symp. Digest*, June 1998, pp. 51-54.

[121] Z. Yonghong, F. Zhenghe, and F. Yong, “Ka-band 4-bit phase shifter with low phase deviation,” *Proc. of the 4th International Conf. Microwave and Millimeter Wave Technology*, 2004, pp. 382-385.

[122] D.-W. Kang, J.-G. Kim, B.-W. Min, and G. M. Rebeiz, “Single and four-element -band transmit/receive phased-array silicon RFICs with 5-bit amplitude and phase control,” *IEEE Trans. Microwave Theory and Techniques*, vol. 57, pp. 3534-3543, 2009.

[123] G. Velu, K. Blary, L. Burgnies, A. Marteau, G. Houzet, D. Lippens, and J.-C. Carru, “A 360° BST phase shifter with moderate bias voltage at 30 GHz,” *IEEE Trans. Microwave Theory and Techniques*, vol. 55, pp. 438-444, 2007.

[124] G. McFeetors and M. Okoniewski, “Distributed MEMS analog phase shifter with enhanced tuning,” *IEEE Microwave and Wireless Components Letters*, vol. 16, pp. 34-36, 2006.

[125] M. Aust, H. Wang, R. Carandang, K. Tan, C.H. Chen, T. Trinh, R. Esfandiari, and H.C. Yen, “GaAs monolithic components development for Q-band phased array application,” *IEEE MTT-S International Microwave Symp. Digest*, June 1992, pp. 703-706.

[126] A.W. Jacomb-Hood, D. Seielstad, and J.D. Merrill, “A three-bit monolithic phase shifter at V-band,” *IEEE Microwave and Millimeter-Wave Monolithic Circuits Symp. Digest*, June 1987, pp. 81-84.

[127] S. Mueller, F. Goelden, P. Scheele, M. Wittek, C. Hock, and R. Jakoby, “Passive phase shifter for W-band applications using liquid crystals,” *Proc. of the 36th European Microwave Conference*, Manchester, UK, 2006, pp. 306-309.

[128] S. Y. Kim and G. M. Rebeiz, “A 4-bit passive phase shifter for automotive radar applications in 0.13 µm CMOS,” *IEEE Compound Semiconductor Integrated Circuit Symposium*, Greensboro, NC, USA, October 2009, DOI: 10.1109/CSICS.2009.5315586.

[129] S. Weinreb, W. Berk, S. Duncan, and N. Byer, “Monolithic varactor 360° phase shifters for 75-110 GHz,” *Proc. of the International Semiconductor Device Research Conf.*, Charlottesville, VA, USA, December 1993, pp. 399-403.

[130] N. Somjit, G. Stemme, and J. Oberhammer, “Binary-coded 4.25-bit W-band monocrystalline-silicon MEMS multistage dielectric-block phase shifters,” *IEEE Trans. Microwave Theory and Techniques*, vol. 57, pp. 2834-2840, 2009.

[131] J.-J. Hung, L. Dussopt, and G. M. Rebeiz, “Distributed 2- and 3-bit W-band MEMS phase shifters on glass substrates,” *IEEE Trans. Microwave Theory and Techniques*, vol. 52, pp. 600-606, 2004.

[132] K. Zuefle, F. Steinhagen, W.E. Haydl, and A. Hulsmann, “Coplanar 4-bit HEMT phase shifters for 94 GHz phased array radar systems,” *IEEE MTT-S International Microwave Symp. Digest,* June 1999, pp. 303-306.

[133] S. E. Shih, D. W. Duan, O. Fordham, M. Parmar, K. Tornquist, X. Zeng, P. Chang-Chien, and R. Tsai, “A W-band 4-bit phase shifter in multilayer scalable array systems,” *IEEE Compound Semiconductor Integrated Circuits Symp. Digest*, Oct. 2007, DOI: 10.1109/CSICS 07.2007.20.

[134] D. Sievenpiper, J. Schaffner, H. J. Song, R. Y. Loo, and G. Tangonan, “Two-dimensional beam steering using an electrically tuneable impedance surface,” *IEEE Trans. Antennas and Propagation*, vol. 51, no.10, pp. 2713-2722, 2003.

[135] W. Menzel, D. Pilz, and M. Al-Tikriti, “MM-wave folded reflector antennas with high gain, low loss, and low profile,” *IEEE Antennas and Propagation Magazine*, pp. 24-29, June 2002.

Appendix A: Detailed description of the MEMS tuneable HIS design

A.1. General considerations

The capacitive array of MEMS-based HIS is realized by two layers of metal patches shifted relative to each other in **E**-field direction (see Fig. 17, Section 2.4.2): the lower patches are placed on the dielectric substrate and the upper membranes of a larger size are fixed with springs on four stems above the neighbouring lower patches. The gap between the lower patches and the upper membranes is filled with air and controlled by an applied actuation voltage which decreases the gap and increases the MEMS capacitance.

As far as the HIS is periodical, it is handy to consider a unit cell, see Fig. A1, for describing the structure dimensions. The **E**-field direction is oriented along the X axis. Each lower patch is divided in two equal parts by the border of two neighbouring unit cells. Once drawn, this unit cell can be easily multiplied periodically while preparing the masks for fabrication.

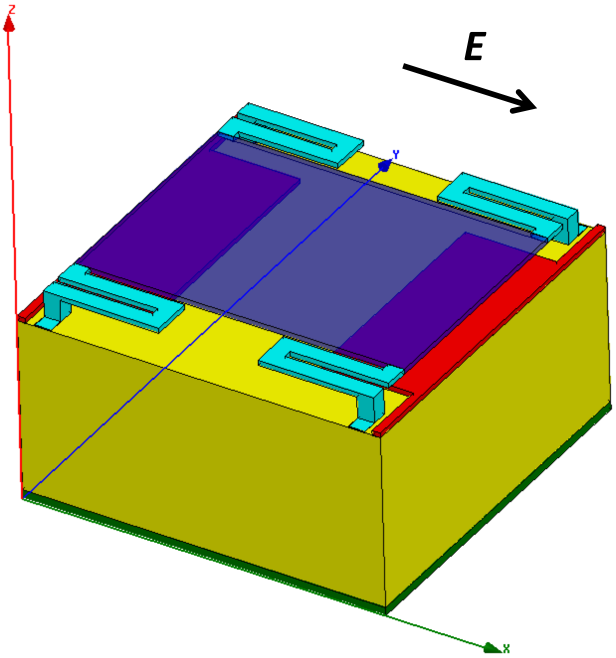

Fig. A1 Unit cell of the HIS. (Upper membrane is semi-transparent to show the lower patches)

All wiring is made along the Y axis. Neither patches, nor membranes are connected in the X directions.

Every row of MEMS capacitors distributed along the axis X is terminated at the edge by one half of the lower patches, see Fig. A2.

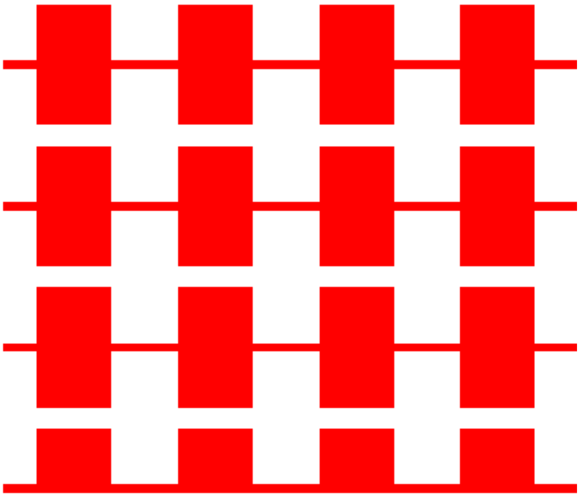

Fig. A2 Edge of the mask for lower patches.

A.2. Parameters

A.2.1 Nominal design

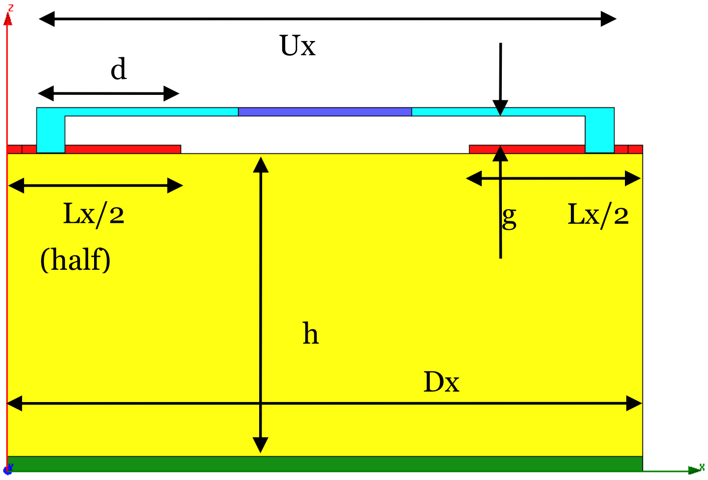

Fig. A3 Side view of the unit cell.

The parameters of the nominal design shown in Fig. A3 are:

Dx – period of the HIS along the X axis,

Ux – width of the upper membrane along the X axis,

d – horizontal overlapping between the upper membrane and lower patch,

Lx – width of the lower patch along the X axis,

h – thickness of the dielectric substrate,

g – gap between the lower side of the upper membrane and the upper side of the lower patch,

t_l – thickness of the lower patch.

The upper membrane consists of a monocrystalline silicon layer covered from all sides by metal, see Fig. A4.

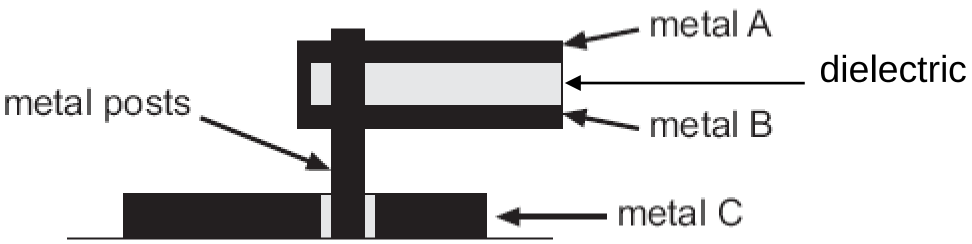

Fig. A4 Cross-section of the upper membrane of the MEMS tuneable HIS.

Corresponding parameters of the membrane are:
t_a, t_b, t_c, t_d – thicknesses of metal layers A, B, C and dielectric layer between layers A and B.

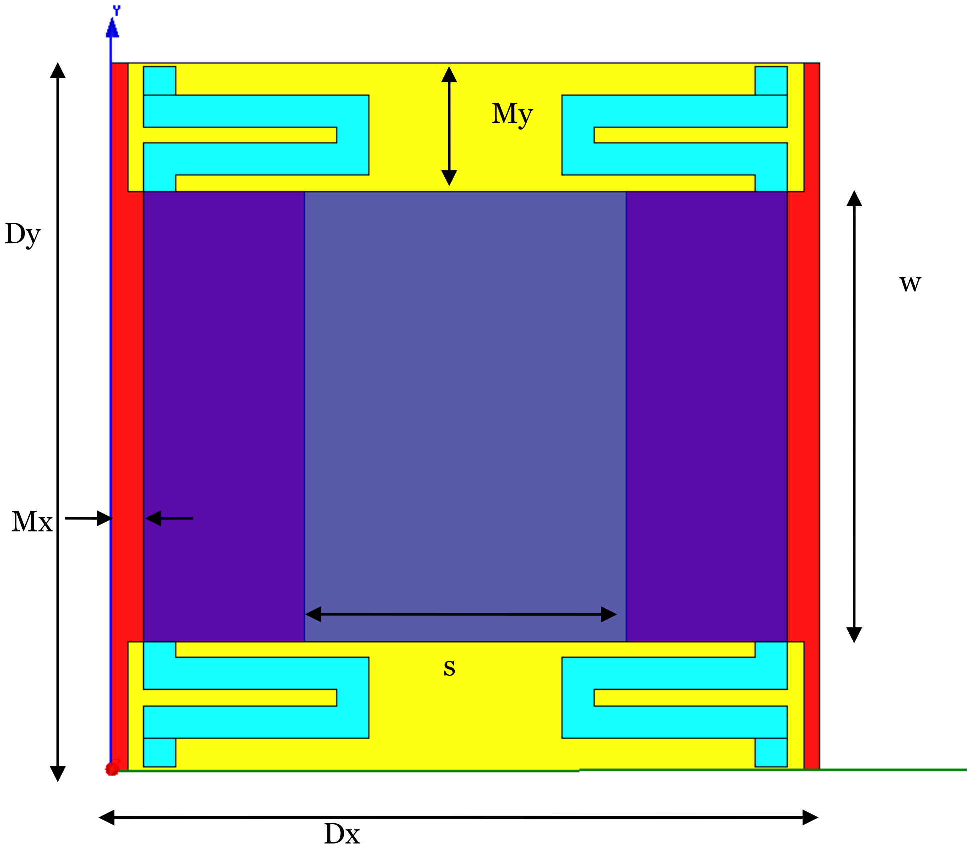

Fig. A5 Top view of the unit cell.

Parameters shown in Fig. A5 are:
Dx – period of the HIS along the X axis,
Dy – period of the HIS along the Y axis,

w – width of the overlapping between the membrane and lower patch (normally equal to the width of the membrane and lower patch along the Y axis),
s – separation between the lower patches along the X axis,
Mx – margin between the membrane and unit cell border along the X axis (2×Mx is the separation between membranes along the X axis),
My – margin between the membrane and unit cell border along the Y axis (2×My is separation between membranes along the Y axis).

Dimensions of the springs, stems and wiring are to be chosen according to the fabrication constraints and taking into account their influence on the actuation voltage and HIS loss at the resonance. The parameters are the same as in Fig. 27 of Section 2.4.4:
l_{spr} – length of the spring,
w_{spr} – width of the spring,
s_{spr} – spacing between the turns of the spring.

The losses are smaller for a longer spring, e.g., l_{spr} = 110 μm. Optimal dimension for the spring width is w_{spr} = 10 μm. The spacing can be found as $s_{spr} = (My - 2\times w_{spr})/3$.

A.2.2 Design with additional actuation electrode

As described in Section 2.4.3, instead of actuation by applying voltage source between the membrane and the lower patches, an additional actuation electrode (orange in Fig. A6) can be introduced between the lower patches. If its thickness is smaller than the thickness of the lower patches, the tuning range of the MEMS capacitance is increased. Electrode material might be a metal with high resistivity, e.g. 200 nm Cr.

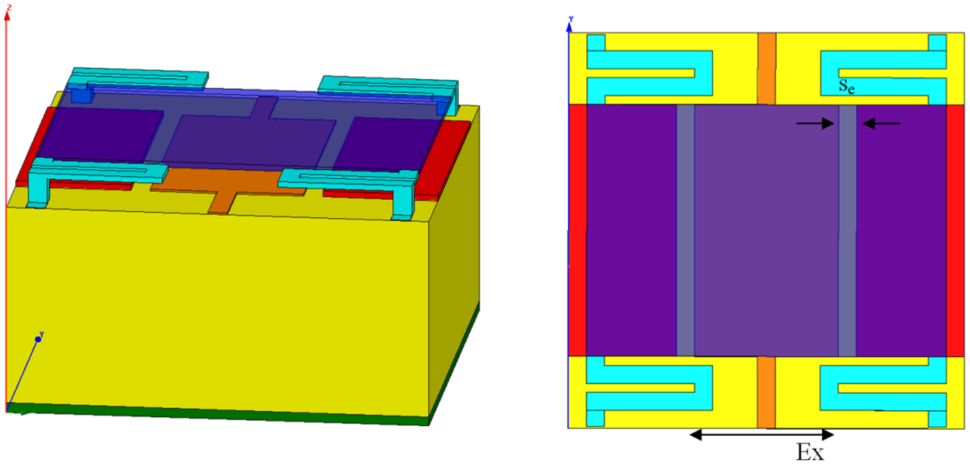

Fig. A6 Additional actuation electrode design, 3D view and top view of the unit cell.

Ex – width of the electrode along the X axis,

s_e – separation between the actuation electrode and the lower patches.
t_e – thickness of the electrode.

Width Ex should be not less than 2*d in order to gain in actuation voltage value comparing to the nominal design. Thickness t_e should be much smaller than t_l in order to gain in tuning range. Separation s_e should be not smaller than 10 μm.

A.2.3 Fixed and flexible parameters

Fixed parameters:

h = 110 μm (total wafer thickness). If final h will differ a lot from 110 μm, it can be compensated by value g.

h, w, d, g – most important parameters that determine the resonance frequency.

Flexible parameters:

Following parameters can be slightly changed in order to facilitate fabrication and fit springs.

Dx, Dy, Ux: Dx and Dy should not be larger than 350 μm. Large Ux is good for additional electrode design (allows large Ex), but may be difficult to fabricate and is limited by Dx.

Ex is also flexible, but is related to d, Dx and Ux:
$Ex \le Ux - 2\times d - 20\ \mu m \le Dx - 2\times d - 40\ \mu m$

Dx can be intentionally made larger to increase Ex.

Following parameters will be uniquely related to the previous ones:
$Lx = Dx - Ux + 2*d$,
$Mx = 0.5(Dx - Ux)$,
$My = 0.5(Dy - Uy)$,
$s = Ux - 2*d$,
$s_e = 0.5(Ux - Ex) - d$

Suggested values for thicknesses:
$t_a = t_b$, = 0.5 μm or larger
$t_c = t_d = 1\ \mu m$
$t_e = 0.2\ \mu m$.

A.2.4. Algorithm for choosing values of the flexible parameters

The flexible parameters cab be chosen according to the following algorithm:

1. Determine the size occupied by a spring and a stem along the Y axis. That will give My.
2. 2×My + w will give Dy.
3. Dx should be close to Dy (Square cell is preferable, but Dx and Dy can differ by 10%).
4. Ux ≤ Dx – 20 μm to give space for wiring to lower patches (Mx ≥ 10 μm).
5. Lx, s, Ex, s_e – calculated by formulae above.

A.3. Description of structures (chips) to manufacture

There are three different experiments that will be carried out with manufactured HIS chips:

1. Reflection type phase shifter (RT). A HIS of 1.27 × 2.54 mm^2 will be put as a backshort of a rectangular metal waveguide, and the S_{11} parameter will be measured at 70-115 GHz frequency range. Changing the gap by applying voltage will result in a smooth change of the resonant frequency of the HIS. All membranes are connected to one voltage source, and all lower patches (or additional electrodes) are connected to a common ground. At least 4 structures overall on one wafer: two of nominal design (RT) and two of additional electrode design (RT+e).
2. Phase shifter based on a dielectric waveguide (DW). A HIS of 6× 30 mm^2 will be put adjacent to a dielectric waveguide, and the S-parameters will be measured. Applying voltage will result in changing the impedance of the HIS, which will lead to a phase shift. All membranes are connected to one voltage source, and all lower patches (or additional electrodes) are connected to a common ground. Two structures overall on one wafer: one for the nominal design (DW) and another for additional electrode design (DW+e).
3. Beam steering (BS). A HIS of 70× 18.2 mm^2 will be illuminated by a plane wave. Membranes are connected in rows along the Y axis and every row is biased by a separate voltage source. When voltage gradient is induced along the X axis, the reflection wave will change its direction. All lower patches (or additional electrodes) are connected to a common ground. Two structures overall on one

wafer: one for the nominal design (BS) and another for additional electrode design (BS+e).

A.4. Dimensions

For all structures h=110 μm. Material of the wafer is high resistivity silicon. All dimensions are in microns. Nx and Ny are the number of cells along the X and Y axis correspondingly. Every HIS structure on the wafer should be labelled by four parameters: h, w, d, g.

Wafer 1 (main option, estimated resonance frequency 84 GHz):

Structure	**g**	**w**	**d**	D_x	D_y	N_x	N_y	M_x	M_y	U_x	L_x	l_{spr}	w_{spr}	s_{spr}	**s**	E_x	s_e
RT	1.8	130	32	250	250	5	10	30	60	190	124	110	10	13	126	-	-
RT+e	1.8	130	32	250	250	5	10	10	60	230	84	110	10	13	166	140	13
DW	1.8	130	32	250	250	24	120	30	60	190	124	110	10	13	126	-	-
DW+e	1.8	130	32	250	250	24	120	10	60	230	84	110	10	13	166	140	13
BS	1.8	130	32	350	350	200	52	70	110	210	204	110	10	30	146	-	-
BS+e	1.8	130	32	350	350	200	52	50	110	250	164	110	10	30	186	160	13

Period of RT structure is limited by 250 μm (D≤250) in order to have at least 5 elements in X direction. Period of BS structure is made larger to have fewer elements and make more space for the contact pads.

Wafer 2 (estimated resonance frequency 89 GHz):
g = 2.2 μm
Other dimensions as in the table above (same fabrication masks).

Wafer 3 (estimated resonance frequency 77 GHz):
g = 1.4 μm
Other dimensions as in the table above (same fabrication masks).

Aalto-DD 127/2011

This thesis focuses on the development of novel smart microelectromechanically tuneable electromagnetic surfaces, namely high-impedance surfaces, for millimetre wave beam steering applications. One of such applications is automotive radar at 79 GHz, where electronic steering of the beam is needed for accurate detection of objects in the vehicle's surroundings. Major challenges in development of millimetre wave beam steering devices are high level of losses and high cost of millimetre wave components, e.g., phase shifters. The concept presented in this thesis is to combine smart artificial electromagnetic materials and microelectromechanical systems (MEMS) fabrication technology. The methodology used in this study is a combination of analytical analysis, numerical simulations and electromagnetic measurements of MEMS tuneable high-impedance surfaces. Several prototypes were fabricated, and their characterisation confirmed designed properties of the high-impedance surfaces.

9 789526 043890

ISBN 978-952-60-4389-0
ISBN 978-952-60-4390-6 (pdf)
ISSN-L 1799-4934
ISSN 1799-4934
ISSN 1799-4942 (pdf)

Aalto University
School of Electrical Engineering
Department of Radio Science and Engineering
www.aalto.fi

BUSINESS +
ECONOMY

ART +
DESIGN +
ARCHITECTURE

SCIENCE +
TECHNOLOGY

CROSSOVER

DOCTORAL
DISSERTATIONS